

國立交通大學

應用化學系碩士班

碩士論文

位移技術應用在多參考態微擾理論的關鍵評核

Critical Evaluation of Shift Techniques Applicable to

Multireference Perturbation Theory

研究生：張書維

指導教授：魏恆理 副教授

中華民國一百年八月

位移技術應用在多參考態微擾理論的關鍵評核

Critical Evaluation of Shift Techniques Applicable to Multireference
Perturbation Theory

研究生：張書維
指導教授：魏恆理

Student: Shu-Wei Chang
Advisor: Henryk Witek

國立交通大學

應用化學系碩士班



Submitted to M. S. Program, Department of Applied Chemistry
College of Science

National Chiao Tung University

In Partial Fulfillment of the Requirement

for the Degree of

Master

In

Applied Chemistry

August 2011

Hsinchu, Taiwan, Republic of China

中華民國一百年八月

位移技術應用在多參考態微擾理論的關鍵評核

研究生：張書維

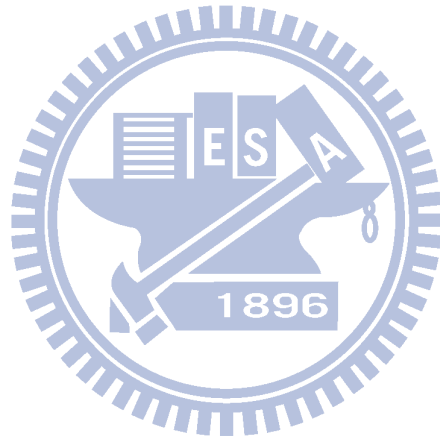
指導教授：魏恆理

國立交通大學應用化學系碩士班

摘要

為了描述激發態與開殼層系統，多參考態微擾理論 (multireference perturbation theory) 是精確的電子相關 (electron-correlation) 方法中為最受信賴且計算上較可實行的。然而，多參考態微擾理論卻存在著一個嚴重的問題，稱之為入侵態 (intruder states) 問題。入侵態會使得系統的位能面不連續且導致沒有物理意義的結果。多參考態微擾理論配合位移技術 (shift techniques) 的使用可以很有效地移除入侵態。儘管如此，用多參考態微擾理論來研究系統的化學性質會隨著位移技術所使用的參數而劇烈地改變。我們因此著手進行各種可運用的位移技術研究，即實數位移 (real shift)、虛數位移 (imaginary shift) 與入侵態規避技術 (intruder state avoidance technique)，並找出其適當的位移參數值。

本論文藉由不同的多參考態微擾理論的方法結合各種位移技術，研究了 15 種雙原子分子中的 65 條低能量電子態 (low-lying electronic states) 之位能曲線。我們用不同的位移值來極限測試這些位能曲線及其光譜常數 (spectroscopic constants) 並與實驗值作比較。最後，運用統計分析來決定每一種位移技術的優化的位移參數值。研究結果顯示當使用優化的位移參數值，不僅可以有效地移除入侵態，還可以減少研究系統在光譜常數上的誤差。



Critical Evaluation of Shift Techniques Applicable to Multireference
Perturbation Theory

Student: Shu-Wei Chang

Advisor: Henryk Witek

M. S. Program, Department of Applied Chemistry
National Chiao Tung University



Abstract

For describing excited states and open-shell systems, multireference perturbation theory (MRPT) is the most reliable and computationally feasible among accurate electron-correlation methods. However, the MRPT methods are subject to a serious problem, known as the intruder state problem. The intruder states shall cause discontinuities in the potential energy surface of a system leading to non-physical results. The use of shift techniques in the MRPT may efficiently eliminate intruder states. Nevertheless, the chemical properties of the system studied using MRPT can change strongly depending on the parameter employed in the shift techniques. We therefore undertook an investigation for available shift techniques (e.g., real shift, imaginary shift, and intruder state avoidance techniques) to find appropriate values of these shift parameters. In this Thesis, 65 potential energy curves of low-lying

electronic states of 15 diatomic molecules were studied using different MRPT methods combined with various shift techniques. The potential energy curves and their spectroscopic constants were critically evaluated for various values of the shift parameter, and compared with experiment. Finally, we used statistical analysis to determine the optimal value of the shift parameter in each shift technique. The research results show that the shift techniques can efficiently eliminate the intruder states and at same time they also reduce the error in spectroscopic parameters of the studied system when an optimal value of shift parameter is used.



Acknowledgment

I would like to sincerely express my gratitude to Prof. Henryk A. Witek, who is friendly and kind, for his patient guidance and encouragement. He gave me an opportunity to learn science from his profound knowledge and the elaborated classes. Without him, I could not get this point, have a wonderful travel with his family and lab mates, and dine together just like a family.

I would like to thank Prof. Zhu and Prof. Shigeto, members of my thesis committee, for their invaluable suggestion and insightful comment on my thesis.

I would like to express the deepest appreciation to my dear parents, brother, and my girlfriend, Yu-Chun for their love, continued support and toleration. I really love you all.

I would like to thank my friends, Christopher, Chien-Pin, Po-Yu, Amy, Chun-Hao, Wun-Fan, Nishimura-san and May in the laboratory for their kindly helping, and cheering me. They gave me an unfadable memory and enrich my life.

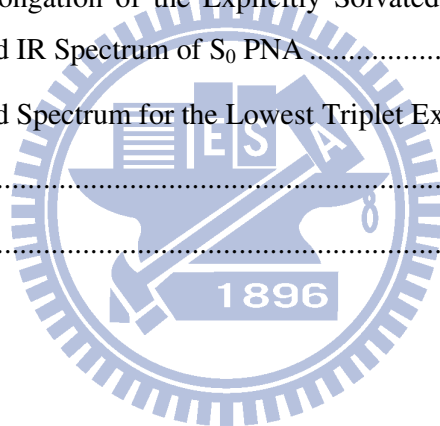
It is my honor to meet many people in these years. Thank you for making me laugh. I will treasure you for sharing precious times.

Finally, this thesis is dedicated to all people who have helped and supported me.

Contents

List of Figures	VIII
List of Tables	XVII
Chapter 1 Introduction	1
Chapter 2 Computational Theory	6
2.1 The Variational Method	6
2.2 The Rayleigh-Schrödinger Perturbation Theory	8
2.3 The Hartree-Fock Method	12
2.4 Configuration State Function	19
2.5 The Multiconfiguration Self-Consistent Field Method.....	21
2.6 The Multireference Perturbation Theory	23
2.7 Intruder States and Shift Techniques	24
Chapter 3 Computational Details	26
Chapter 4 Results and Discussion	29
4.1 Potential Energy Curves.....	29
4.2 Intruder States.....	30
4.3 Effect of Using Intruder State Removal Techniques: General Observations...31	
4.4 Effect of Using Intruder State Removal Techniques: Details	32
4.5 Statistical Analysis for Intruder State Removal Techniques.....	34
4.5.1 Distribution of Changes in Spectroscopic Constants.....	34
4.5.2 Mean Absolute Deviations from Experiments for Spectroscopic Constants	36
4.5.3 Optimal Values of Shift Techniques	37
Chapter 5 Conclusions	40

Chapter 6 Auxiliary materials	41
Appendix A Theoretical Study of <i>p</i>-Nitroaniline for the Infrared Spectra of Ground State and the Lowest Triplet State	91
A.1 Introduction	91
A.2 Computational Details.....	92
A.3 Results and Discussion.....	93
A.3.1 Failure of Simulated Gas-phase and PCM IR Spectra for Singlet Ground State of PNA	93
A.3.2 Simulated IR Spectra of S ₀ PNA Using Explicitly Solvated Models ..	95
A.3.3 Slight Elongation of the Explicitly Solvated Models for Improving Simulated IR Spectrum of S ₀ PNA	96
A.3.4 Simulated Spectrum for the Lowest Triplet Excited State of PNA	99
A.4 Conclusion.....	101
References	102



List of Figures

- Figure 1.1** CASPT2/MOLCAS potential energy curves computed with two values of the imaginary shift parameter σ for the $A^1\Pi$ excited state of CO. ... 3
- Figure 2.1** Excited determinants formed from a HF determinant.¹⁵ 20
- Figure 2.2** Illustration of complete active space. 22
- Figure 4.1** MCQDPT/GAMESS potential energy curves with various values of shift parameter σ for the excited $^5\Pi$ state (a) and $^1\Pi$ (b) state of CO. ... 31
- Figure 4.2** Spectroscopic constants for the $A^1\Pi$ state of CO obtained using different methods with various values of the shift parameter σ 33
- Figure 4.3** Combined errors with various values of the shift parameter for different methods. 38
- Figure 6.1** Spectroscopic constants for the $X^1\Sigma^+$ state of BH obtained using different methods with various values of the shift parameter σ 41
- Figure 6.2** Spectroscopic constants for the $a^3\Pi$ state of BH obtained using different methods with various values of the shift parameter σ 42
- Figure 6.3** Spectroscopic constants for the $A^1\Pi$ state of BH obtained using different methods with various values of the shift parameter σ 42
- Figure 6.4** Spectroscopic constants for the $b^3\Sigma^-$ state of BH obtained using different methods with various values of the shift parameter σ 43
- Figure 6.5** Spectroscopic constants for the $X^2\Pi$ state of CH obtained using different methods with various values of the shift parameter σ 43

Figure 6.6	Spectroscopic constants for the $a^4\Sigma^-$ state of CH obtained using different methods with various values of the shift parameter σ	44
Figure 6.7	Spectroscopic constants for the $A^2\Delta$ state of CH obtained using different methods with various values of the shift parameter σ	44
Figure 6.8	Spectroscopic constants for the $X^3\Sigma^-$ state of NH obtained using different methods with various values of the shift parameter σ	45
Figure 6.9	Spectroscopic constants for the $a^1\Delta$ state of NH obtained using different methods with various values of the shift parameter σ	45
Figure 6.10	Spectroscopic constants for the $b^1\Sigma^+$ state of NH obtained using different methods with various values of the shift parameter σ	46
Figure 6.11	Spectroscopic constants for the $A^3\Pi$ state of NH obtained using different methods with various values of the shift parameter σ	46
Figure 6.12	Spectroscopic constants for the $X^2\Pi$ state of OH obtained using different methods with various values of the shift parameter σ	47
Figure 6.13	Spectroscopic constants for the $A^2\Sigma^+$ state of OH obtained using different methods with various values of the shift parameter σ	47
Figure 6.14	Spectroscopic constants for the $X^1\Sigma^+$ state of HF obtained using different methods with various values of the shift parameter σ	48
Figure 6.15	Spectroscopic constants for the $X^1\Sigma^+$ state of BF obtained using different methods with various values of the shift parameter σ	48
Figure 6.16	Spectroscopic constants for the $A^1\Pi$ state of BF obtained using different methods with various values of the shift parameter σ	49

Figure 6.17	Spectroscopic constants for the $a^3\Pi$ state of BF obtained using different methods with various values of the shift parameter σ	49
Figure 6.18	Spectroscopic constants for the $A^2\Pi$ state of CN obtained using different methods with various values of the shift parameter σ	50
Figure 6.19	Spectroscopic constants for the $X^1\Sigma^+$ state of CO obtained using different methods with various values of the shift parameter σ	50
Figure 6.20	Spectroscopic constants for the $D^1\Delta$ state of CO obtained using different methods with various values of the shift parameter σ	51
Figure 6.21	Spectroscopic constants for the $A^1\Pi$ state of CO obtained using different methods with various values of the shift parameter σ	51
Figure 6.22	Spectroscopic constants for the $I^1\Sigma^-$ state of CO obtained using different methods with various values of the shift parameter σ	52
Figure 6.23	Spectroscopic constants for the $a^3\Sigma^+$ state of CO obtained using different methods with various values of the shift parameter σ	52
Figure 6.24	Spectroscopic constants for the $d^3\Delta$ state of CO obtained using different methods with various values of the shift parameter σ	53
Figure 6.25	Spectroscopic constants for the $a^3\Pi$ state of CO obtained using different methods with various values of the shift parameter σ	53
Figure 6.26	Spectroscopic constants for the $e^3\Sigma^-$ state of CO obtained using different methods with various values of the shift parameter σ	54
Figure 6.28	Spectroscopic constants for the $X^2\Pi$ state of FO obtained using different methods with various values of the shift parameter σ	55

Figure 6.29	Spectroscopic constants for the $X^2\Pi$ state of NO obtained using different methods with various values of the shift parameter σ	55
Figure 6.30	Spectroscopic constants for the $B^2\Pi$ state of NO obtained using different methods with various values of the shift parameter σ	56
Figure 6.31	Spectroscopic constants for the $^2\Phi(1)$ state of NO obtained using different methods with various values of the shift parameter σ	56
Figure 6.32	Spectroscopic constants for the $a^4\Pi$ state of NO obtained using different methods with various values of the shift parameter σ	57
Figure 6.33	Spectroscopic constants for the $b^4\Sigma^-$ state of NO obtained using different methods with various values of the shift parameter σ	57
Figure 6.34	Spectroscopic constants for the $B'^2\Delta$ state of NO obtained using different methods with various values of the shift parameter σ	58
Figure 6.35	Spectroscopic constants for the $X^3\Sigma_g^-$ state of B_2 obtained using different methods with various values of the shift parameter σ	58
Figure 6.36	Spectroscopic constants for the $X^1\Sigma_g^+$ state of C_2 obtained using different methods with various values of the shift parameter σ	59
Figure 6.37	Spectroscopic constants for the $^1\Delta_g(1)$ state of C_2 obtained using different methods with various values of the shift parameter σ	59
Figure 6.38	Spectroscopic constants for the $^1\Sigma_g^+(2)$ state of C_2 obtained using different methods with various values of the shift parameter σ	60
Figure 6.39	Spectroscopic constants for the $a^3\Pi_u$ state of C_2 obtained using different methods with various values of the shift parameter σ	60

Figure 6.40	Spectroscopic constants for the $b^3\Sigma_g^-$ state of C_2 obtained using different methods with various values of the shift parameter σ	61
Figure 6.41	Spectroscopic constants for the $A^1\Pi_u$ state of C_2 obtained using different methods with various values of the shift parameter σ	61
Figure 6.42	Spectroscopic constants for the $c^3\Sigma_u^+$ state of C_2 obtained using different methods with various values of the shift parameter σ	62
Figure 6.43	Spectroscopic constants for the $d^3\Pi_g$ state of C_2 obtained using different methods with various values of the shift parameter σ	62
Figure 6.44	Spectroscopic constants for the $e^3\Pi_g$ state of C_2 obtained using different methods with various values of the shift parameter σ	63
Figure 6.45	Spectroscopic constants for the $C^1\Pi_g$ state of C_2 obtained using different methods with various values of the shift parameter σ	63
Figure 6.46	Spectroscopic constants for the $X^3\Sigma_g^+$ state of N_2 obtained using different methods with various values of the shift parameter σ	64
Figure 6.47	Spectroscopic constants for the $A^3\Sigma_u^+$ state of N_2 obtained using different methods with various values of the shift parameter σ	64
Figure 6.48	Spectroscopic constants for the $W^3\Delta_u$ state of N_2 obtained using different methods with various values of the shift parameter σ	65
Figure 6.49	Spectroscopic constants for the $B^3\Pi_g$ state of N_2 obtained using different methods with various values of the shift parameter σ	65
Figure 6.50	Spectroscopic constants for the $B'^3\Sigma_u^-$ state of N_2 obtained using different methods with various values of the shift parameter σ	66

Figure 6.51	Spectroscopic constants for the $a' \ ^1\Sigma_u^-$ state of N_2 obtained using different methods with various values of the shift parameter σ	66
Figure 6.52	Spectroscopic constants for the $w \ ^1\Delta_u$ state of N_2 obtained using different methods with various values of the shift parameter σ	67
Figure 6.53	Spectroscopic constants for the $a \ ^1\Pi_g$ state of N_2 obtained using different methods with various values of the shift parameter σ	67
Figure 6.54	Spectroscopic constants for the $C \ ^3\Pi_u$ state of N_2 obtained using different methods with various values of the shift parameter σ	68
Figure 6.55	Spectroscopic constants for the $X \ ^3\Sigma_g^-$ state of O_2 obtained using different methods with various values of the shift parameter σ	68
Figure 6.56	Spectroscopic constants for the $a \ ^1\Delta_g$ obtained using different methods with various values of the shift parameter σ	69
Figure 6.58	Spectroscopic constants for the $c \ ^1\Sigma_u^-$ state of O_2 obtained using different methods with various values of the shift parameter σ	70
Figure 6.59	Spectroscopic constants for the $A' \ ^3\Delta_u$ state of O_2 obtained using different methods with various values of the shift parameter σ	70
Figure 6.60	Spectroscopic constants for the $A \ ^3\Sigma_u^+$ state of O_2 obtained using different methods with various values of the shift parameter σ	71
Figure 6.61	Spectroscopic constants for the $X \ ^1\Sigma_g^+$ state of F_2 obtained using different methods with various values of the shift parameter σ	71
Figure 6.62	Spectroscopic constants for the $^1\Sigma_g^- (1)$ state of F_2 obtained using different methods with various values of the shift parameter σ	72

Figure 6.63	Spectroscopic constants for the $^1\Pi_g(1)$ state of F_2 obtained using different methods with various values of the shift parameter σ	72
Figure 6.64	Spectroscopic constants for the $^1\Pi_u(1)$ state of F_2 obtained using different methods with various values of the shift parameter σ	73
Figure 6.65	Spectroscopic constants for the $^3\Pi_u(1)$ state of F_2 obtained using different methods with various values of the shift parameter σ	73
Figure 6.66	Distribution of changes in R_e induced by changing the intruder state removal parameter within whole studied shift values.....	74
Figure 6.67	Distribution of changes in R_e induced by changing the intruder state removal parameter ignoring the region of yellow boxes in Figures 6.1-6.65.	74
Figure 6.68	Distribution of changes in ω_e induced by changing the intruder state removal parameter within whole studied range of the shift values.	75
Figure 6.69	Distribution of changes in ω_e induced by changing the intruder state removal parameter ignoring the region of yellow boxes in Figures 6.1-6.65.	75
Figure 6.70	Distribution of changes in D_e induced by changing the intruder state removal parameter within whole studied range of the shift values.	76
Figure 6.71	Distribution of changes in D_e induced by changing the intruder state removal parameter ignoring the region of yellow boxes in Figures 6.1-6.65.	76
Figure 6.72	Mean absolute deviation from the experiment for R_e obtained with	

	CASPT2/MOLPRO method.....	77
Figure 6.73	Mean absolute deviation from the experiment for R_e obtained with MCQDPT/GAMESS method.....	77
Figure 6.74	Mean absolute deviation from the experiment for R_e obtained with IPEA-CASPT2/MOLCAS method.....	78
Figure 6.75	Mean absolute deviation from the experiment for R_e obtained with CASPT2/MOLCAS method.....	78
Figure 6.76	Mean absolute deviation from the experiment for R_e obtained with G1-CASPT2/MOLCAS method.....	79
Figure 6.77	Mean absolute deviation from the experiment for ω_e obtained with CASPT2/MOLPRO method.....	79
Figure 6.78	Mean absolute deviation from the experiment for ω_e obtained with MCQDPT/GAMESS method.....	80
Figure 6.79	Mean absolute deviation from the experiment for ω_e obtained with IPEA-CASPT2/MOLCAS method.....	80
Figure 6.80	Mean absolute deviation from the experiment for ω_e obtained with CASPT2/MOLCAS method.....	81
Figure 6.81	Mean absolute deviation from the experiment for ω_e obtained with G1CASPT2/MOLCAS method.....	81
Figure 6.82	Mean absolute deviation from the experiment for D_e obtained with CASPT2/MOLPRO method.....	82
Figure 6.83	Mean absolute deviation from the experiment for D_e obtained with	

	MCQDPT/GAMESS method.....	82
Figure 6.84	Mean absolute deviation from the experiment for D_e obtained with IPEA-CASPT2/MOLCAS method.....	83
Figure 6.85	Mean absolute deviation from the experiment for D_e obtained with CASPT2/MOLCAS method.....	83
Figure 6.86	Mean absolute deviation from the experiment for D_e obtained with G1-CASPT2/MOLCAS method.....	84
Figure A.1	Experimental and computational IR spectra for singlet ground state of PNA. The asterisk symbol indicates the spectra obtained from the PNA+2ACN with the elongation of C–NH ₂ model.	94
Figure A.2	Schematic geometries of the explicitly solvated models.....	96
Figure A.3	Experimental and computational IR spectra for singlet ground state of PNA and isotope-substituted PNA. The IR spectra obtained from PNA+2ACN (dotted line) and PNA+2ACN with the elongation of C–NH ₂ (solid line) models.....	98
Figure A.4	Experimental and computational IR spectra for the lowest excited triplet state of PNA. The asterisk symbol indicates the spectra obtained from the PNA+2ACN with the elongation of C–NH ₂ model.....	100
Figure A.5	Experimental and computational IR spectra for the lowest triplet state of PNA and isotope-substituted PNA. The IR spectra obtained from PNA+2ACN (dotted line) and PNA+2ACN with the elongation of C–NH ₂ (solid line) models.....	101

List of Tables

Table 1 The low-lying electronic states included in the MRPT calculations and numbers of available experimental data for diatomic molecules.....	85
Table 2 Experimental data of the low-lying states for diatomic molecules.....	86
Table 3 Conversion of coefficients from spherical harmonic type to Cartesian type.	89



Chapter 1

Introduction

Theoretical calculations and quantum chemistry are getting more and more important in recent years because scientists can employ computational techniques to predict, explain, and rationalize many chemical properties of molecules such as equilibrium structures, dipole moments, excitation energies, infrared spectra, Raman spectra, reaction mechanisms, etc. Especially thanks to the fast development of computing technology and enhancement of the speed of the central processing units (CPU), we are able to deal with the constantly growing computational cost. On the other hand, personal computers are much cheaper and faster than supercomputers ten years ago. It is easy to get a personal computer and employ it in theoretical calculations helping one's research.

In quantum chemistry, the Schrödinger equation is a complicated problem that cannot be solved exactly because of existence of electron-electron interactions in a many-electron system. Hartree-Fock (HF) theory was developed to solve the Schrödinger equation approximately. Afterward many electron-correlation methods have been developed based on the Hartree-Fock (HF) equations. Thus the Hartree-Fock (HF) method certainly became a keystone of quantum chemistry. The popular electron-correlation methods include multiconfiguration self-consistent field

(MCSCF), configuration interaction (CI), coupled-cluster (CC), Møller-Plesset perturbation theory (MPPT), multireference perturbation theories (MRPT), etc. These methods take into account electron correlation to overcome the defect of the HF method and to improve the accuracy. Unfortunately, computational costs of both the CI methods and the CC methods are indeed expensive even though these methods are regarded as very accurate methods. Another popular class of methods is called density functional theory (DFT), in which electronic energy of a system can be expressed in terms of a functional of the electron density. An advantage of DFT is much lower computational cost.

Many chemical problems often involve excited states, multiplet electronic structures and quasi-degenerate systems. However, the HF method and MPPT method are based on a single Slater determinant and therefore are not adequate to describe such open-shell systems. In DFT, there is no systematic way to deal with the excited states and the spin multiplet systems. Scientists devoted substantial effort developing accurate methods for solving these problems. One of possible reliable and computationally feasible ways to describe this kind of systems is a combination of the multiconfiguration self-consistent field (MCSCF) method together with an appropriate electron-correlation technique such as multireference configuration interaction (MRCI) method, multireference coupled-cluster (MRCC) method, or multireference perturbation theory (MRPT). The MCSCF wavefunctions are used as reference states in MRCI, MRCC and MRPT. Here, a limitation is that both MRCI and MRCC can only be applied for small molecules (<10 atoms) and only the MRPT

methods are applicable for larger systems (about 20 atoms).

Based on Rayleigh-Schrödinger perturbation theory (RSPT), the popular MRPT methods include complete active space perturbation theory (CASPT2)^{1,2}, multireference Møller-Plesset perturbation theory (MRMP)³, multiconfigurational quasidegenerate perturbation theory (MCQDPT)⁴ and n-electron valence state perturbation theory (NEVPT2)⁵. Most of these methods may suffer from the problem of intruder states.

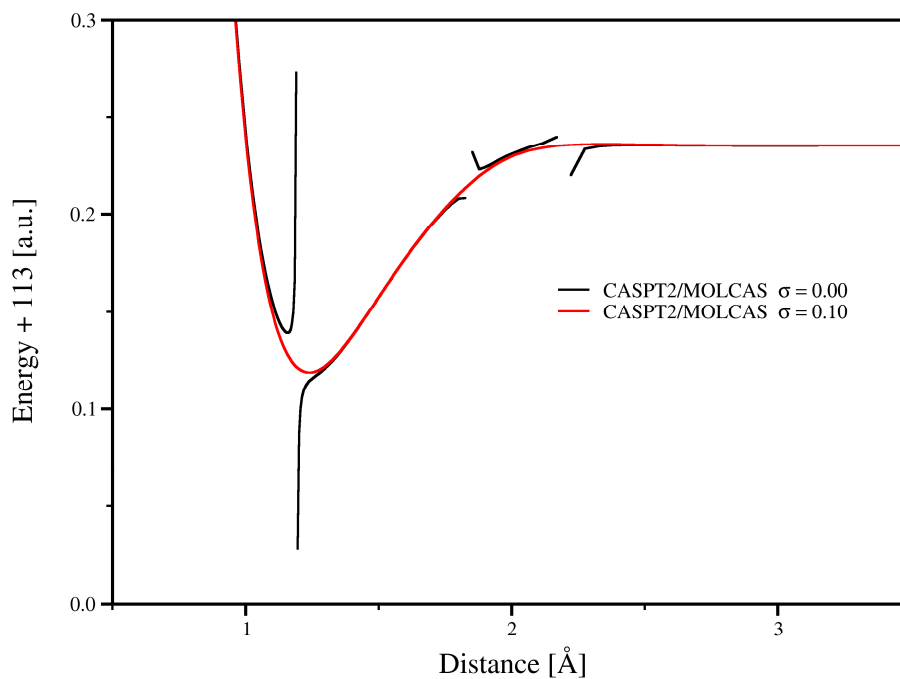


Figure 1.1 CASPT2/MOLCAS potential energy curves computed with two values of the imaginary shift parameter σ for the $A^1\Pi$ excited state of CO.

Figure 1.1 shows the potential energy curves of the excited $^1\Pi$ state of CO obtained from the CASPT2 calculations. The black curve, obtained with the standard CASPT2 method, has a problem with a strong intruder state around 1.2 Å and with weak

intruder states around 1.8 and 2.3 Å. It is clear that the intruder states constitute a serious problem, which distorts the shape of the curve around its minimum causing loosing significant information. Fortunately, introducing shift techniques in perturbation theory calculations can efficiently remove the intruder states. The perturbation theory shift techniques are available in a few flavors: real shift technique⁶, imaginary shift technique⁷, intruder state avoidance (ISA) technique⁸, etc. After applying an intruder state removal technique, the potential energy curve in Figure 1.1 (red curve) became continuous and well-behaving. Recently certain undesired properties of the shift techniques have been discovered. It was found that it is possible to obtain almost arbitrary results in the calculations by using improper shift parameter value because the chemical properties of molecules turned out to depend strongly on the shift parameter.⁹ For example, a possibility of a wrong prediction of the ground state for the scandium dimer was recently communicated due to improper choice of the shift parameter.^{10,11}

Since there is no standard way to select the proper value of the shift parameter, our investigations presented in the body of this Thesis center on the determination of an appropriate determinant applicable for determination of an appropriate value of the shift parameter. We therefore studied the behavior of three types of shift techniques (e.g., real shift, imaginary shift and ISA shift) implemented in three standard chemical programs by performing perturbation theory calculations combined with shift techniques for a set of simple molecules and comparing the resulting spectroscopic constants with experiment. Potential energy curves of 65 low-lying electronic states

of 15 diatomic molecules consisting of the first- or second-periodic elements were studied using different MRPT methods. Subsequently, the resulting spectroscopic constants such as the equilibrium distance, the vibrational frequency and the dissociation energy were calculated for every choice of the shift parameter. The analysis of these results helped us to propose an optimal value of the shift parameter for each of the studied shift techniques. This appropriate choice can reduce the error and eliminate large deviations of spectroscopic constants caused by intruder states or improper selection of the value of the shift parameter.

The detailed introduction about MCSCF, MRPT, intruder states and shift techniques is given in Chapter 2. Our research approaches and the usage of the chemical programs are shown in Chapter 3. The results and discussion of analysis of each shift technique are presented in Chapter 4. The conclusions of this These is shown in Chapter 5. An additional project is present in Appendix A, in which we have used DFT/B3LYP to simulate the IR spectra of *p*-nitroaniline (PNA). The prediction is successful owing to employing an explicitly solvated model of PNA.

Chapter 2

Computational Theory

2.1 The Variational Method

The time-independent Schrödinger equation

$$\hat{H}\Psi = E\Psi \quad (2.1.1)$$

where \hat{H} is the Hamiltonian operator, Ψ is an eigenfunction of \hat{H} , and E is the corresponding eigenvalue, can be conveniently expressed using the bracket notation.

The bra vector $\langle\Psi|$ and the ket vector $|\Psi\rangle$ are defined in the bracket notation as

$$\begin{aligned} \langle\Psi| &\equiv \Psi^* \\ |\Psi\rangle &\equiv \Psi \end{aligned} \quad (2.1.2)$$

Using this notation, the Schrödinger equation in Eq. (2.1.1) can be rewritten as

$$\hat{H}|\Psi\rangle = E|\Psi\rangle \quad (2.1.3)$$

The expectation value of the Hamiltonian and the overlap integral is expressed as

$$\begin{aligned} \langle\Psi|\hat{H}|\Psi\rangle &\equiv \int \Psi^* \hat{H} \Psi d\tau \\ \langle\Psi|\Psi\rangle &= 1 \end{aligned} \quad (2.1.4)$$

In practice, however, it is very complicated to find Ψ . One follows then an indirect

approach in order to find a good approximation to Ψ following so called variational principle^{12,13}. The variational method is an important way to approximate the exact energy of the Schrödinger equation. Assuming that the Hamiltonian operator \hat{H} possess a set of eigenfunctions $|\varphi_i\rangle$ and eigenenergies ε_i , and denoting the ground state energy as ε_0 , we have

$$\hat{H}|\varphi_i\rangle \equiv \varepsilon_i |\varphi_i\rangle \quad (2.1.5)$$

An arbitrary function $|\Phi\rangle$ that obeys the same boundary conditions as the eigenfunctions $|\varphi_i\rangle$ can be expanded in a complete set of the orthonormal functions $|\varphi_i\rangle$

$$|\Phi\rangle = \sum_i c_i |\varphi_i\rangle \quad (2.1.6)$$

Substituting Eq. (2.1.6) into the Schrödinger equation and multiplying by $\langle\Phi|$ on the left side one obtains

$$\begin{aligned} \langle\Phi|\hat{H}|\Phi\rangle &= \sum_j \sum_i c_j^* c_i \varepsilon_i \langle\varphi_j|\varphi_i\rangle \\ &= \sum_j \sum_i c_j^* c_i \varepsilon_j \delta_{ji} \\ &= \sum_i |c_i|^2 \varepsilon_i \end{aligned} \quad (2.1.7)$$

where we assumed that the eigenfunctions $|\varphi_i\rangle$ are orthonormal, $\langle\varphi_j|\varphi_i\rangle = \delta_{ji}$. Since ε_0 is the eigenenergy of the ground state, for all the other eigenenergies $\varepsilon_i \geq \varepsilon_0$. Equation (2.1.7) can be then written as

$$\langle\Phi|\hat{H}|\Phi\rangle = \sum_i |c_i|^2 \varepsilon_i \geq \sum_i |c_i|^2 \varepsilon_0 \quad (2.1.8)$$

Because $\langle \Phi | \Phi \rangle = \sum_j \sum_i c_j^* c_i \delta_{ji} = \sum_i |c_i|^2$, substituting $\langle \Phi | \Phi \rangle$ into right side of Eq. (2.1.8) and rearranging the equation gives

$$\frac{\langle \Phi | \hat{H} | \Phi \rangle}{\langle \Phi | \Phi \rangle} \geq \epsilon_0 \quad (2.1.9)$$

The arbitrary function $|\Phi\rangle$ is called a trial function and the ratio in Eq. (2.1.9) called Rayleigh quotient, expresses the energy of the trial function. Consequently, this ratio shows that the energy of the trial function is always higher than the ground state energy. In order to approach the exact energy, the variational method minimizes the energy via applying appropriate trial function or varying parameters of the trial function.

2.2 The Rayleigh-Schrödinger Perturbation Theory

Perturbation theory provides another route to approach the exact solution^{12,13}.

We can achieve high accuracy of the energy and the wavefunction by including high order corrections. The main idea in perturbation theory is to divide the Hamiltonian operator into the unperturbed operator \hat{H}^0 and the perturbation operator \hat{V}

$$\hat{H} = \hat{H}^0 + \lambda \hat{V} \quad (2.2.1)$$

The time-independent Schrödinger equation Eq. (2.1.3) can be written as

$$(\hat{H}^0 + \lambda \hat{V}) |\Psi_n\rangle = E_n |\Psi_n\rangle \quad (2.2.2)$$

We expand the exact eigenfunctions and the eigenvalues as a Taylor series in λ

$$|\Psi_n\rangle = |\Psi_n^{(0)}\rangle + \lambda |\Psi_n^{(1)}\rangle + \lambda^2 |\Psi_n^{(2)}\rangle + \dots$$

$$E_n = E_n^{(0)} + \lambda E_n^{(1)} + \lambda^2 E_n^{(2)} + \dots \quad (2.2.3)$$

We refer to $|\Psi_n^{(0)}\rangle$ and $E_n^{(0)}$ as the zeroth-order wavefunction and the zeroth-order energy, to $|\Psi_n^{(1)}\rangle$ and $E_n^{(1)}$ as the first-order wavefunction and first-order energy, and so on. Substitution of the wavefunction and the energy as expressed by Eq. (2.2.3) into Eq. (2.2.2) gives

$$(\hat{H}^0 + \lambda \hat{V})(|\Psi_n^{(0)}\rangle + \lambda |\Psi_n^{(1)}\rangle + \lambda^2 |\Psi_n^{(2)}\rangle + \dots) =$$

$$(E_n^{(0)} + \lambda E_n^{(1)} + \lambda^2 E_n^{(2)} + \dots)(|\Psi_n^{(0)}\rangle + \lambda |\Psi_n^{(1)}\rangle + \lambda^2 |\Psi_n^{(2)}\rangle + \dots) \quad (2.2.4)$$

Collecting terms of Eq. (2.2.4) involving the same power of λ , we get

$$\lambda^0 : \hat{H}^0 |\Psi_n^{(0)}\rangle = E_n^{(0)} |\Psi_n^{(0)}\rangle \quad (2.2.5)$$

$$\lambda^1 : \hat{H}^0 |\Psi_n^{(1)}\rangle + \hat{V} |\Psi_n^{(0)}\rangle = E_n^{(0)} |\Psi_n^{(1)}\rangle + E_n^{(1)} |\Psi_n^{(0)}\rangle \quad (2.2.6)$$

$$\lambda^2 : \hat{H}^0 |\Psi_n^{(2)}\rangle + \hat{V} |\Psi_n^{(1)}\rangle = E_n^{(0)} |\Psi_n^{(2)}\rangle + E_n^{(1)} |\Psi_n^{(1)}\rangle + E_n^{(2)} |\Psi_n^{(0)}\rangle \quad (2.2.7)$$

and so on. To simplify the derivation, we can choose the condition $\langle \Psi_n^{(0)} | \Psi_n \rangle = 1$ which is referred to as the intermediate normalization. Multiplying $\langle \Psi_n^{(0)} |$ on left side of wavefunction of Eq. (2.2.3), we have

$$\langle \Psi_n^{(0)} | \Psi_n \rangle = \langle \Psi_n^{(0)} | \Psi_n^{(0)} \rangle + \lambda \langle \Psi_n^{(0)} | \Psi_n^{(1)} \rangle + \lambda^2 \langle \Psi_n^{(0)} | \Psi_n^{(2)} \rangle + \dots = 1$$

Since λ is a variable, we get the orthogonality condition $\langle \Psi_n^{(0)} | \Psi_n \rangle = 0$. Multiplying

$\langle \Psi_n^{(0)} |$ on left side of each equation in Eq. (2.2.5), Eq. (2.2.6) and Eq. (2.2.7) and using the intermediate normalization, we have

$$E_n^{(0)} = \langle \Psi_n^{(0)} | \hat{H}^0 | \Psi_n^{(0)} \rangle \quad (2.2.8)$$

$$E_n^{(1)} = \langle \Psi_n^{(0)} | \hat{V} | \Psi_n^{(0)} \rangle \quad (2.2.9)$$

$$E_n^{(2)} = \langle \Psi_n^{(0)} | \hat{V} | \Psi_n^{(1)} \rangle \quad (2.2.10)$$

The first-order correction energy $E_n^{(1)}$ is the integral of the perturbation operator \hat{V} over the unperturbed wavefunction. We need to correct the energy further because the unperturbed wavefunction is not the exact wavefunction. For finding the second-order correction energy $E_n^{(2)}$, we need to know the first-order correction wavefunction. The first-order correction wavefunction can be expanded as a linear combination of zero-order correction wavefunctions

$$| \Psi_n^{(1)} \rangle = \sum_{m \neq n} | \Psi_m^{(0)} \rangle \langle \Psi_m^{(0)} | \Psi_n^{(1)} \rangle \quad (2.2.11)$$

Using Eq. (2.2.11), the second-order correction energy Eq. (2.2.10) can be written as

$$E_n^{(2)} = \sum_{m \neq n} \langle \Psi_n^{(0)} | \hat{V} | \Psi_m^{(0)} \rangle \langle \Psi_m^{(0)} | \Psi_n^{(1)} \rangle \quad (2.2.12)$$

Substituting Eq. (2.2.11) into Eq. (2.2.6) and then multiplying by $\langle \Psi_m^{(0)} |$ on the left side, we obtain

$$\begin{aligned} \langle \Psi_m^{(0)} | \hat{H}^0 | \Psi_n^{(1)} \rangle + \langle \Psi_m^{(0)} | \hat{V} | \Psi_n^{(0)} \rangle &= \langle \Psi_m^{(0)} | E_n^{(0)} | \Psi_n^{(1)} \rangle + \langle \Psi_m^{(0)} | E_n^{(1)} | \Psi_n^{(0)} \rangle \\ E_m^{(0)} \langle \Psi_m^{(0)} | \Psi_n^{(1)} \rangle + \langle \Psi_m^{(0)} | \hat{V} | \Psi_n^{(0)} \rangle &= E_n^{(0)} \langle \Psi_m^{(0)} | \Psi_n^{(1)} \rangle \end{aligned} \quad (2.2.13)$$

Rearrangement of Eq. (2.2.13) gives

$$\langle \Psi_m^{(0)} | \Psi_n^{(1)} \rangle = \frac{\langle \Psi_m^{(0)} | \hat{V} | \Psi_n^{(0)} \rangle}{E_n^{(0)} - E_m^{(0)}} \quad (2.2.14)$$

Substituting Eq. (2.2.14) into Eq. (2.2.11), we get the first-order correction wavefunction

$$|\Psi_n^{(1)}\rangle = \sum_{m \neq n} \frac{\langle \Psi_m^{(0)} | \hat{V} | \Psi_n^{(0)} \rangle}{E_n^{(0)} - E_m^{(0)}} |\Psi_m^{(0)}\rangle \quad (2.2.15)$$

Substituting Eq. (2.2.14) into the $\langle \Psi_m^{(0)} | \Psi_n^{(1)} \rangle$ of Eq. (2.2.12), we get the second-order correction energy

$$\begin{aligned} E_n^{(2)} &= \sum_{m \neq n} \frac{\langle \Psi_n^{(0)} | \hat{V} | \Psi_m^{(0)} \rangle \langle \Psi_m^{(0)} | \hat{V} | \Psi_n^{(0)} \rangle}{E_n^{(0)} - E_m^{(0)}} \\ &= \sum_{m \neq n} \frac{|\langle \Psi_n^{(0)} | \hat{V} | \Psi_m^{(0)} \rangle|^2}{E_n^{(0)} - E_m^{(0)}} \end{aligned} \quad (2.2.16)$$

The second-order correction energy in Eq. (2.2.16) is given in terms of the unperturbed wavefunctions and energies. It also shows that the main effect of the perturbation comes from the eigenfunctions $|\Psi_m^{(0)}\rangle$, whose energies are located near the energy of the eigenfunction $|\Psi_n^{(0)}\rangle$ because the correction energy is inversely proportional to the zeroth-order energy difference between eigenfunctions $|\Psi_n^{(0)}\rangle$ and $|\Psi_m^{(0)}\rangle$. This form of the perturbation theory is referred to as the Rayleigh-Schrödinger perturbation theory (RSPT); it is widely applied in the quantum chemistry.

2.3 The Hartree-Fock Method

Assuming that electrons move independently in an average field, the many-electron wavefunction can be written as a product of spin orbitals $\chi(x)$ for each electron, where x represents collectively the space and spin coordinates.

$$\Psi = \chi_1(1)\chi_2(2)\dots\chi_N(N) \quad (2.3.1)$$

To satisfy the Pauli exclusion principle, the wavefunction must be antisymmetric with respect to interchange of two electrons. This can be achieved if the wavefunction is written as a normalized Slater determinant $|\Psi_{SD}\rangle$.¹²

$$\begin{aligned} |\Psi_{SD}\rangle &= \frac{1}{\sqrt{N!}} \begin{vmatrix} \chi_1(1) & \chi_2(1) & \cdots & \chi_N(1) \\ \chi_1(2) & \chi_2(2) & \cdots & \chi_N(2) \\ \vdots & \vdots & \ddots & \vdots \\ \chi_1(N) & \chi_2(N) & \cdots & \chi_N(N) \end{vmatrix} \\ &= \frac{1}{\sqrt{N!}} \det[\chi_1(1)\chi_2(2)\dots\chi_N(N)] \end{aligned} \quad (2.3.2)$$

The Born-Oppenheimer approximation describes the motion of N_e electrons in the field of fixed locations of N_n nuclei. The main justification for the Born-Oppenheimer approximation is the observation that the electrons move much faster than the nuclei. The motion of electrons can be decoupled from nuclei to obtain the electronic Hamiltonian operator \hat{H}_e ¹⁴

$$\hat{H}_e = \sum_{i=1}^{N_e} \left(-\frac{1}{2} \nabla_i^2 - \sum_{A=1}^{N_n} \frac{Z_A}{r_{iA}} \right) + \sum_{i=1}^{N_e} \sum_{j>i}^{N_e} \frac{1}{r_{ij}} + \sum_{A=1}^{N_n} \sum_{B>A}^{N_n} \frac{1}{r_{AB}} \quad (2.3.3)$$

The electronic Hamiltonian operator \hat{H}_e is composed of one-electron operators h_i , two-electron operators g_{ij} and the nuclear repulsion operator \hat{V}_{nn}

$$\hat{H}_e = \sum_{i=1}^{N_e} h_i + \sum_{i=1}^{N_e} \sum_{j>i}^{N_e} g_{ij} + \hat{V}_{nn}$$

where

$$h_i = -\frac{1}{2} \nabla_i^2 - \sum_{A=1}^{N_n} \frac{Z_A}{r_{iA}}$$

$$g_{ij} = \frac{1}{r_{ij}}$$

$$\hat{V}_{nn} = \sum_{A=1}^{N_n} \sum_{B>A}^{N_n} \frac{1}{r_{AB}} \quad (2.3.4)$$

Applying the normalized Slater determinant $|\Psi_{SD}\rangle$, the energy of electronic Hamiltonian operator \hat{H}_e is given by

$$\begin{aligned} E &= \langle \Psi_{SD} | \hat{H}_e | \Psi_{SD} \rangle \\ &= \langle \Psi_{SD} | \sum_{i=1}^{N_e} h_i + \sum_{i=1}^{N_e} \sum_{j>i}^{N_e} g_{ij} + \hat{V}_{nn} | \Psi_{SD} \rangle \end{aligned} \quad (2.3.5)$$

At this point, the Slater determinant $|\Psi_{SD}\rangle$ can be expressed conveniently by an antisymmetrizer operator \hat{A} acting on the product of spin orbitals

$$\begin{aligned} |\Psi_{SD}\rangle &= |\hat{A} \chi_1(1) \chi_2(2) \dots \chi_N(N)\rangle \\ \hat{A} &= \frac{1}{\sqrt{N!}} \sum_{n=1}^{N!} (-1)^{p_n} \hat{P}_n \\ &= \frac{1}{\sqrt{N!}} \left(1 - \sum_i \sum_j \hat{P}_{ij} + \sum_i \sum_j \sum_k \hat{P}_{ijk} - \dots \right) \end{aligned} \quad (2.3.6)$$

where \hat{A} can generate $N!$ possible permutations of electron coordinates by

permutation operators such as \hat{P}_{ij} (interchanges two electron coordinates), \hat{P}_{ijk} (interchanges three electron coordinates), etc., and p_n is the number of transpositions. For instance

$$\begin{aligned}
& \left| \hat{A} \chi_1(1) \chi_2(2) \chi_3(3) \right\rangle \\
&= \frac{1}{\sqrt{3!}} (1 - \hat{P}_{12} - \hat{P}_{13} - \hat{P}_{23} + \hat{P}_{123} + \hat{P}_{132}) \chi_1(1) \chi_2(2) \chi_3(3) \\
&= \frac{1}{\sqrt{3!}} [\chi_1(1) \chi_2(2) \chi_3(3) - \chi_2(1) \chi_1(2) \chi_3(3) - \\
&\quad \chi_3(1) \chi_2(2) \chi_1(3) - \chi_1(1) \chi_3(2) \chi_2(3) + \\
&\quad \chi_3(1) \chi_1(2) \chi_2(3) + \chi_2(1) \chi_3(2) \chi_1(3)] \tag{2.3.7}
\end{aligned}$$

For one-electron operator and two-electron operator, we use the antisymmetrizer operator expression of the Slater determinant to simplify the derivation of the Hartree-Fock equations

$$\begin{aligned}
& \langle \Psi_{SD} | \sum_{i=1}^{N_e} h_i + \sum_{i=1}^{N_e} \sum_{j>i}^{N_e} g_{ij} | \Psi_{SD} \rangle \\
&= \langle \hat{A} \chi_1(1) \chi_2(2) \dots \chi_N(N) | \sum_{i=1}^{N_e} h_i + \sum_{i=1}^{N_e} \sum_{j>i}^{N_e} g_{ij} | \hat{A} \chi_1(1) \chi_2(2) \dots \chi_N(N) \rangle \\
&= \langle \chi_1(1) \chi_2(2) \dots \chi_N(N) | \sum_{i=1}^{N_e} h_i + \sum_{i=1}^{N_e} \sum_{j>i}^{N_e} g_{ij} | \hat{A} \hat{A} \chi_1(1) \chi_2(2) \dots \chi_N(N) \rangle \\
&= \sqrt{N!} \left(\langle \chi_1(1) \chi_2(2) \dots \chi_N(N) | \sum_{i=1}^{N_e} h_i + \right. \\
&\quad \left. \sum_{i=1}^{N_e} \sum_{j>i}^{N_e} g_{ij} | \hat{A} \chi_1(1) \chi_2(2) \dots \chi_N(N) \rangle \right)
\end{aligned}$$

$$\begin{aligned}
&= \sqrt{N!} \left(\langle \chi_1(1)\chi_2(2)\dots\chi_N(N) | \sum_{i=1}^{N_e} h_i | \hat{A}\chi_1(1)\chi_2(2)\dots\chi_N(N) \rangle + \right. \\
&\quad \left. \langle \chi_1(1)\chi_2(2)\dots\chi_N(N) | \sum_{i=1}^{N_e} \sum_{j>i}^{N_e} g_{ij} | \hat{A}\chi_1(1)\chi_2(2)\dots\chi_N(N) \rangle \right) \quad (2.3.8)
\end{aligned}$$

For each one-electron operator, only a matrix element without any permutation of electron coordinates survives. The other matrix elements vanish because of orthonormality of the remaining permuted spin orbitals. Choosing the one-electron operator for coordinate of electron 1 as an example, we have

$$\begin{aligned}
&\langle \chi_1(1)\chi_2(2)\dots\chi_N(N) | h_1 | \hat{A}\chi_1(1)\chi_2(2)\dots\chi_N(N) \rangle \\
&= \langle \chi_1(1) | h_1 | \chi_2(1) \rangle \langle \chi_2(2) | \chi_2(2) \rangle \dots \langle \chi_N(N) | \chi_N(N) \rangle - \\
&\quad \langle \chi_1(1) | h_1 | \chi_2(1) \rangle \langle \chi_2(2) | \chi_1(2) \rangle \dots \langle \chi_N(N) | \chi_N(N) \rangle - \dots \\
&= \langle \chi_1(1) | h_1 | \chi_1(1) \rangle \\
&= h_1(1) \quad (2.3.9)
\end{aligned}$$

For each two-electron operator, only two types of matrix elements survive. One is the term without any permutation, and in the other two electron coordinates are interchanged. Choosing the two-electron operator for coordinates of electron 1 and electron 2 as an example, we have

$$\begin{aligned}
&\langle \chi_1(1)\chi_2(2)\dots\chi_N(N) | g_{12} | \hat{A}\chi_1(1)\chi_2(2)\dots\chi_N(N) \rangle \\
&= \langle \chi_1(1)\chi_2(2)\dots\chi_N(N) | g_{12} | (1 - \hat{P}_{12})\chi_1(1)\chi_2(2)\dots\chi_N(N) \rangle
\end{aligned}$$

$$\begin{aligned}
&= \langle \chi_1(1)\chi_2(2)\dots\chi_N(N) | g_{12} | \chi_1(1)\chi_2(2)\dots\chi_N(N) \rangle - \\
&\quad \langle \chi_1(1)\chi_2(2)\dots\chi_N(N) | g_{12} | \chi_2(1)\chi_1(2)\dots\chi_N(N) \rangle \\
&= \langle \chi_1(1)\chi_2(2) | g_{12} | \chi_1(1)\chi_2(2) \rangle - \langle \chi_1(1)\chi_2(2) | g_{12} | \chi_2(1)\chi_1(2) \rangle \\
&= J_{12} - K_{12} \tag{2.3.10}
\end{aligned}$$

The J_{12} matrix element is called the Coulomb integral and the K_{12} matrix element is called the exchange integral. Nuclear repulsion operator integrates to a constant because it is independent of the electron coordinates. We can simply write

$$\begin{aligned}
&\langle \Psi_{SD} | \hat{V}_{nn} | \Psi_{SD} \rangle \\
&= \hat{V}_{nn} \langle \Psi_{SD} | \Psi_{SD} \rangle \\
&= \hat{V}_{nn} \tag{2.3.11}
\end{aligned}$$


As mentioned above, the energy Eq. (2.3.5) can be written as

$$\begin{aligned}
E &= \sum_{i=1}^{N_e} h_i(i) + \sum_{i=1}^{N_e} \sum_{j>i}^{N_e} (J_{ij} - K_{ij}) + \hat{V}_{nn} \\
&= \sum_{i=1}^{N_e} \langle \chi_i(i) | h_i | \chi_i(i) \rangle - \frac{1}{2} \sum_{i=1}^{N_e} \sum_{j=1}^{N_e} (J_{ij} - K_{ij}) + \hat{V}_{nn} \tag{2.3.12}
\end{aligned}$$

To derive the Hartree-Fock equations, we minimize the energy by using the Lagrange method of undetermined multipliers.¹⁵ Constructing the Lagrange function L , we define

$$L = E - \sum_i^{N_e} \sum_j^{N_e} \epsilon_{ij} [\langle \chi_i(i) | \chi_j(j) \rangle - \delta_{ij}] \quad (2.3.13)$$

where ϵ_{ij} is a Lagrange multiplier. Setting the variation of the energy to zero, we have

$$\delta L = \delta E - \sum_i^{N_e} \sum_j^{N_e} \epsilon_{ij} [\langle \delta \chi_i(i) | \chi_j(j) \rangle + \langle \chi_i(i) | \delta \chi_j(j) \rangle] = 0$$

where

$$\begin{aligned} \delta E = & \sum_{i=1}^{N_e} [\langle \delta \chi_i(i) | h_i | \chi_i(i) \rangle + \langle \chi_i(i) | h_i | \delta \chi_i(i) \rangle + \\ & \frac{1}{2} \sum_{i=1}^{N_e} \sum_{j=1}^{N_e} [\langle \delta \chi_i(i) \chi_j(j) | g_{ij} | \chi_i(i) \chi_j(j) \rangle + \\ & \langle \chi_i(i) \delta \chi_j(j) | g_{ij} | \chi_i(i) \chi_j(j) \rangle + \langle \chi_i(i) \chi_j(j) | g_{ij} | \delta \chi_i(i) \chi_j(j) \rangle + \\ & \langle \chi_i(i) \chi_j(j) | g_{ij} | \chi_i(i) \delta \chi_j(j) \rangle - \langle \delta \chi_i(i) \chi_j(j) | g_{ij} | \chi_i(i) \chi_j(j) \rangle - \\ & \langle \chi_i(i) \delta \chi_j(j) | g_{ij} | \chi_j(i) \chi_i(j) \rangle - \langle \chi_i(i) \chi_j(j) | g_{ij} | \delta \chi_j(i) \chi_i(j) \rangle - \\ & \langle \chi_i(i) \chi_j(j) | g_{ij} | \chi_j(i) \delta \chi_i(j) \rangle] \end{aligned} \quad (2.3.14)$$

The summation of both first and second terms in square brackets of δE for all i and j is identical. The first and third terms in square brackets of δE are complex conjugated with regard to each other. We can recognize similar pattern also in other terms and obtain

$$\delta L = \sum_{i=1}^{N_e} \langle \delta \chi_i(i) | h_i | \chi_i(i) \rangle + \sum_{i=1}^{N_e} \sum_{j=1}^{N_e} [\langle \delta \chi_i(i) \chi_j(j) | g_{ij} | \chi_i(i) \chi_j(j) \rangle -$$

$$\langle \delta\chi_i(i)\chi_j(j) | g_{ij} | \chi_j(i)\chi_i(j) \rangle - \varepsilon_{ij} \langle \delta\chi_i(i) | \chi_j(j) \rangle +$$

complex conjugate = 0 (2.3.15)

At this point, we define two operators for convenience

$$J_j(i) | \chi_i(i) \rangle = \langle \chi_j(j) | g_{ij} | \chi_j(j) \rangle | \chi_i(i) \rangle$$

$$K_j(i) | \chi_i(i) \rangle = \langle \chi_j(j) | g_{ij} | \chi_j(i) \rangle | \chi_i(j) \rangle$$

(2.3.16)

Where $J_j(i)$ is known as the Coulomb operator and $K_j(i)$ is known as the exchange operator. Both descriptions of two operators treat an affected electron as a mean field formed from other electrons. Substituting Eq. (2.3.16) into Eq. (2.3.15), we have

$$\delta L = \sum_{i=1}^{N_e} \langle \delta\chi_i(i) | \left\{ h_i | \chi_i(i) \rangle + \sum_{j=1}^{N_e} [J_j(i) - K_j(i)] | \chi_i(i) \rangle - \sum_{j=1}^{N_e} \varepsilon_{ij} | \chi_i(i) \rangle \right\} + \text{complex conjugate} = 0$$

(2.3.17)

Since $\langle \delta\chi_i(i) |$ is arbitrary, the terms in the braces must be zero for all i

$$\left\{ h_i + \sum_{j=1}^{N_e} [J_j(i) - K_j(i)] \right\} | \chi_i(i) \rangle = \sum_{j=1}^{N_e} \varepsilon_{ij} | \chi_i(i) \rangle$$

$$f_i | \chi_i(i) \rangle = \sum_{j=1}^{N_e} \varepsilon_{ij} | \chi_i(i) \rangle$$

(2.3.18)

The Fock operator f_i is defined as the quantity in the braces in Eq. (2.3.18). We can diagonalize the matrix of the Lagrange multipliers ε_{ij} by an appropriate unitary transformation

$$f_i | \chi_i(i) \rangle = \varepsilon_i | \chi_i(i) \rangle$$

(2.3.19)

The equations (2.3.19) are referred to as the Hartree-Fock (HF) equations. In HF equations, the definitions of the Coulomb operator $J_j(i)$ and the exchange operator $K_j(i)$ depend on the spin orbitals of all electrons. Hence we need to employ the self-consistent field (SCF) method to solve the HF equations iteratively until the total energy and wavefunction are converged, and get the HF energy. That is to say that the minimized energy and optimized wavefunction are determined when their differences from the previous iteration are both under acceptable thresholds respectively.

2.4 Configuration State Function

The Hartree-Fock method treats the interactions between electrons only in an average way. It neglects the instantaneous Coulombic interactions between electrons. The difference of exact nonrelativistic energy E_{non} and Hartree-Fock energy E_{HF} is usually called the correlation energy E_{corr} ¹²

$$E_{\text{corr}} = E_{\text{non}} - E_{\text{HF}} \quad (2.4.1)$$

Considering that the Hartree-Fock wavefunction, constructed as a single Slater determinant, does not properly describe the character of the exact wavefunction, we can account for the electron correlation by constructing a wavefunction including many determinants, or equivalently, many configuration state functions (CSF). The configuration state functions consist of all spin symmetry-adapted singly excited determinants Φ_a^r , doubly excited determinants Φ_{ab}^{rs} , triply excited determinants Φ_{abc}^{rst} , etc.

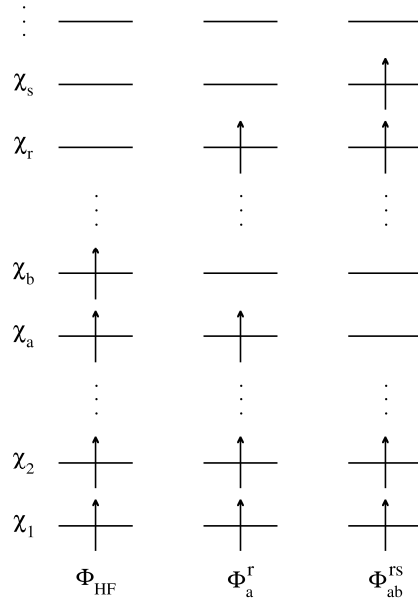


Figure 2.1 Excited determinants formed from a HF determinant.¹⁵

The configuration interaction (CI) method using following CI wavefunctions and, employs variational method to optimize the CI wavefunctions and the energy. The CI wavefunction Ψ_{CI} is constructed as a linear combination of the CSFs

$$\Psi_{CI} = C_{HF} \Phi_{HF} + \sum_{a,r} C_a^r \Phi_a^r + \sum_{\substack{a<b \\ r<s}} C_{ab}^{rs} \Phi_{ab}^{rs} + \sum_{\substack{a<b<c \\ r<s<t}} C_{abc}^{rst} \Phi_{abc}^{rst} + \dots$$

where C_a^r , C_{ab}^{rs} , C_{abc}^{rst} , etc. are CI coefficients and

$$\begin{aligned} \Phi_{HF} &= \frac{1}{\sqrt{N!}} \det |\chi_1 \chi_2 \dots \chi_a \chi_b \dots \chi_n| \\ \Phi_a^r &= \frac{1}{\sqrt{N!}} \det |\chi_1 \chi_2 \dots \chi_r \chi_b \dots \chi_n| \\ \Phi_{ab}^{rs} &= \frac{1}{\sqrt{N!}} \det |\chi_1 \chi_2 \dots \chi_r \chi_s \dots \chi_n| \end{aligned} \quad (2.4.2)$$

and so on.

Including all possible CSFs in the CI calculations results in so-called full CI (FCI) method, which reproduces the exact solutions when used with an infinite basis set and small basis sets. Unfortunately, we cannot use infinite basis sets. On the other hand, the number of CSFs in the FCI calculations is too large even for very small molecules. Suppose we have M spatial wavefunctions, from which we can construct $2M$ spin orbitals, and N electrons. The total number of the CSFs is $\binom{2M}{N}$. Taking into account only CSFs with proper spin multiplicity $(2S+1)$, the number of CSFs is expressed by Weyl's formula¹⁶ as

$$\frac{2S+1}{M+1} \binom{M+1}{\frac{1}{2}N-S} \binom{M+1}{\frac{1}{2}N+S+1} \quad (2.4.3)$$

where S is the spin angular momentum. For instance, the calculation for H_2O with a small basis set, 6-31(d) containing 19 basis set functions and 10 electrons. The total number of singlet CSFs is 3.0×10^7 , which is extremely large. Thus we need to deal with a matrix with size 3.0×10^7 by 3.0×10^7 . For this reason, the FCI calculation is not feasible for general systems.

2.5 The Multiconfiguration Self-Consistent Field Method

The multiconfiguration self-consistent field (MCSCF) method is particularly important for excited states calculations, quasi-degenerate systems, and biradical structures. The MCSCF wavefunction is constructed as a linear combination of CSFs containing not only the CI coefficients, but also the coefficients of molecular orbitals.

Simultaneous optimization of both the CI coefficients and the molecular orbital coefficients leads to demanding computations but we can get good results by choosing only a few chemically important CSFs. The MCSCF method is an approximation of the CI method. A common strategy is the complete active space self-consistent field (CASSCF) method¹⁷. The concept of complete active space (CAS) is based on division of the orbitals into inactive orbitals, active orbitals and virtual orbitals (see Figure 2.2). Characteristics of the three classes of orbitals are as follows:

- The inactive orbitals are always doubly occupied.
- The active orbitals allow all possible occupations (0, 1, or 2).
- The virtual orbitals are always empty.

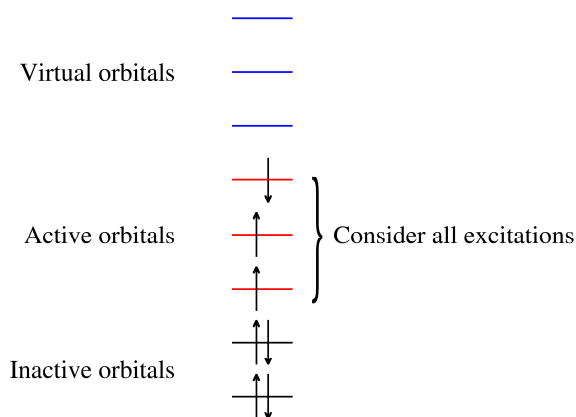


Figure 2.2 Illustration of complete active space.

The electrons except the electrons within inactive orbitals are called active electrons. The CSF basis is constructed by forming all possible distributions of active electrons among active orbitals. This ansatz allows for serious reduction of the computing time.

2.6 The Multireference Perturbation Theory

In applications of the Rayleigh-Schrödinger perturbation theory, one needs to define zeroth-order Hamiltonian and the remaining perturbation operator. For instance, the single reference Møller-Plesset perturbation theory adopts the zero-order Hamiltonian \hat{H}^0 and perturbed operator \hat{V} as

$$\hat{H}^0 = \sum_{i=1}^{N_e} f_i$$

$$\hat{V} = \hat{H}_c - \hat{H}^0 = \sum_{i=1}^{N_e} \sum_{j>i}^{N_e} \frac{1}{r_{ij}} - \sum_{i=1}^{N_e} \sum_{j=1}^{N_e} [J_j(i) - K_j(i)] \quad (2.6.1)$$

The perturbation \hat{V} is the difference of between the two-electron potential in the original electronic Hamiltonian and in the Fock operator. For multiconfigurational systems, the multireference perturbation theories (MRPT) adopt slightly more complicated form of the zero-order Hamiltonian. The use of the CASSCF wavefunction as the zero-order wavefunction combined with perturbation theory is referred to as the complete active space perturbation theory (CASPT2) developed by Roos et al. The second-order perturbation theory correction to energy is given by

$$E_\alpha^{(2)} = \sum_k \frac{|\langle \alpha | \hat{V} | k \rangle|^2}{E_\alpha^{(0)} - E_k^{(0)}} \quad (2.6.2)$$

where α indicates the CASSCF reference state and k indicates a singly or doubly excited intermediate state. Other popular variants of perturbation theories are the multireference Møller-Plesset perturbation theory (MRMP) and the multiconfigurational quasidegenerate perturbation theory (MCQDPT) developed by

Hirao and Nakano. In fact, the MRMP and MCQDPT are the same in case of single state calculation. The MRPT methods mentioned above could occur divergences due to the intruder states. Recently, n-electron valence state perturbation theory (NEVPT2), one of the MRPT methods, was developed by Angeli et al., and is characterized by absence of intruder states.

In order to reduce the systematic error in CASPT2, two modifications of the zero-order Hamiltonian were proposed. One is adding a correction function such as g_1 , g_2 or g_3 to the zero-order Hamiltonian¹⁸. The other is introducing the IPEA-shift¹⁹ in the definition of the zero-order Hamiltonian. Because of the success of the IPEA-shift applicable to CASPT2 calculations, the default value (0.25 a.u.) of the IPEA-shift has been employed in the MOLCAS chemical program. In this study, we also investigated the CASPT2 with the g_1 correction and CASPT2 with IPEA-shift.

2.7 Intruder States and Shift Techniques

Intruder states appear in the MRPT calculations when the difference between the zero-order energy of the reference state and of an excited intermediate state in the Eq. (2.6.2) is small ($E_\alpha^{(0)} \approx E_k^{(0)}$). Consequently, the second-order correction energy $E_\alpha^{(2)}$ may become extremely large, approaching $+\infty$ or $-\infty$ in the limit of a perfect degeneracy. The occurrence of the intruder state result in overcorrection, discontinuity of potential energy surface and irrational chemical information.

Such problems can be solved by including more appropriate orbitals in the active

space, as usually a poor choice of CSFs describing the electronic structure is the origin of the intruder state problem. However, in most situations such calculations are not feasible. A convenient way to avoid intruder states is using shift techniques that introduce a shift parameter σ in the denominator of the Eq. (2.6.2) to prevent it from vanishing

$$E_{\alpha}^{(2)} = \sum_k \frac{|\langle \alpha | \hat{V} | k \rangle|^2}{E_{\alpha}^{(0)} - E_k^{(0)} + \sigma} \quad (2.7.1)$$

The following shift techniques were developed by using different definition of the shift parameter. The level shift technique using real value as the shift parameter is called here as the real shift technique. The imaginary level shift technique uses an imaginary shift parameter $i\sigma$. The intruder state avoidance (ISA) technique employed in MCQDPT and MRMP methods defines the shift parameter as

$$\sigma = \frac{b}{E_{\alpha}^{(0)} - E_k^{(0)}} \quad (2.7.2)$$

where b is a small constant at our disposal. Although shift techniques can eliminate intruder states effectively, these modifications may sometimes lead to wrong information without any chemical or physical meaning.

Chapter 3

Computational Details

The potential energy curves of 15 diatomic molecules have been determined with Dunning's augmented correlation-consistent polarized valence triple zeta (aug-cc-pVTZ) basis sets. The total number of low-lying electronic states considered in the Thesis is 65. The selected molecules consisted of first or second row elements. The list of low-lying electronic states for each selected molecule and their experimental spectroscopic constants are given in Table 1 and Table 2, respectively.

The CASSCF calculations are the first step in the multireference perturbation treatment. For molecules with more than one electronic state, we adopted here the state-averaged CASSCF approach. Otherwise, the state-specific CASSCF approach is used for single state calculation. Both state-averaged and state-specific CASSCF calculations were performed with MOLPRO (version 2009) program.^{20,21} A computational strategy employing full valence space including all valence orbitals and valence electrons was adopted for the studied here molecules. To provide appropriate CASSCF wavefunctions for the subsequent MRPT calculations, it is important to take care of the potential energy curves of the studied low-lying electronic states for each molecule. We look particular care for every potential energy curves to assume continuity and well-behaving character of the curves through the

full range of the standard distances.

All the MRPT methods employed the same reference wavefunctions defined as the CASSCF wavefunctions. We attempted to uniformly take this CASSCF wavefunctions into GAMESS (2009) and MOLCAS (version 7.4) programs. However, the GAMESS program has a distinct definition of the atomic orbitals from the other programs. The atomic orbital Ψ_{nlm} consists of the radial part $R_n(r)$ and the angular part $Y_l^m(\theta, \varphi)$

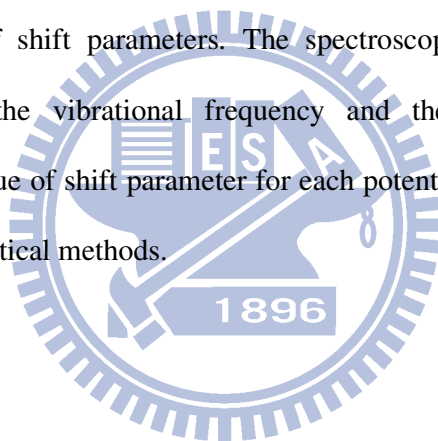
$$\Psi_{nlm} = NR_n(r)Y_l^m(\theta, \varphi)$$

where N is normalized constant. The angular part can be described as two following types of functions; the Cartesian type is used in the GAMESS program while the spherical harmonic type is used in the other programs. The coefficients of these two types of orbitals can be converted to each other as shown in Table 3. Accordingly, the CASSCF wavefunctions obtained from the MOLPRO can be applied to the other programs.

Three different shift techniques applicable to multireference perturbation theories were studied in present Thesis. The real shift technique was used for CASPT2 implemented in MOLPRO program. We refer to these calculations as CASPT2/MOLPRO. We investigated the shift parameter from 0.0 to 1.0 a.u. The ISA technique was used together with MCQDPT and MRMP, both implemented in GAMESS program. The range of the shift parameter was from 0.0 to 0.5 a.u. Because MRMP is a special case of MCQDPT, we refer to both of these calculations as MCQDPT/GAMESS. The imaginary shift technique was used together with CASPT2

implemented in MOLCAS program. The range of the employed shift parameter was from 0.0 to 1.5 a.u. We refer to these calculations as CASPT2/MOLCAS. A related CASPT2/MOLCAS calculation using additional 0.25 a.u. IPEA shift are referred to as IPEA-CASPT2/MOLCAS. Finally, the last studied method was CASPT2 with the g1 correction referred to as G1-CASPT2/MOLCAS.

The maximal value of the studied shift parameter was chosen as a very large number, which is typically much larger than usual choice done in quantum chemical calculations. The reason for such a choice comes from the fact that we wanted to cover a large range of shift parameters. The spectroscopic constants (e.g., the equilibrium distance, the vibrational frequency and the dissociation energy) determined for each value of shift parameter for each potential curve were critically evaluated by using statistical methods.



Chapter 4

Results and Discussion

4.1 Potential Energy Curves

Potential energy curves of diatomic molecules provide the simplest way to test various quantum chemical techniques. In this project we determine equilibrium constants R_e , vibrational frequencies ω_e , and dissociation energies D_e in order to evaluate the accuracy of various multireference perturbation theories using the shift techniques. The calculated spectroscopic constants can be critically assessed by comparison with accurate experimental data derived from vibrational spectroscopy. For theoretical calculations, it is convenient to use only one variable, the distance between two atoms, to simplify the complicated chemical problems and compare with experiment.

The potential energy curves of the 65 low-lying electronic states of 15 molecules are constructed by performing over 150 single point calculations for each curve. The set of interatomic distances was chosen to cover the full range from the dissociation limit (around 8 Å) to short distances (around 0.6 Å) for each studied state. The points around the minimum of the curves are chosen very densely with the interval of 0.005 Å. This allows us to compute accurately the spectroscopic constants around equilibrium in the MRPT calculations.

Before constructing the potential energy curves of the MRPT methods, we need to obtain appropriate CASSCF wavefunctions for each diatomic molecule. However, there is a problem that the CASSCF wavefunctions do not reproduce completely the same results in the different programs due to difference of code implementation. An idea of our project is to transfer the CASSCF wavefunctions from the MOLPRO program to the GAMESS and MOLCAS programs. We demonstrate that this idea is feasible because the reference energies of various MRPT methods are exactly the same. Choosing the MOLRPO program has an advantage for the state-averaged CASSCF calculations. This program can simultaneously optimize several electronic states in the CASSCF calculations containing different symmetries or spin multiplicities. Therefore, we can obtain a set of the CASSCF wavefunctions to satisfy the studied states of each diatomic molecule. The use of the CASSCF wavefunctions gives us a uniform way to investigate the potential energy curves of the MRPT methods.

4.2 Intruder States

Intruder states occur in the MRPT calculations because of the appearance of very small denominators in the second-order energy correction. Figure 4.1 shows the potential energy curves of the $^5\Pi$ state and $^1\Pi$ state of CO. The potential energy curve of the $^5\Pi$ state of CO is not affected by intruder states. The curve of the $^1\Pi$ state of CO is affected by intruder states, which cause a discontinuity at approximately 1.29 Å

appearing around the minimum of the curve, analogous to the black line in Figure 1.1 in Chapter 1. As the result, we cannot compute spectroscopic constants for this curve. Summarizing, the presence of the intruder states leads to a discontinuity in the potential energy surface, which completely distorts the information normally available for the MRPT methods.

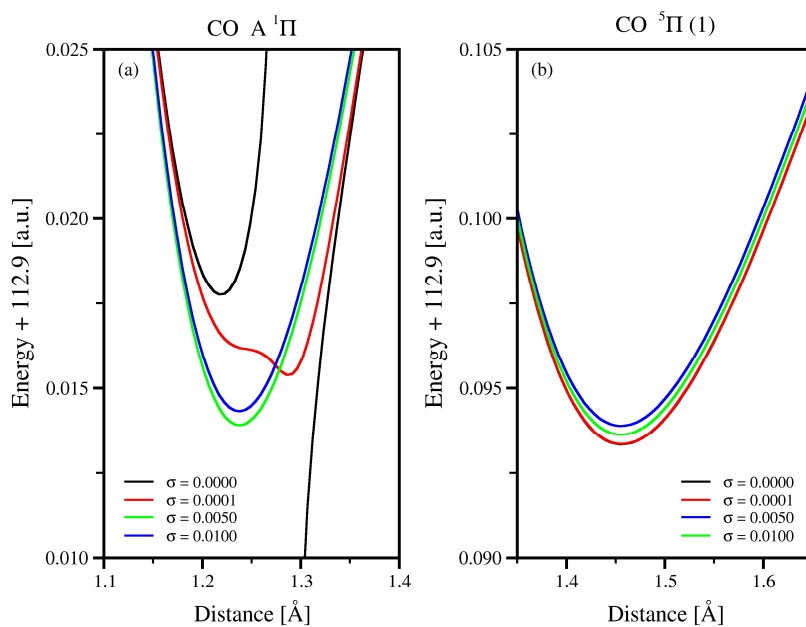


Figure 4.1 MCQDPT/GAMESS potential energy curves with various values of shift parameter σ for the excited ${}^5\Pi$ state (a) and ${}^1\Pi$ (b) state of CO.

4.3 Effect of Using Intruder State Removal Techniques:

General Observations

Intruder state removal techniques are the most efficient way to eliminate the intruder states and produce a smooth potential energy curves. These techniques

introduce a shift parameter σ in the denominator of Eq. (2.6.2) to prevent the appearance of infinities in the second-order energy correction. The process of the intruder states elimination is shown in Figure 4.1b. The shifted potential energy curve is still slightly distorted when a small shift parameter ($\sigma = 0.0001$ a.u.) is used. Using a larger value of the shift parameter ($\sigma = 0.0050$ a.u.) is enough to remove the intruder state completely. However, using even larger a value of the shift parameter ($\sigma = 0.0100$ a.u.) removes the discontinuity equally well, but simultaneously affects the shape of the potential energy curve. On the other hand, a potential energy curve not affected by the intruder states (see Figure 4.1a) does also change its shape and is affected by the choice of the shift parameter. It is clear that the shift techniques can have the substantial influence on the determination of various chemical properties.

4.4 Effect of Using Intruder State Removal Techniques:

Details

To investigate how the shift parameter affects the chemical properties of the diatomic molecules, we constructed the potential energy curves of the 65 low-lying electronic states using different MRPT methods. Subsequently, we computed the resulting spectroscopic constants with various values of the shift parameter. The spectroscopic constants are shown in Figures 6.1-6.65. Figure 4.2 gives as an example the results for the $^1\Pi$ state of CO obtained with different methods as a function of the shift parameter.

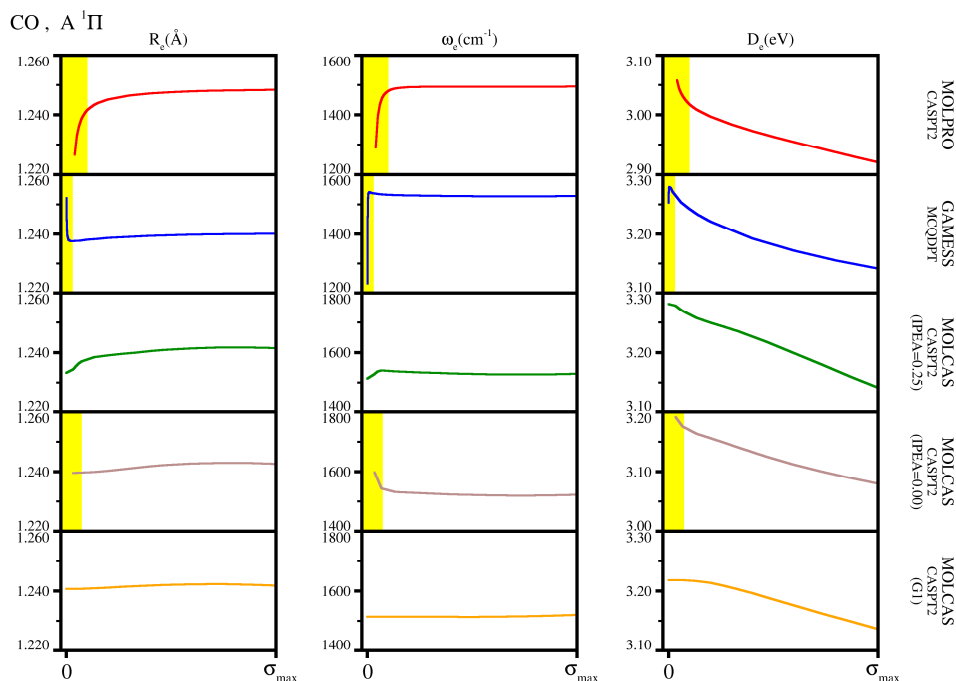
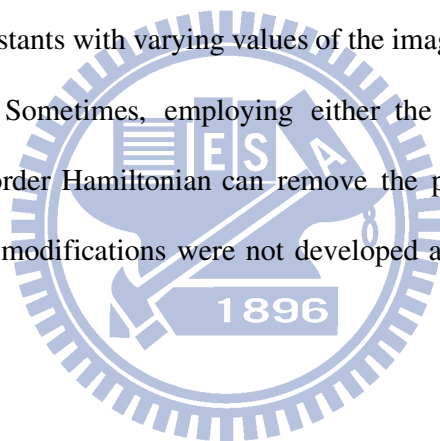


Figure 4.2 Spectroscopic constants for the A $^1\Pi$ state of CO obtained using different methods with various values of the shift parameter σ .

In this figure, the left column corresponds to R_e , the middle column, to ω_e , and the right column, to D_e . The maximal shift parameter σ_{\max} is 1.0 a.u. for the real shift parameter, 0.5 a.u. for the ISA shift parameter, and 1.5 a.u. for the imaginary shift parameter. Some of the plots display yellow boxes for small values of the shift parameter. Such a region indicates an unusually large change of a given spectroscopic constant. The main reason for such a behavior is that the potential energy curve is strongly distorted by intruder states and small values of the shift parameter cannot eliminate such a strong distortion.

The behavior of the spectroscopic constants for various values of the shift

parameter shows some regular patterns. In the CASPT2/MOLPRO method, a larger value (0.3 a.u.) of the real shift parameter is required to eliminate intruder states because the potential energy curves are often distorted by very strong intruder states around the curve minima or at the long interatomic distances. In the MCQDPT/GAMESS method, the intruder states could be completely removed even by small value (0.001 a.u.) of the ISA shift parameter. However, the changes of spectroscopic constants show large dependence on the value of σ for small values of the shift parameter (see Figure 4.2). In the CASPT2/MOLCAS methods, the behavior of the spectroscopic constants with varying values of the imaginary shift parameter is similar in most cases. Sometimes, employing either the IPEA shift or the g_1 correction in the zero-order Hamiltonian can remove the problem of the intruder state even if these two modifications were not developed as a remedy for intruder states elimination.



4.5 Statistical Analysis for Intruder State Removal Techniques

4.5.1 Distribution of Changes in Spectroscopic Constants

The statistical analysis was performed to investigate the changes in the spectroscopic constants induced by variation of the intruder state removal parameter. The changes of spectroscopic constants (ΔR_e , $\Delta \omega_e$, and ΔD_e) were defined in the

following way. The minimal and maximal values of R_e in the CASPT2/MOLPRO calculations shown in Figure 4.2 are 1.225 and 1.250 Å respectively. The change of R_e between the minimal and maximal values is 0.025 Å. We refer to this change of R_e as ΔR_e . Analogously, the change of ω_e referred to as $\Delta\omega_e$ is 200 cm^{-1} and the change of D_e referred to as ΔD_e is 0.13 eV. We analyzed statistically the distributions of ΔR_e , $\Delta\omega_e$, and ΔD_e in Figures 6.1-6.65. The results of these distributions are shown in Figures 6.66, Figure 6.68, and Figure 6.70. For example, Figure 6.66 presents the distributions of ΔR_e in the form of five histograms correspond to five methods. In every histogram, each column corresponds to a number of states characterized by the same ΔR_e .

The Figures 6.67, 6.69 and 6.71 give similar analysis for observing the effect of the small values of the shift parameter upon the distributions. We analyzed the ΔR_e , $\Delta\omega_e$ and ΔD_e ignoring the values of spectroscopic constants which are located in the yellow boxes in Figures 6.1-6.65. For instance, the maximal value of ΔD_e observed from CASPT2/MOLPRO shown in Figure 4.2 changes from 3.05 to 3.00 eV after ignoring in the yellow box region.

We can observe the effect of small values of the shift parameter on ΔR_e through comparing the distributions shown in Figures 6.66 and 6.67. The similar effect is also provided from the distributions of $\Delta\omega_e$ shown in Figures 6.68 and 6.69, and ΔD_e shown in Figures 6.70 and 6.71. The CASPT2/MOLPRO, MCQDPT/GAMESS, and CASPT2/MOLCAS methods show significant reduction of large deviations achievable by ignoring the yellow box regions. Namely, using larger values of the

shift parameter in these methods can reduce the changes of spectroscopic constants induced by the intruder states. On the other side, the IPEA-CASPT2/MOLCAS and G1-CASPT2/MOLCAS methods cannot produce the improved results in that approach. The modified CASPT2/MOLCAS calculations with too large value of the shift parameter can actually lead to larger changes of the spectroscopic constants.

4.5.2 Mean Absolute Deviations from Experiments for Spectroscopic Constants

The critical evaluations of shift techniques applicable to perturbation theory were investigated by means of absolute deviations of the spectroscopic constants for experiment. We computed the absolute deviations between the computed results (Figures 6.1-6.65) and the experimental data (Table 2). The mean absolute deviations of R_e , ω_e and D_e were presented in Figures 6.72-6.86. Some of the experiment data are not available so the total number of experimental data for R_e , ω_e , and D_e is 55, 54, and 55, respectively. Figure 6.72 shows the mean absolute deviations of R_e for the CASPT2/MOLCAS calculations. The number in blue denotes the total number of physically valid results. For small shifts, some of the potential energy curves severely plagued with the intruder states prohibiting one from computing the spectroscopic constants.

For the CASPT2/MOLPRO method, the mean absolute deviations of spectroscopic constants decrease with varying the shift values for R_e and ω_e , and

remain constant for D_e (see Figures 6.72, 6.77, and 6.82). For the MCQDPT/GAMESS method, the mean absolute deviations of spectroscopic constants (see Figures 6.78, 6.73, and 6.83) are reduced significantly for large values of the shift parameter (>0.002 a.u.). The IPEA-CASPT2/MOLCAS, CASPT2/MOLCAS, and G1-CASPT2/MOLCAS methods display the similar tendency of the mean absolute deviations for each spectroscopic constant. The mean absolute deviations begin to increase for R_e , and ω_e if the large values of the shift parameter (> 0.6 a.u.) were employed, and decrease for D_e (see Figures 6.74-6.76, 6.79-6.81, and 6.84-6.86).

4.5.3 Optimal Values of Shift Techniques

To find the optimal value of the shift parameter for each method, we computed the combined error for all the spectroscopic constants. The combined error of each method is shown in Figure 4.3. The definition of the combined error is a summation of each mean absolute deviation divided by the accuracy units. The accuracy units are chosen as 0.001 \AA for R_e , 1 cm^{-1} for ω_e , and 0.01 eV for D_e . For example, the CASPT2/MOLPRO calculations with $\sigma = 0.0$ (see Figures 6.72, 6.77, and 6.82), the mean absolute deviations of the spectroscopic constants are 0.0107 \AA for R_e , 42.6 cm^{-1} for ω_e , and 0.2268 eV for D_e ; therefore, the combined error is

$$\text{combined error} = \frac{0.0107}{0.001} + \frac{42.6}{1} + \frac{0.2268}{0.01} \approx 76$$

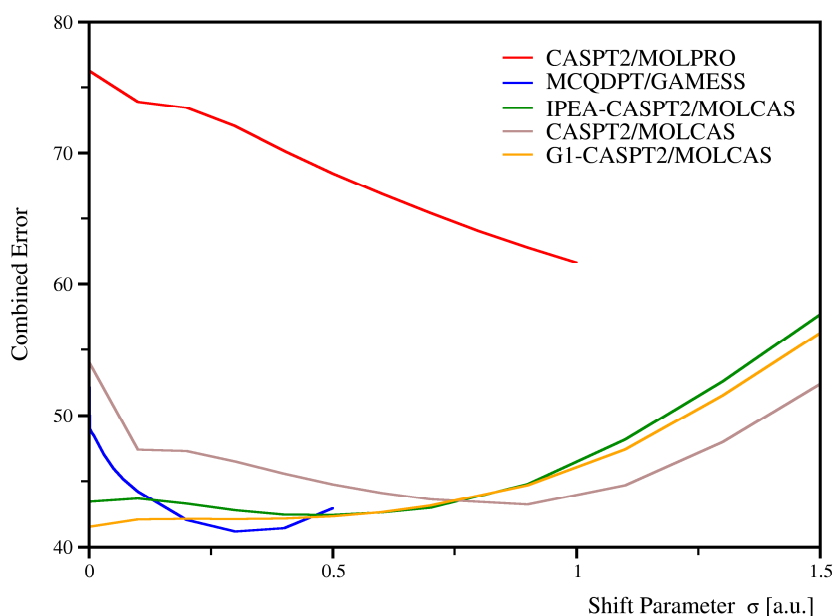


Figure 4.3 Combined errors with various values of the shift parameter for different methods.

The optimal value was determined by evaluating of the combined error for each shift technique. In the CASPT2/MOLPRO calculations, the optimal value of the real shift parameter is 1.0 a.u., which shows that the larger shift parameters can reduce the deviations of the spectroscopic constants. We also suggest that the value of the shift parameter should be larger than 0.4 a.u. for eliminating the intruder states. In the MCQDPT/GAMESS calculations, we propose the optimal value of the ISA shift parameter is 0.3 a.u. using the analogous analysis. In the IPEA-CASPT2/MOLCAS, CASPT2/MOLCAS and G1-CASPT2/MOLCAS methods, we uniformly propose the optimal value of the imaginary parameter is 0.6 a.u. due to the similar behavior of these methods. Using larger values of the shift parameter shall increase the combined

error for all the CASPT2/MOLCAS methods. Comparing with the CASPT2/MOLCAS method, the combined errors of the modified CASPT2/MOLCAS methods already show a good improvement and present almost a constant within the small values of the shift parameter.

The shift techniques cannot only eliminate the intruder states but also reduce the systematic error. We give two following views. First, the variational method in quantum chemistry always shows an overestimation of the exact energy; however, the second-order perturbation theory generally gives us an underestimated energy owing to the over correction energies. Second, if the infinite large value of the shift parameter is used in the MRPT calculations, the correction energies are almost zero. The MRPT calculations shall present as the CASSCF level. Therefore, employing the shift techniques suitably can balance this over corrections of the second-order perturbation treatment and close to the exact energy. In the past, the customary value of the shift parameter used in MRPT calculations has generally not been larger than 0.4 a.u. for the real shift parameter^{22,23}, 0.05 a.u. for ISA shift parameter^{11,24}, and 0.3 a.u. for imaginary shift parameter^{25,26}. However, our present study reports that the optimal value of each shift parameter is indeed larger than the customary values. On the other hand, employing too small values of the shift parameter probably raise the risk of large error in the MRPT calculations.

Chapter 5

Conclusions

The shift techniques applicable to the MRPT methods have been critically evaluated by a statistical approach. The spectroscopic constants of 65 studied states were investigated and compared with the experiment. We therefore propose that the optimal value of the shift parameter is 1.0 a.u. for the real shift technique, 0.3 a.u. for the ISA shift technique, and 0.6 a.u. for the imaginary shift technique in present Thesis. The research results indicate that the employment of the optimal value can diminish the systematic error of the second-order perturbation theory as well as eliminate intruder states. In this study, the idea of transferring the CASSCF wavefunctions between different programs was successfully implemented. The approach could help us to study the different multireference methods in a uniform way. We could further investigate the behavior of shift techniques applicable to MRPT methods through comparing with other multireference methods such as MRCI, NEVPT2 and so on. Because of the fast development of computer resources, MRPT methods can overcome higher computational demands, which may help to expand their applications field in the future. The shift techniques certainly play an important role for the multireference perturbation theory in this context.

Chapter 6

Auxiliary materials

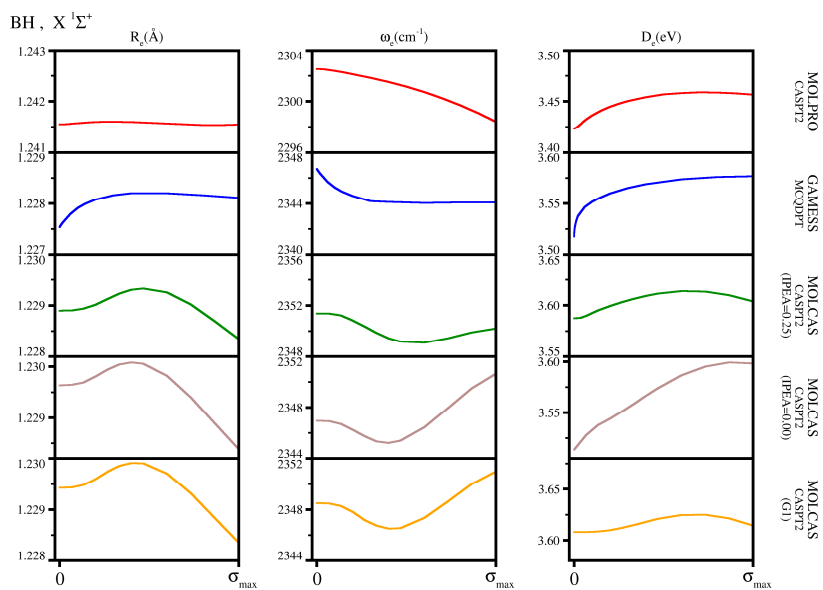


Figure 6.1 Spectroscopic constants for the $X^1\Sigma^+$ state of BH obtained using different methods with various values of the shift parameter σ .

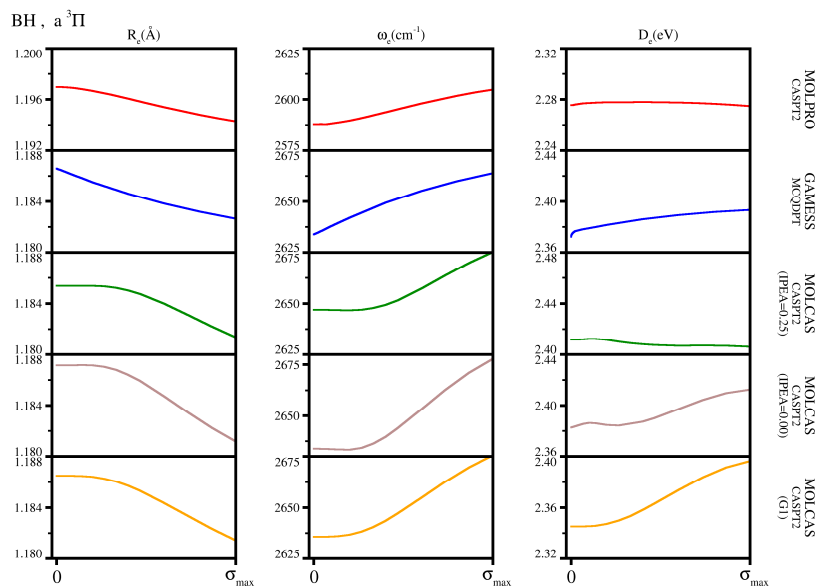


Figure 6.2 Spectroscopic constants for the $a^3\Pi$ state of BH obtained using different methods with various values of the shift parameter σ .

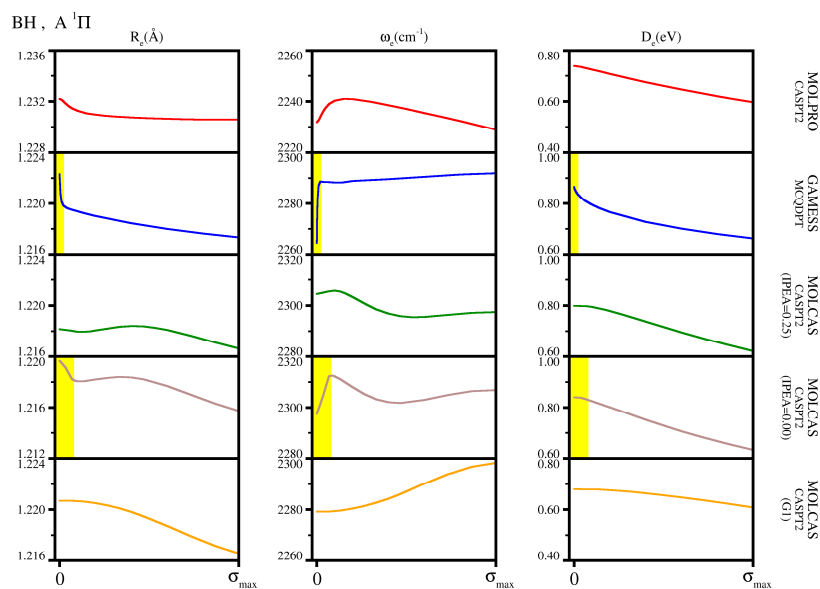


Figure 6.3 Spectroscopic constants for the $A^1\Pi$ state of BH obtained using different methods with various values of the shift parameter σ .

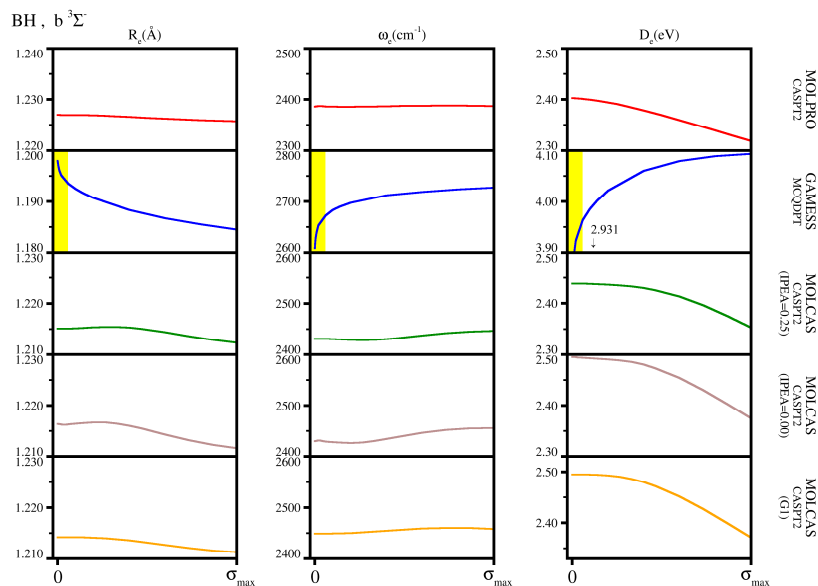


Figure 6.4 Spectroscopic constants for the $b^3\Sigma^-$ state of BH obtained using different methods with various values of the shift parameter σ .

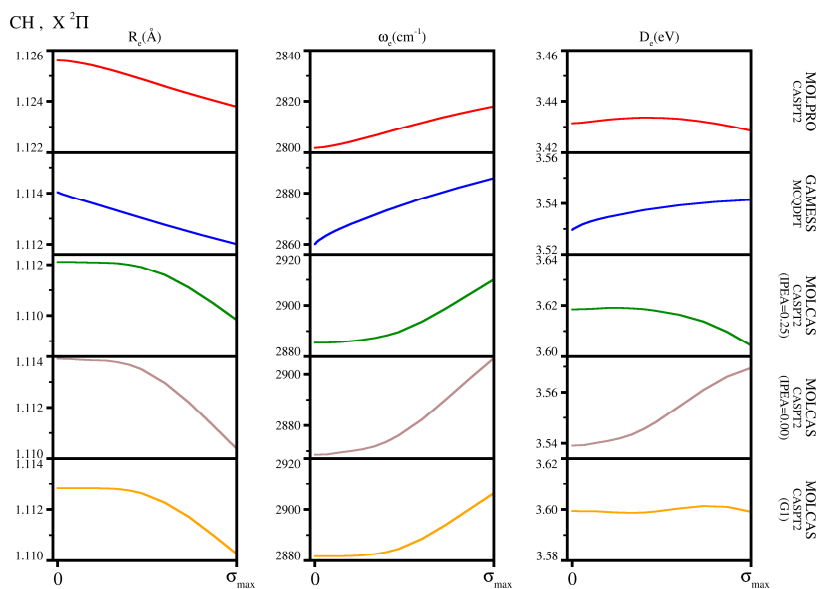


Figure 6.5 Spectroscopic constants for the $X^2\Pi$ state of CH obtained using different methods with various values of the shift parameter σ .

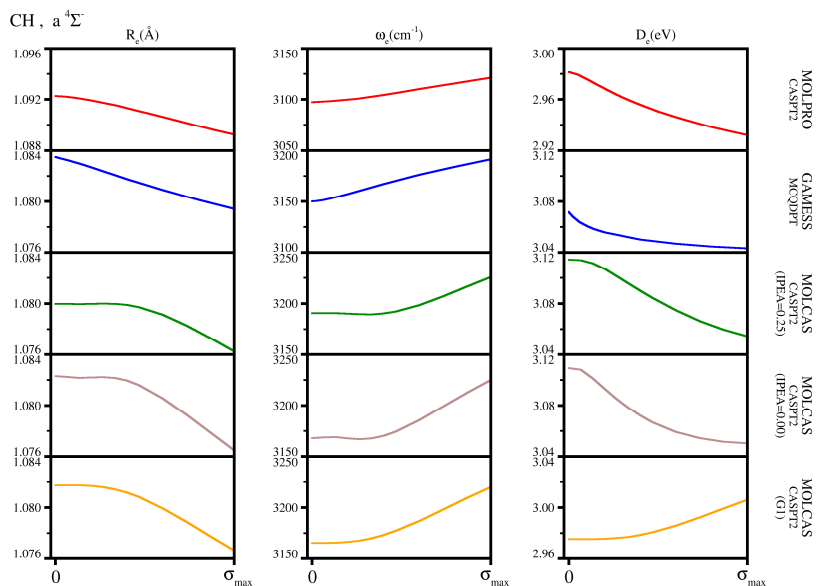


Figure 6.6 Spectroscopic constants for the $a^4\Sigma^-$ state of CH obtained using different methods with various values of the shift parameter σ .

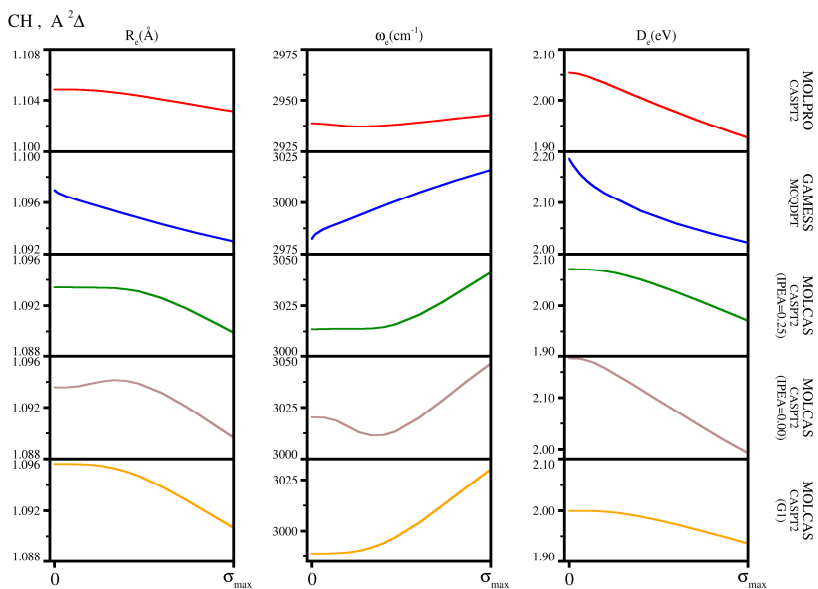


Figure 6.7 Spectroscopic constants for the $A^2\Delta$ state of CH obtained using different methods with various values of the shift parameter σ .

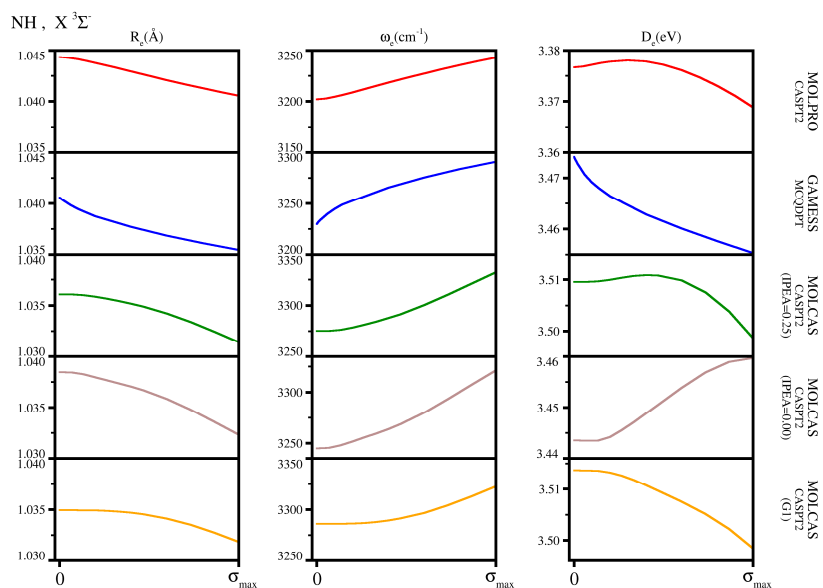


Figure 6.8 Spectroscopic constants for the $X^3\Sigma^-$ state of NH obtained using different methods with various values of the shift parameter σ .

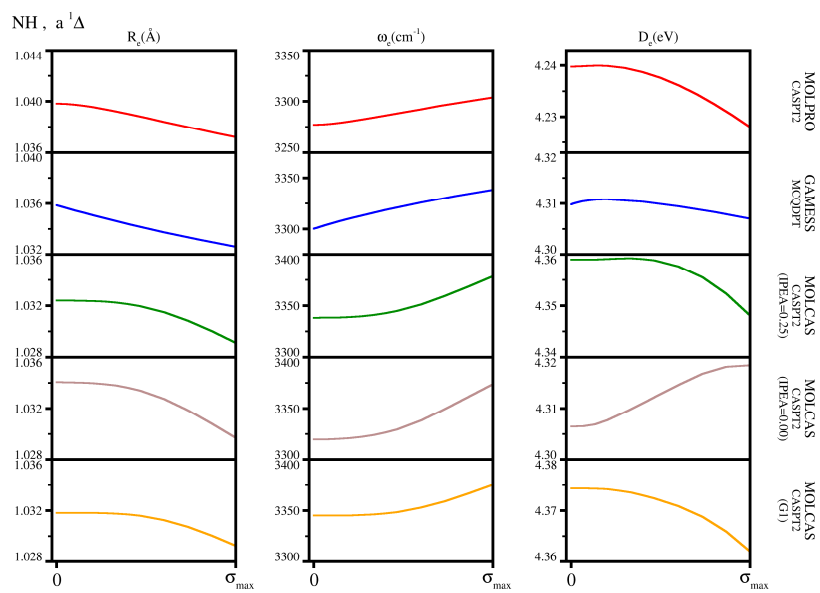


Figure 6.9 Spectroscopic constants for the $a^1\Delta$ state of NH obtained using different methods with various values of the shift parameter σ .

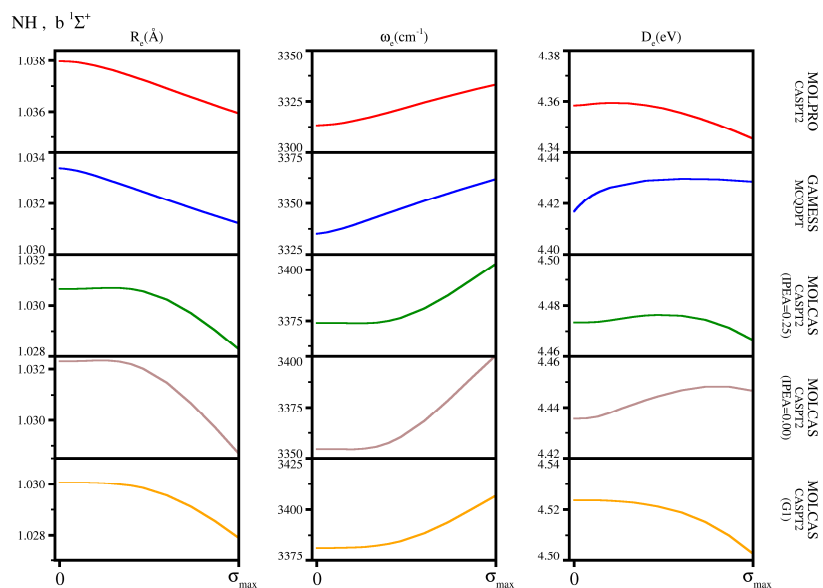


Figure 6.10 Spectroscopic constants for the $b^1\Sigma^+$ state of NH obtained using different methods with various values of the shift parameter σ .

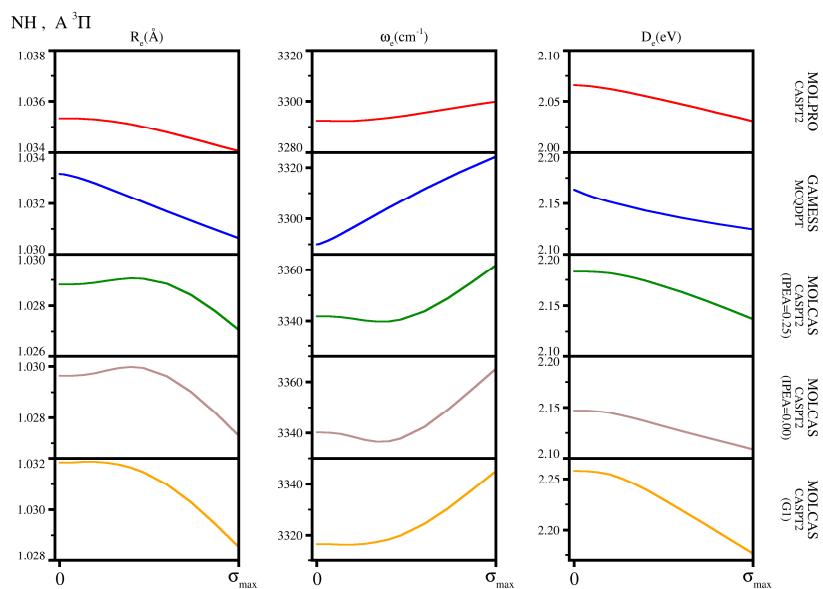


Figure 6.11 Spectroscopic constants for the $A^3\Pi$ state of NH obtained using different methods with various values of the shift parameter σ .

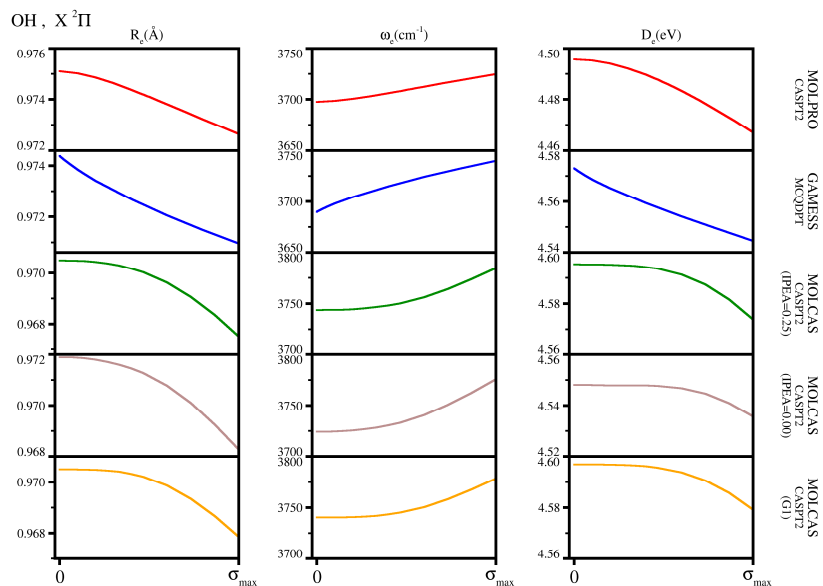


Figure 6.12 Spectroscopic constants for the $X^2\Pi$ state of OH obtained using different methods with various values of the shift parameter σ .

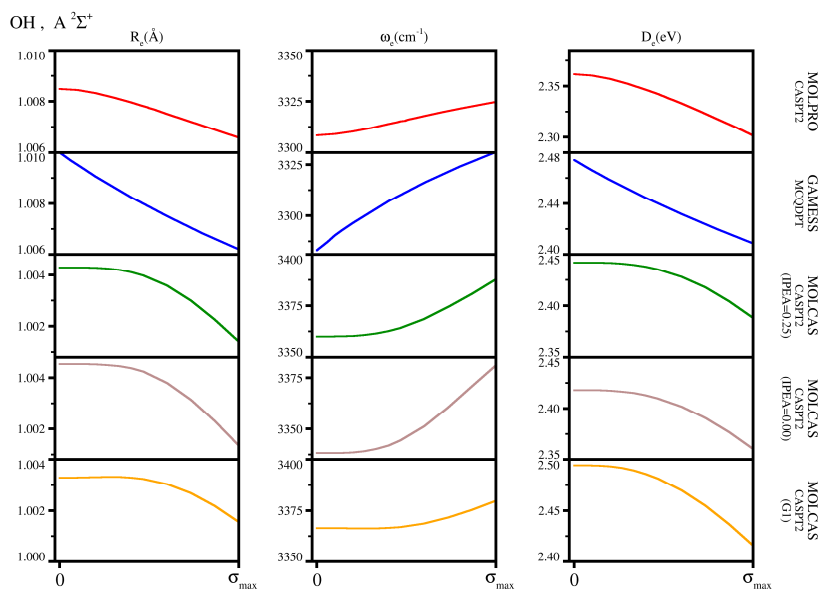


Figure 6.13 Spectroscopic constants for the $A^2\Sigma^+$ state of OH obtained using different methods with various values of the shift parameter σ .

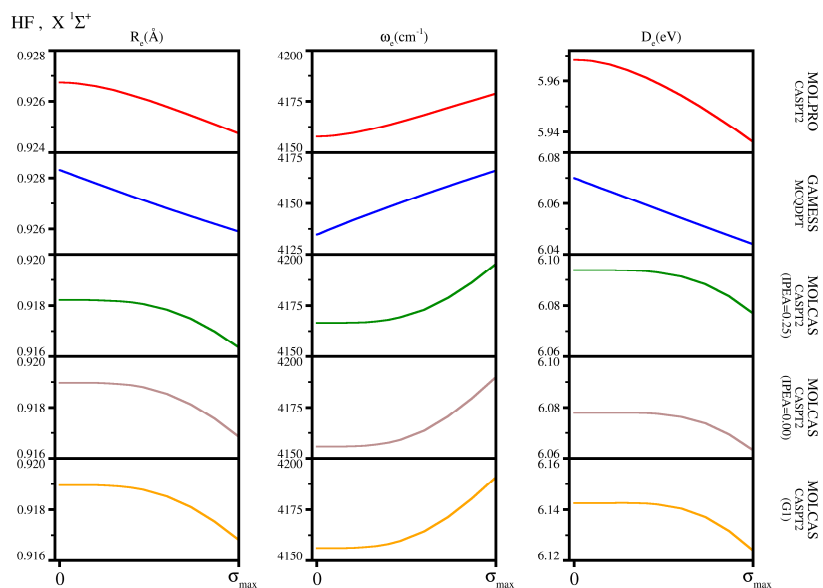


Figure 6.14 Spectroscopic constants for the $X^1\Sigma^+$ state of HF obtained using different methods with various values of the shift parameter σ .

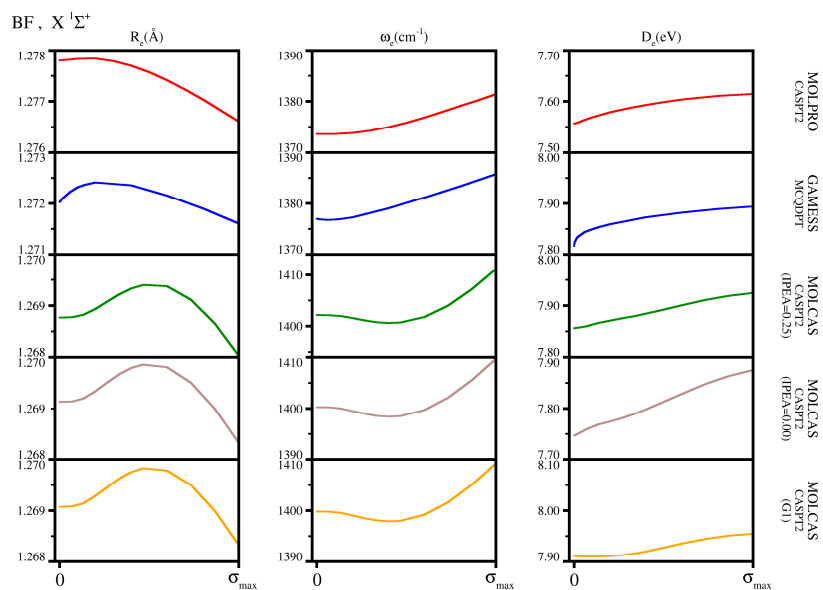


Figure 6.15 Spectroscopic constants for the $X^1\Sigma^+$ state of BF obtained using different methods with various values of the shift parameter σ .

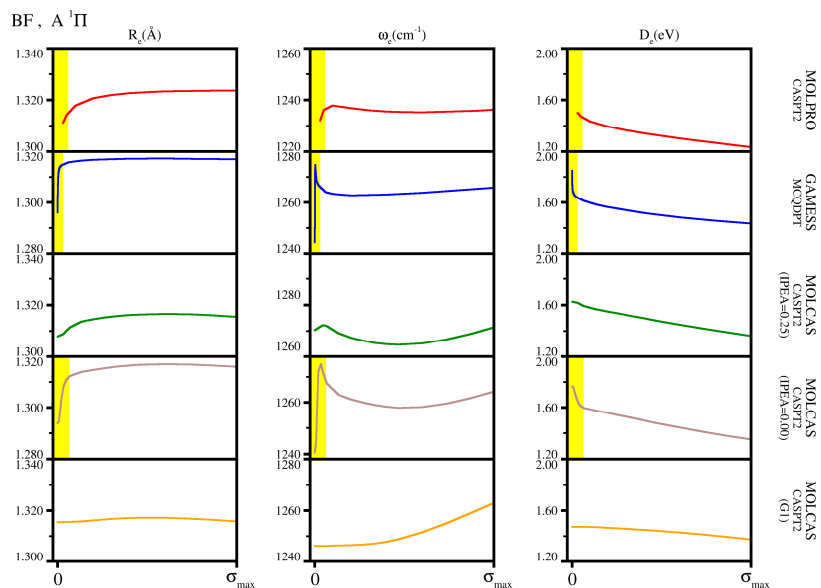


Figure 6.16 Spectroscopic constants for the $A^1\Pi$ state of BF obtained using different methods with various values of the shift parameter σ .

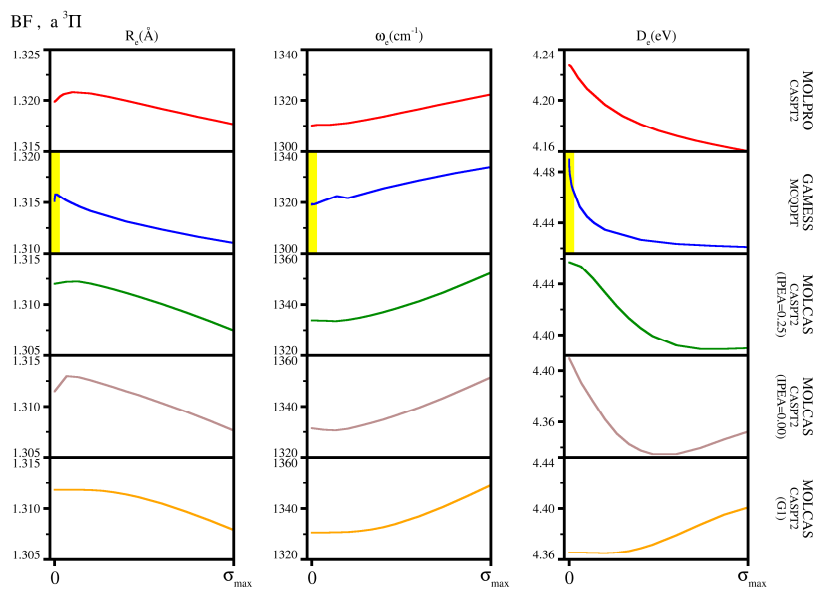


Figure 6.17 Spectroscopic constants for the $a^3\Pi$ state of BF obtained using different methods with various values of the shift parameter σ .

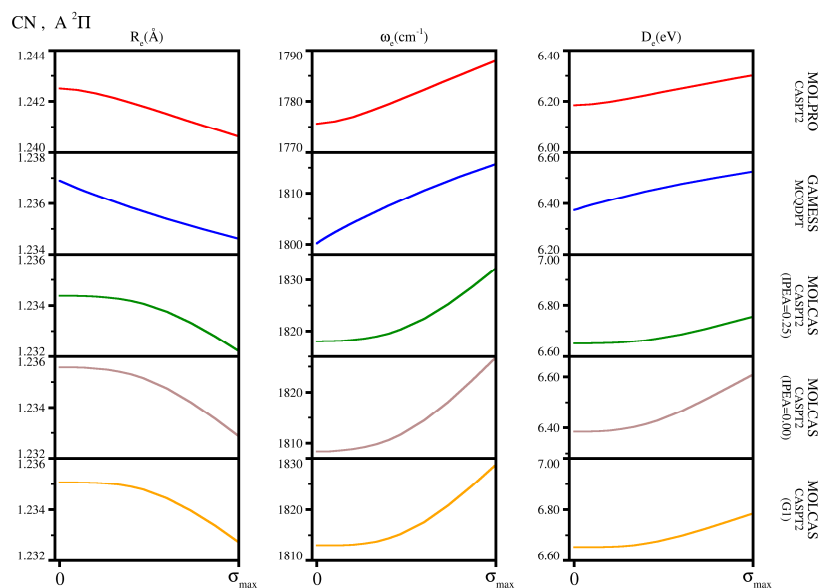


Figure 6.18 Spectroscopic constants for the $A^2\Pi$ state of CN obtained using different methods with various values of the shift parameter σ .

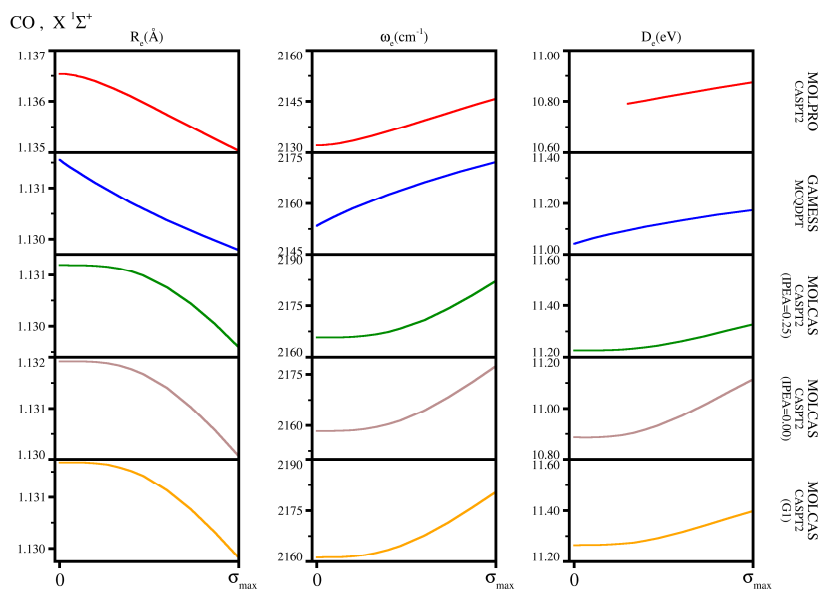


Figure 6.19 Spectroscopic constants for the $X^1\Sigma^+$ state of CO obtained using different methods with various values of the shift parameter σ .

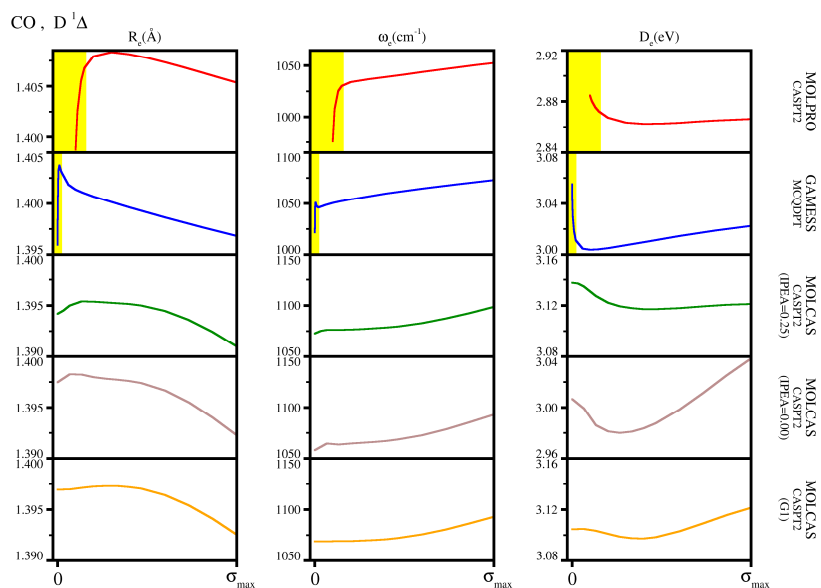


Figure 6.20 Spectroscopic constants for the $D^1\Delta$ state of CO obtained using different methods with various values of the shift parameter σ .

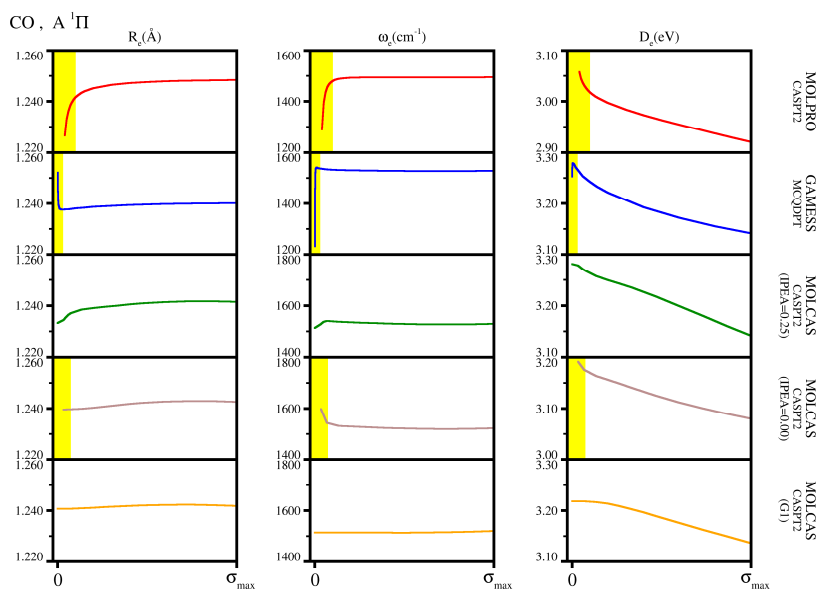


Figure 6.21 Spectroscopic constants for the $A^1\Pi$ state of CO obtained using different methods with various values of the shift parameter σ .

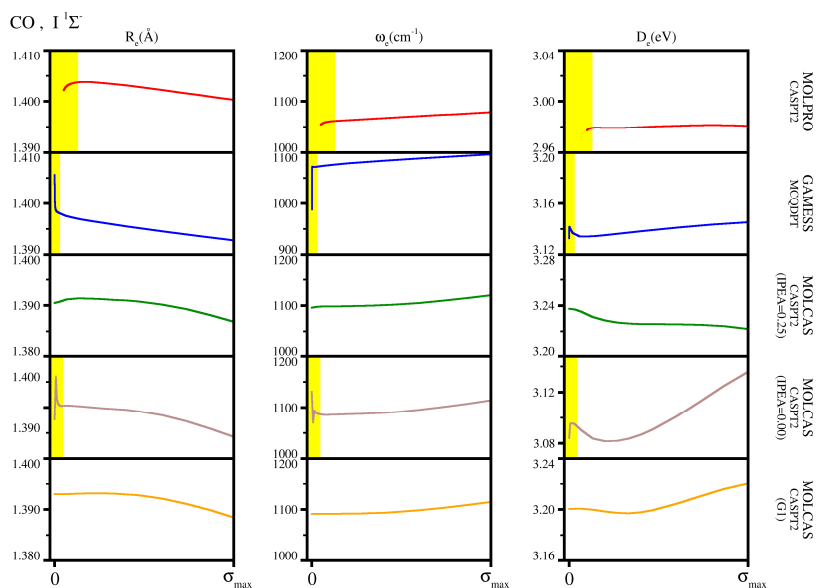


Figure 6.22 Spectroscopic constants for the $I^1\Sigma^-$ state of CO obtained using different methods with various values of the shift parameter σ .

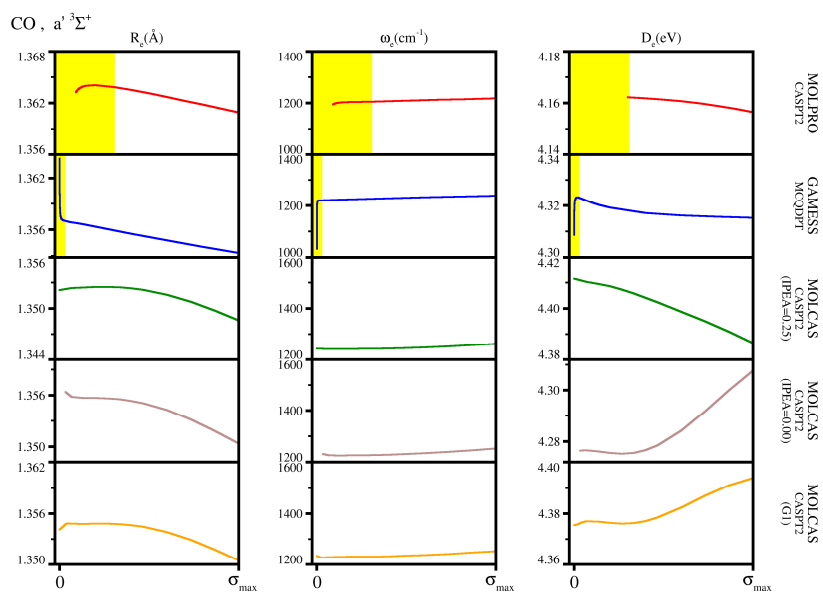


Figure 6.23 Spectroscopic constants for the $a^1^3\Sigma^+$ state of CO obtained using different methods with various values of the shift parameter σ .

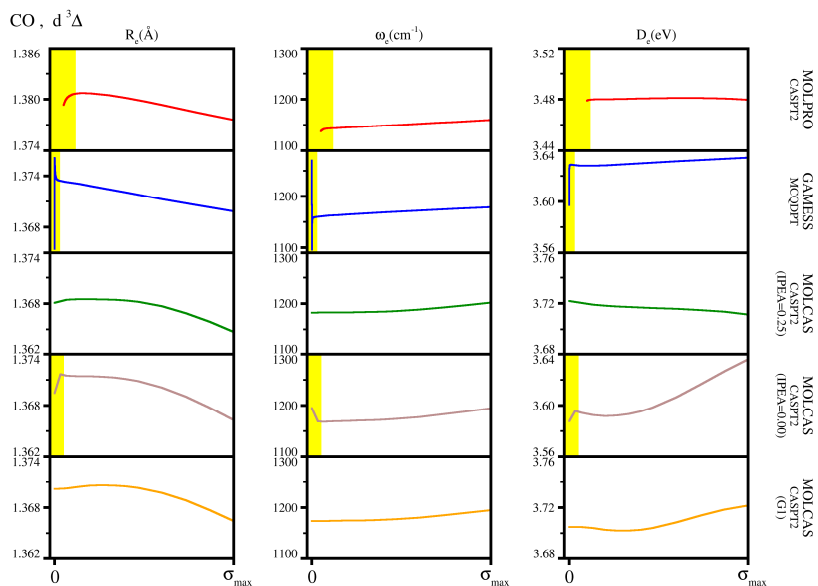


Figure 6.24 Spectroscopic constants for the $d^3\Delta$ state of CO obtained using different methods with various values of the shift parameter σ .

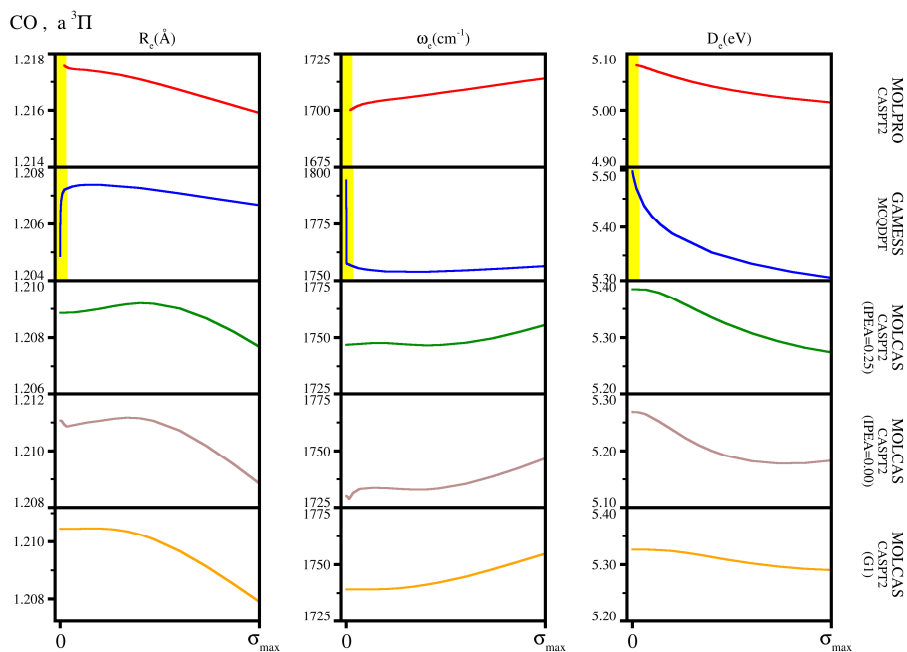


Figure 6.25 Spectroscopic constants for the $a^3\Pi$ state of CO obtained using different methods with various values of the shift parameter σ .

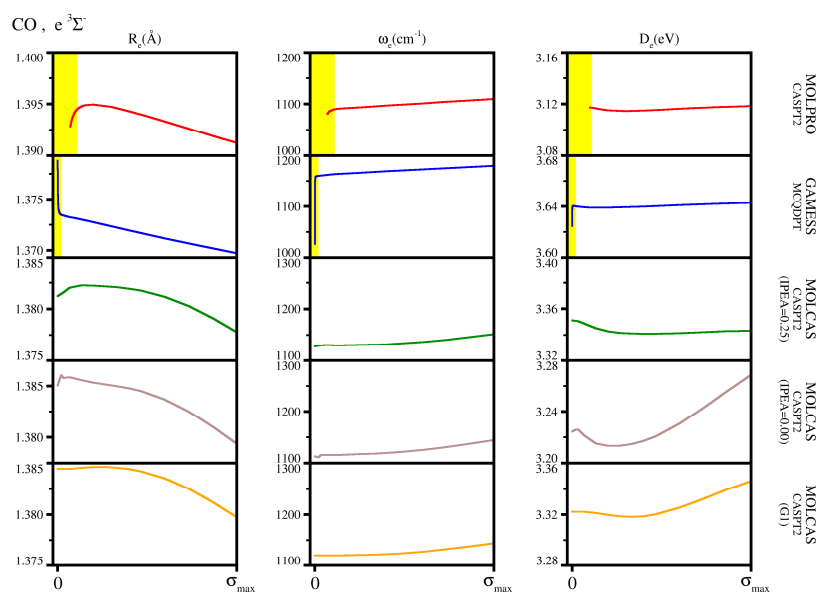


Figure 6.26 Spectroscopic constants for the $e^3\Sigma^-$ state of CO obtained using different methods with various values of the shift parameter σ .

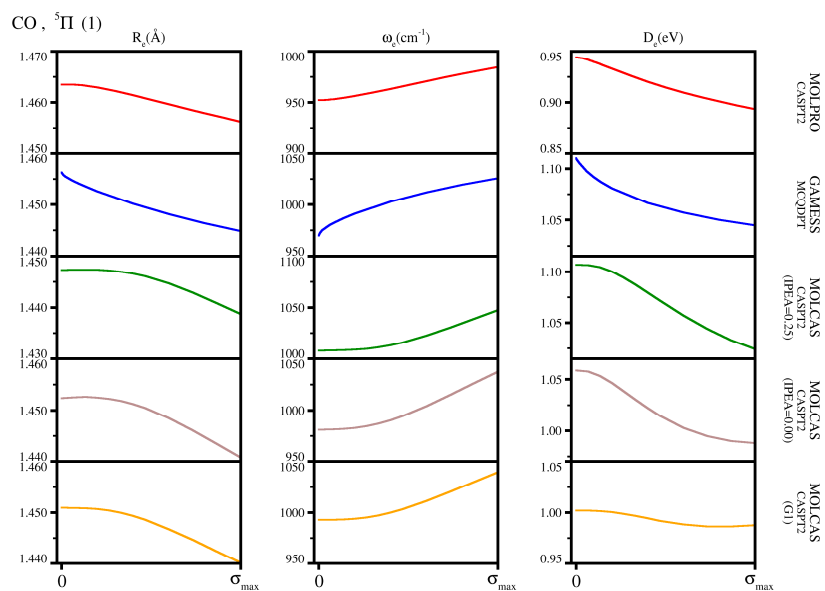


Figure 6.27 Spectroscopic constants for the $^5\Pi (1)$ state of CO obtained using different methods with various values of the shift parameter σ .

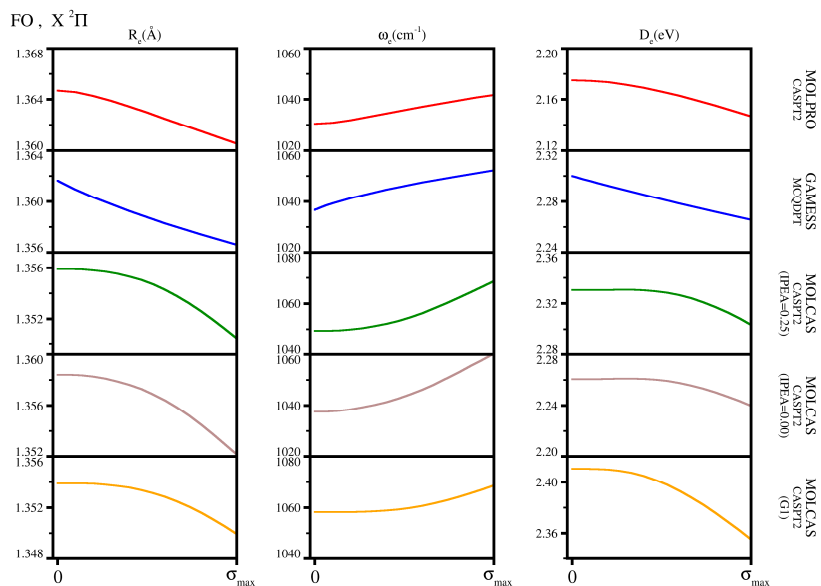


Figure 6.28 Spectroscopic constants for the $X^2\Pi$ state of FO obtained using different methods with various values of the shift parameter σ .

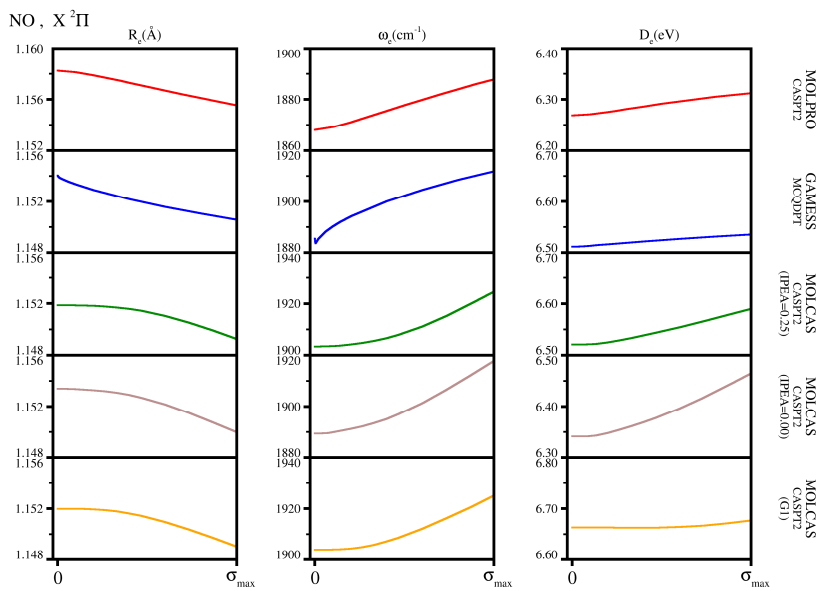


Figure 6.29 Spectroscopic constants for the $X^2\Pi$ state of NO obtained using different methods with various values of the shift parameter σ .

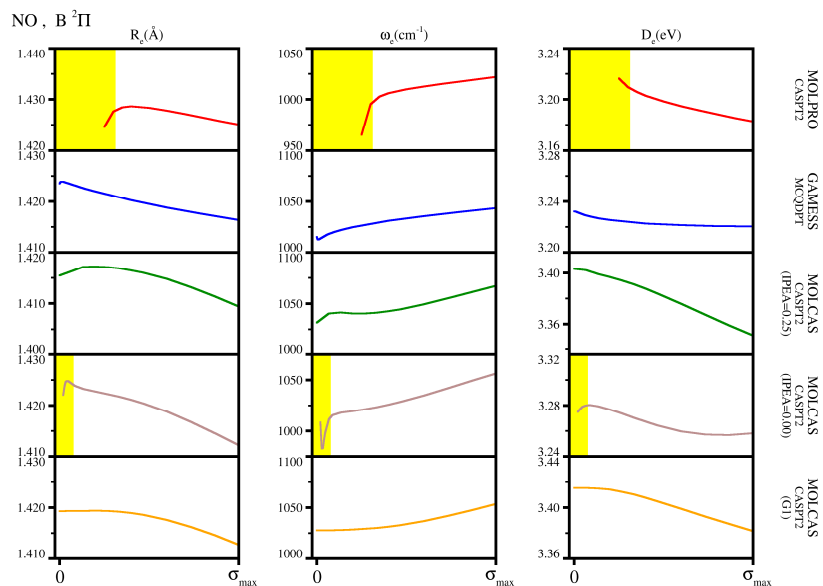


Figure 6.30 Spectroscopic constants for the $B^2\Pi$ state of NO obtained using different methods with various values of the shift parameter σ .

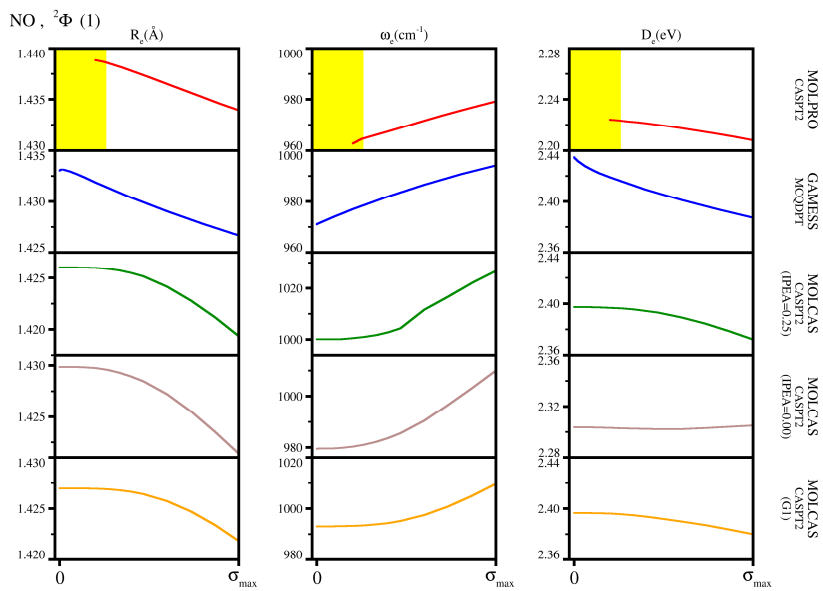


Figure 6.31 Spectroscopic constants for the $^2\Phi(1)$ state of NO obtained using different methods with various values of the shift parameter σ .

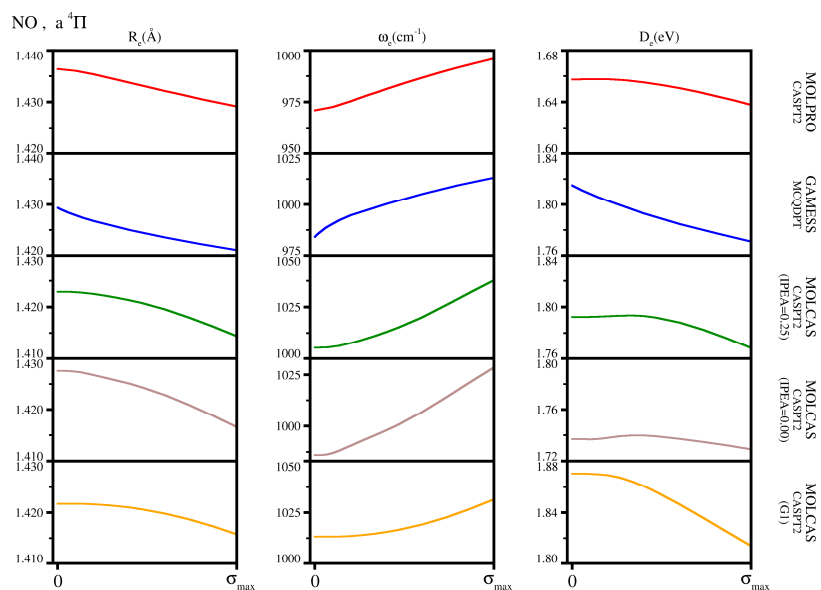


Figure 6.32 Spectroscopic constants for the $a^4\Pi$ state of NO obtained using different methods with various values of the shift parameter σ .

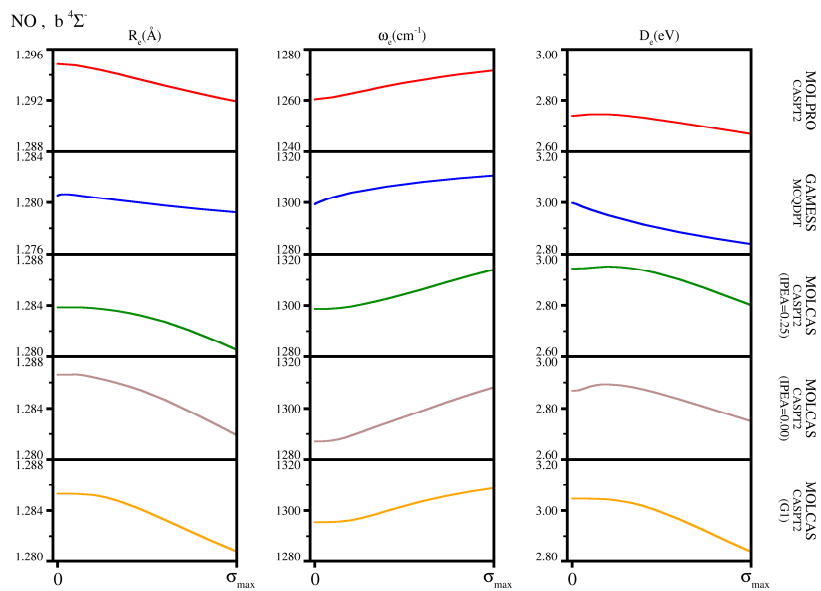


Figure 6.33 Spectroscopic constants for the $b^4\Sigma^-$ state of NO obtained using different methods with various values of the shift parameter σ .

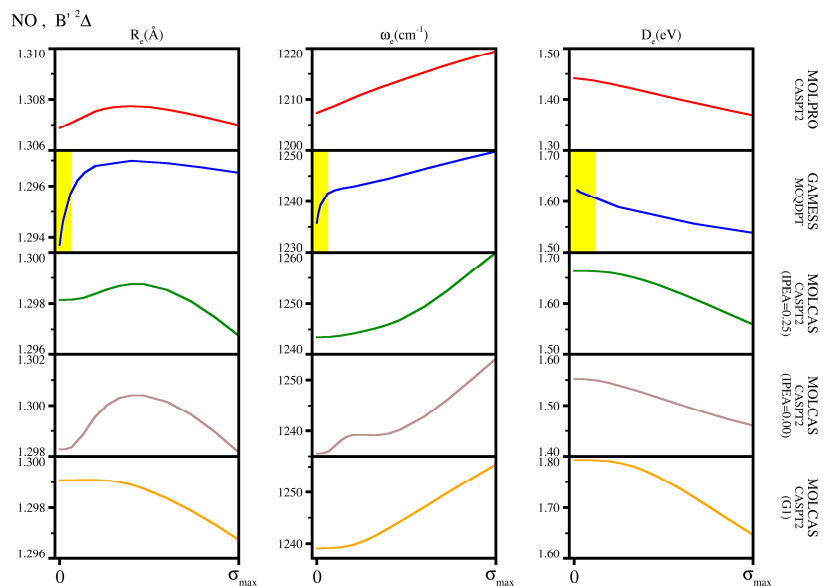


Figure 6.34 Spectroscopic constants for the $B' \ ^2\Delta$ state of NO obtained using different methods with various values of the shift parameter σ .

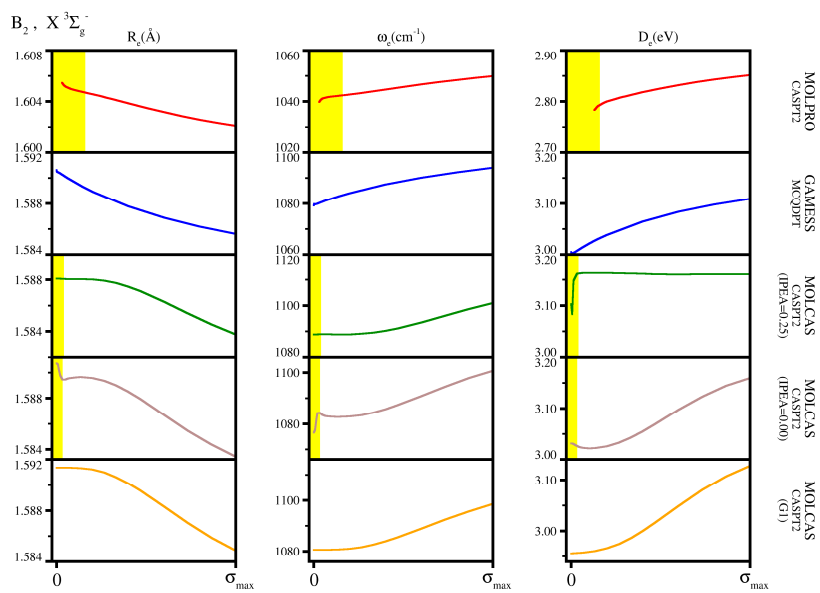


Figure 6.35 Spectroscopic constants for the $X \ ^3\Sigma_g^-$ state of B_2 obtained using different methods with various values of the shift parameter σ .

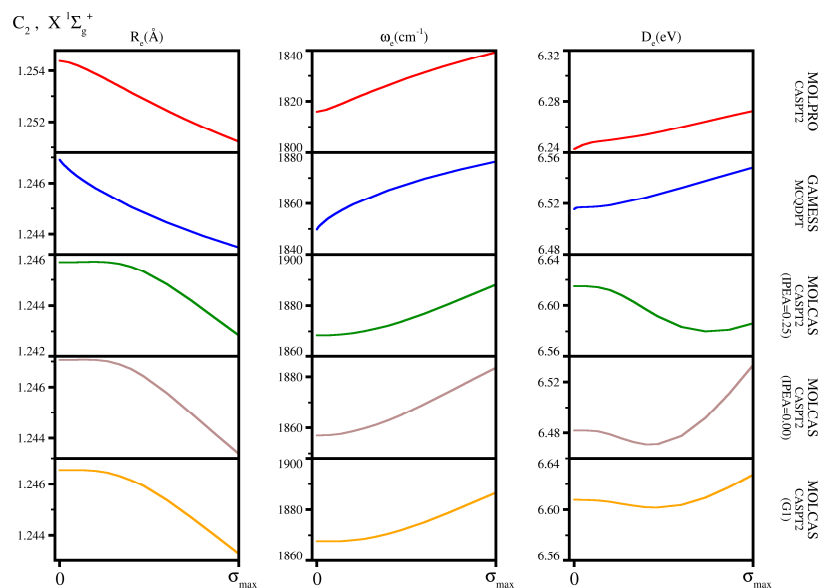


Figure 6.36 Spectroscopic constants for the $X \ ^1\Sigma_g^+$ state of C_2 obtained using different methods with various values of the shift parameter σ .

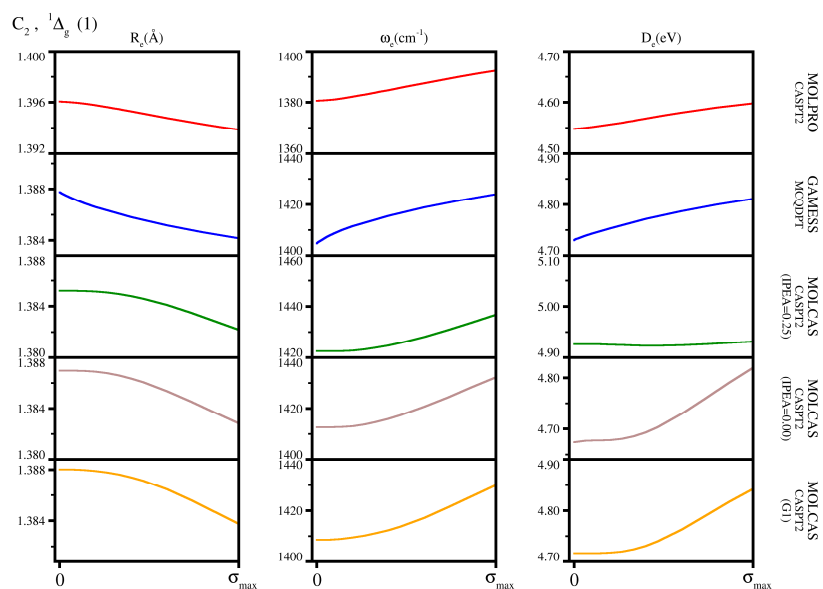


Figure 6.37 Spectroscopic constants for the $^1\Delta_g (1)$ state of C_2 obtained using different methods with various values of the shift parameter σ .

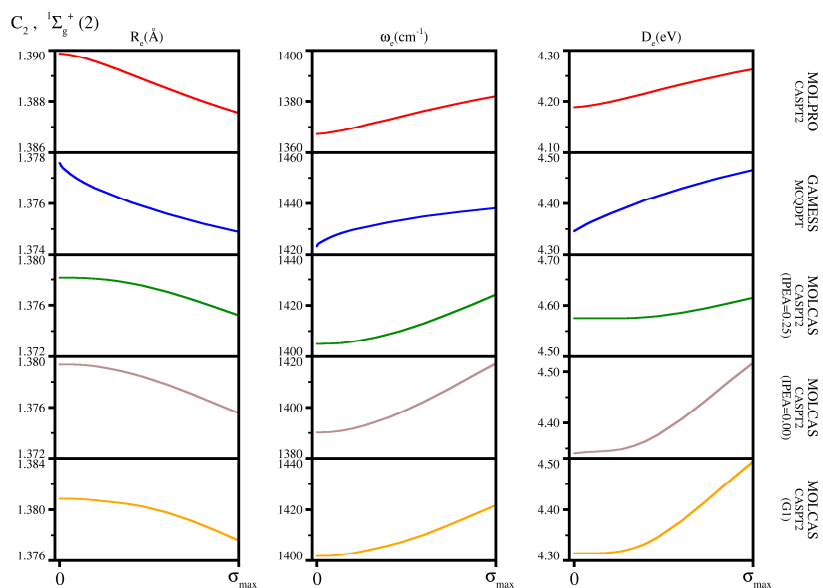


Figure 6.38 Spectroscopic constants for the $1\Sigma_g^+(2)$ state of C_2 obtained using different methods with various values of the shift parameter σ .

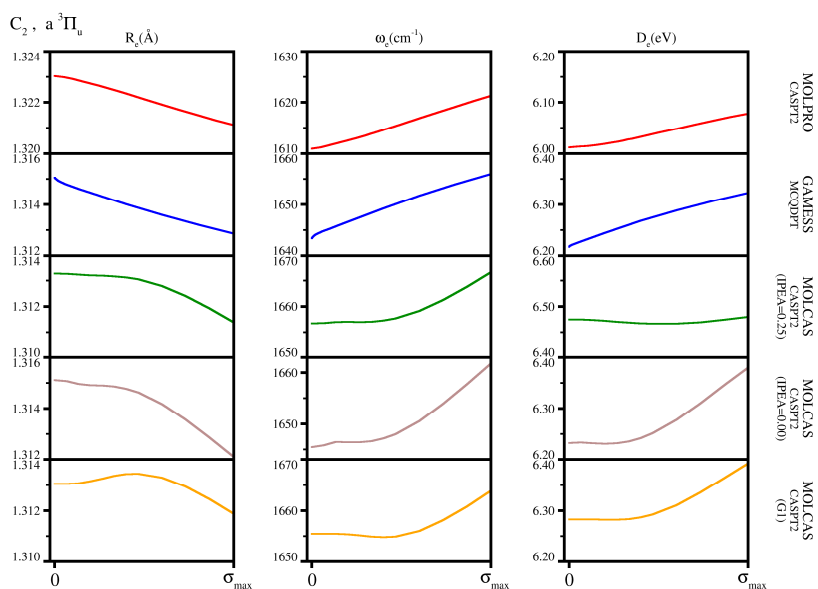


Figure 6.39 Spectroscopic constants for the $a^3\Pi_u$ state of C_2 obtained using different methods with various values of the shift parameter σ .

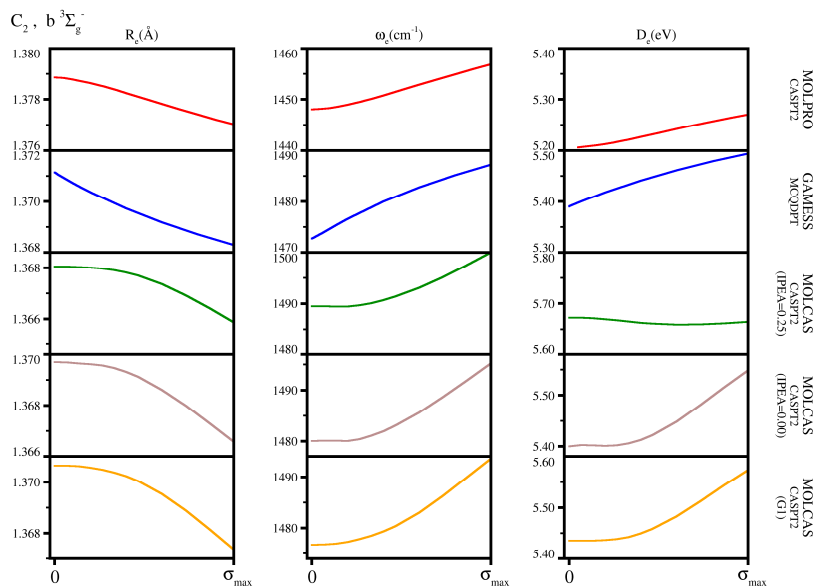


Figure 6.40 Spectroscopic constants for the $b\ ^3\Sigma_g^-$ state of C_2 obtained using different methods with various values of the shift parameter σ .

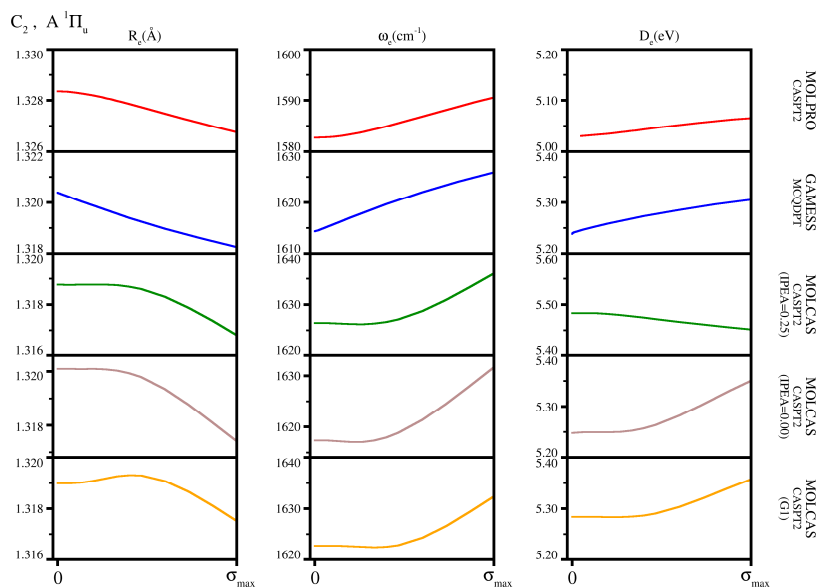


Figure 6.41 Spectroscopic constants for the $A\ ^1\Pi_u$ state of C_2 obtained using different methods with various values of the shift parameter σ .

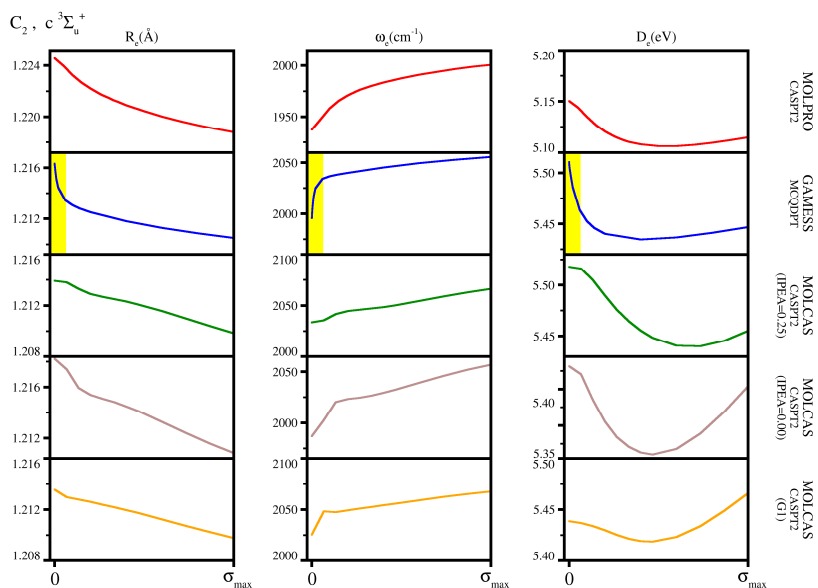


Figure 6.42 Spectroscopic constants for the $c^3\Sigma_u^+$ state of C_2 obtained using different methods with various values of the shift parameter σ .

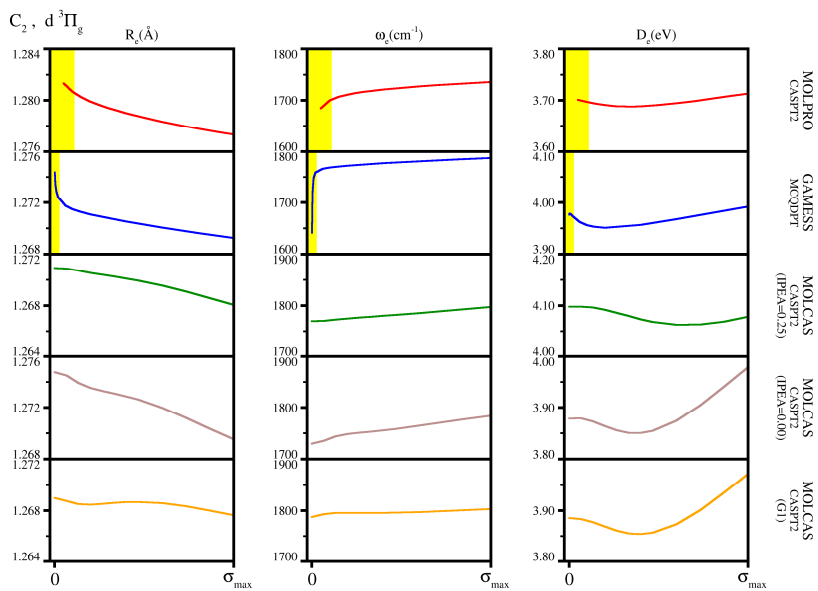


Figure 6.43 Spectroscopic constants for the $d^3\Pi_g$ state of C_2 obtained using different methods with various values of the shift parameter σ .

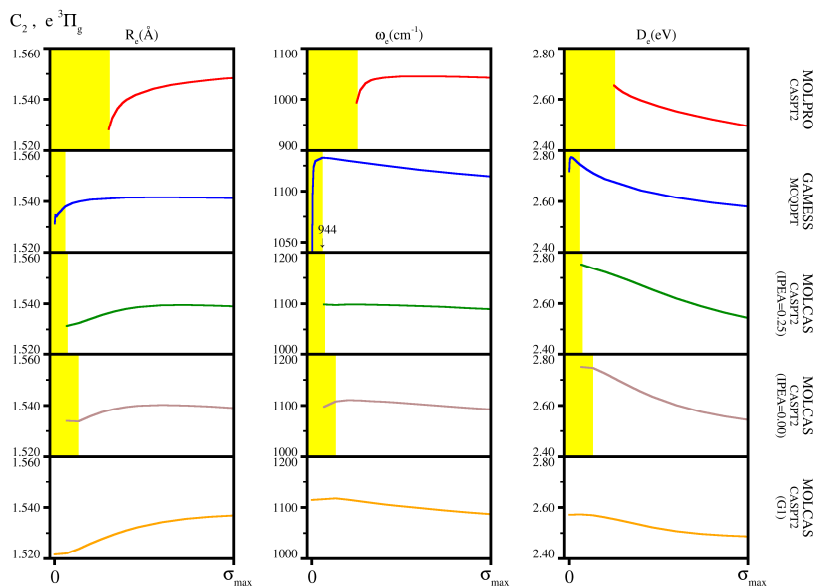


Figure 6.44 Spectroscopic constants for the $e^3\Pi_g$ state of C_2 obtained using different methods with various values of the shift parameter σ .

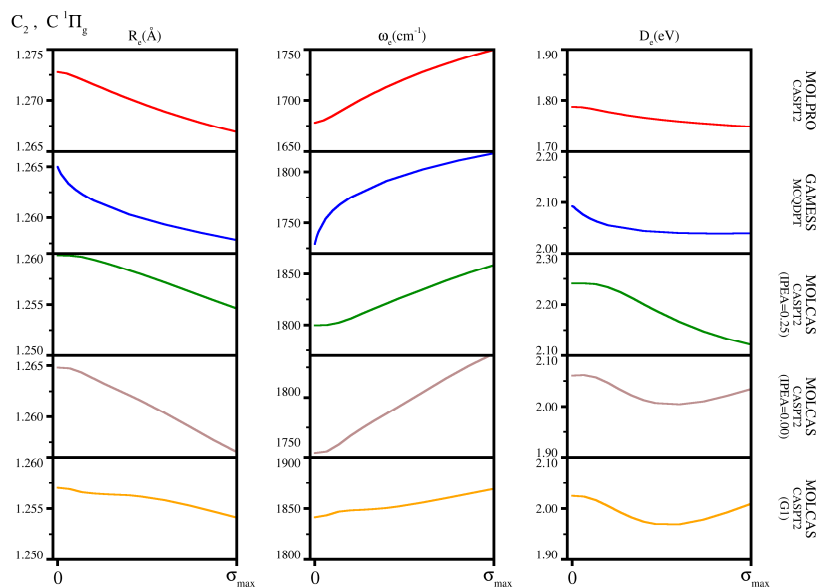


Figure 6.45 Spectroscopic constants for the $C^1\Pi_g$ state of C_2 obtained using different methods with various values of the shift parameter σ .

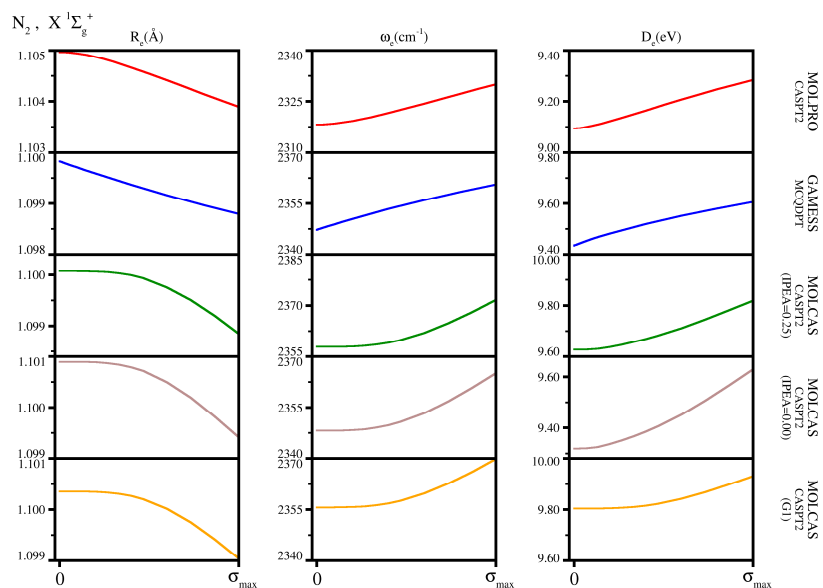


Figure 6.46 Spectroscopic constants for the $X^1\Sigma_g^+$ state of N_2 obtained using different methods with various values of the shift parameter σ .

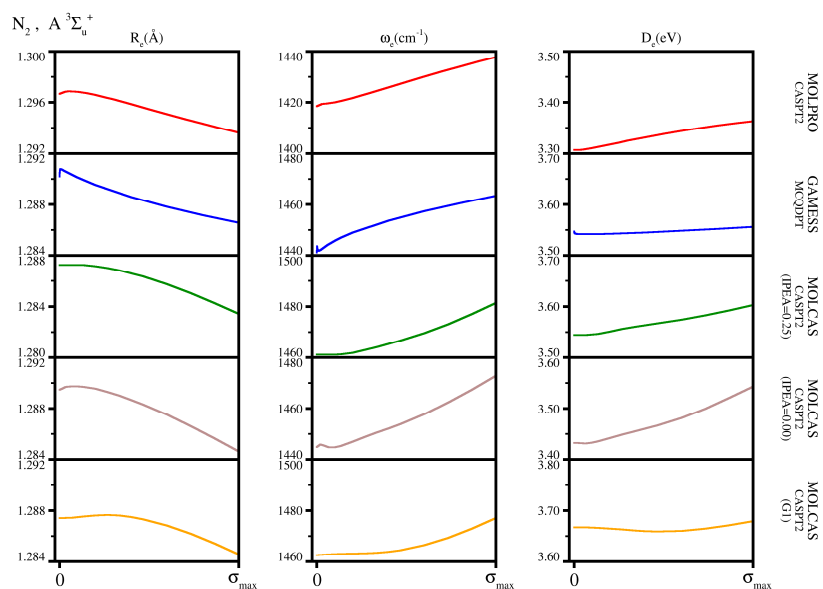


Figure 6.47 Spectroscopic constants for the $A^3\Sigma_u^+$ state of N_2 obtained using different methods with various values of the shift parameter σ .

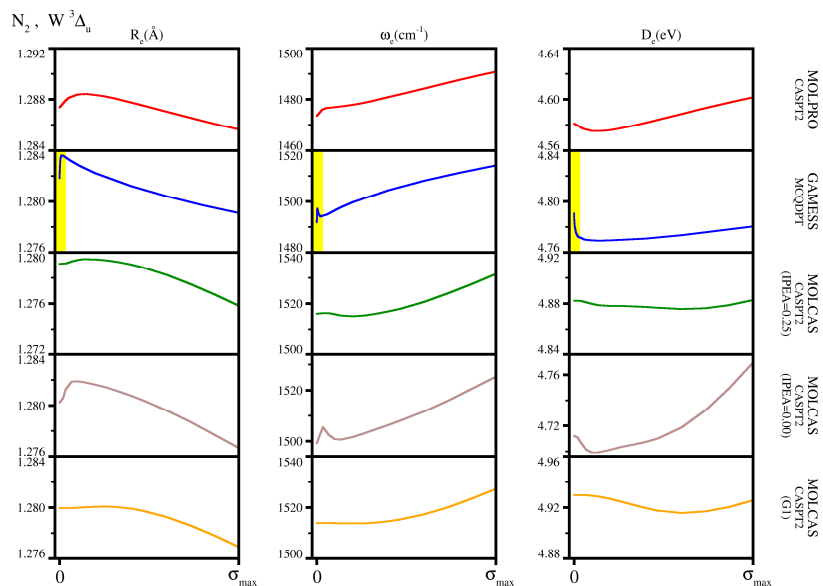


Figure 6.48 Spectroscopic constants for the $W^3\Delta_u$ state of N_2 obtained using different methods with various values of the shift parameter σ .

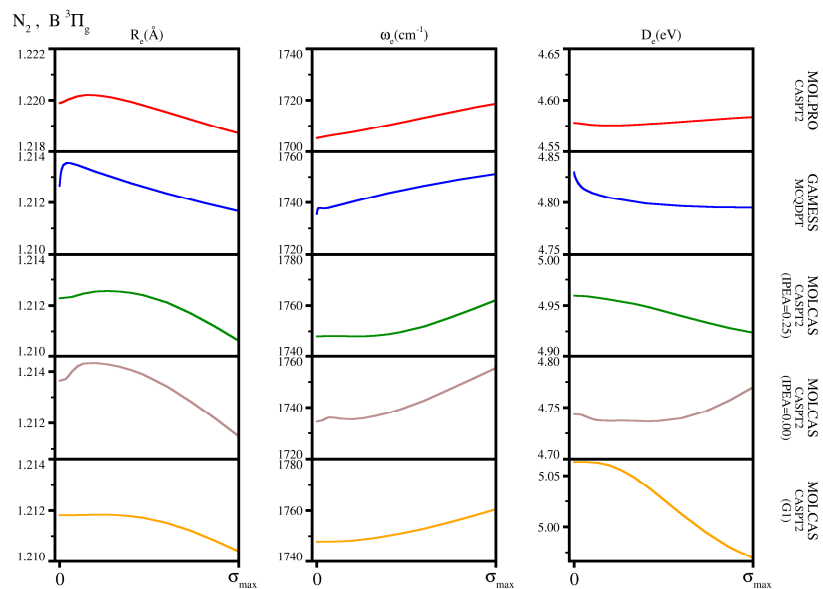


Figure 6.49 Spectroscopic constants for the $B^3\Pi_g$ state of N_2 obtained using different methods with various values of the shift parameter σ .

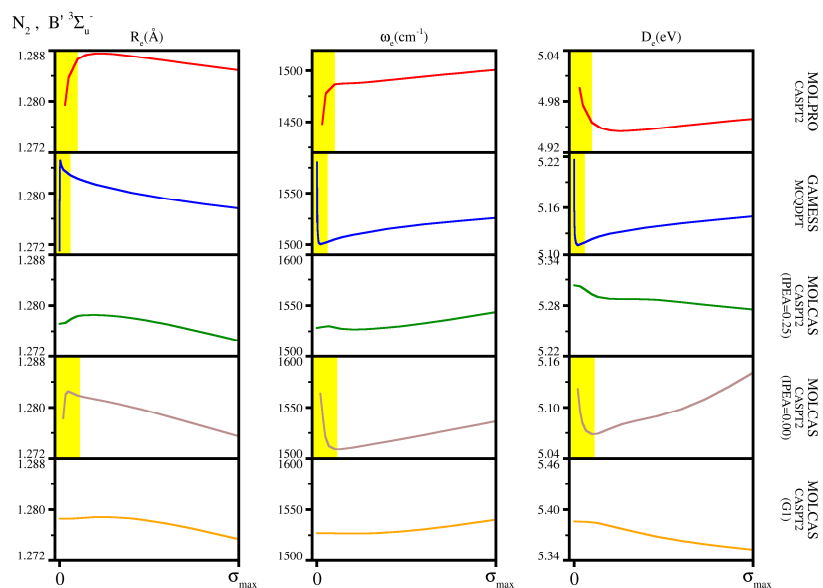


Figure 6.50 Spectroscopic constants for the $B' \ ^3\Sigma_u^-$ state of N_2 obtained using different methods with various values of the shift parameter σ .

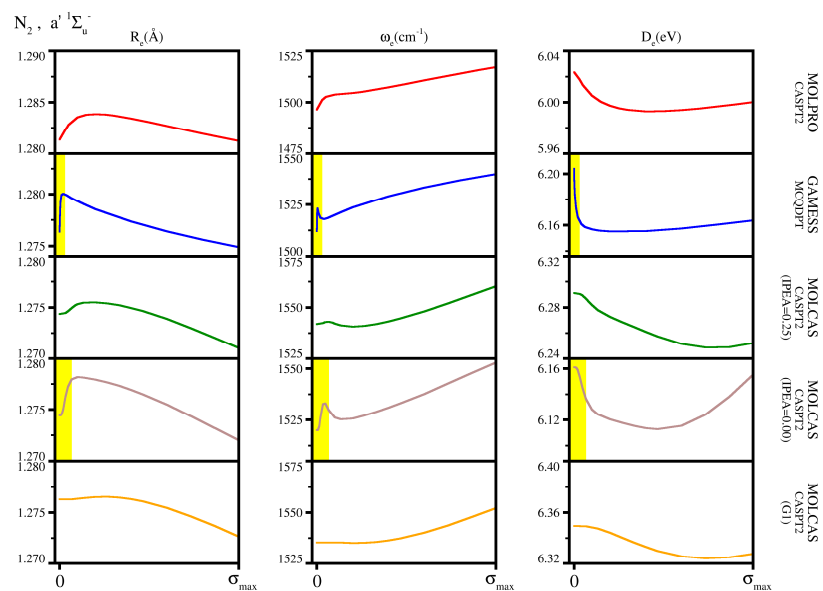


Figure 6.51 Spectroscopic constants for the $a' \ ^1\Sigma_u^-$ state of N_2 obtained using different methods with various values of the shift parameter σ .

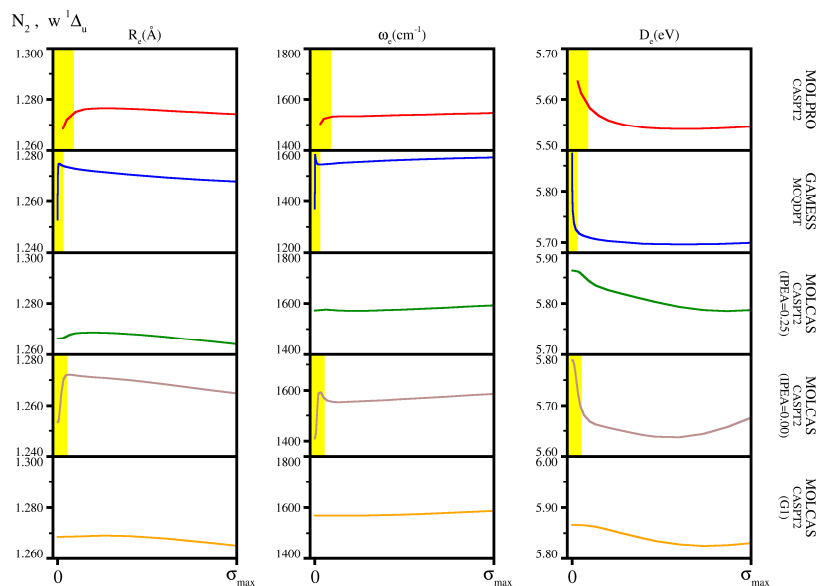


Figure 6.52 Spectroscopic constants for the $w\ ^1\Delta_u$ state of N_2 obtained using different methods with various values of the shift parameter σ .

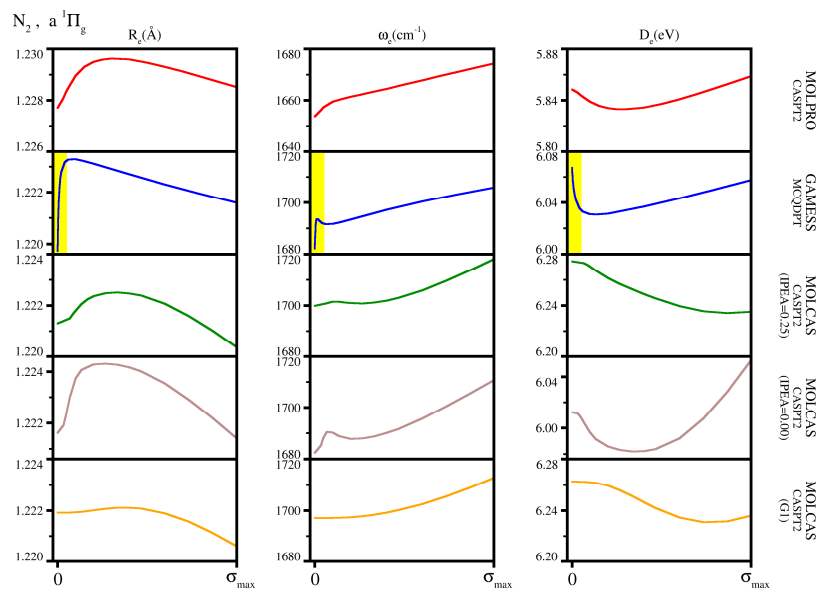


Figure 6.53 Spectroscopic constants for the $a\ ^1\Pi_g$ state of N_2 obtained using different methods with various values of the shift parameter σ .

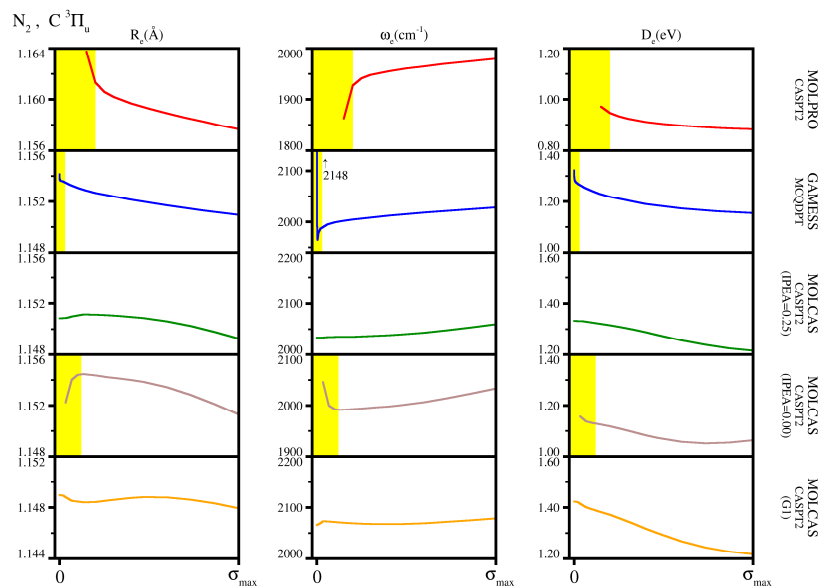


Figure 6.54 Spectroscopic constants for the $C^3\Pi_u$ state of N_2 obtained using different methods with various values of the shift parameter σ .

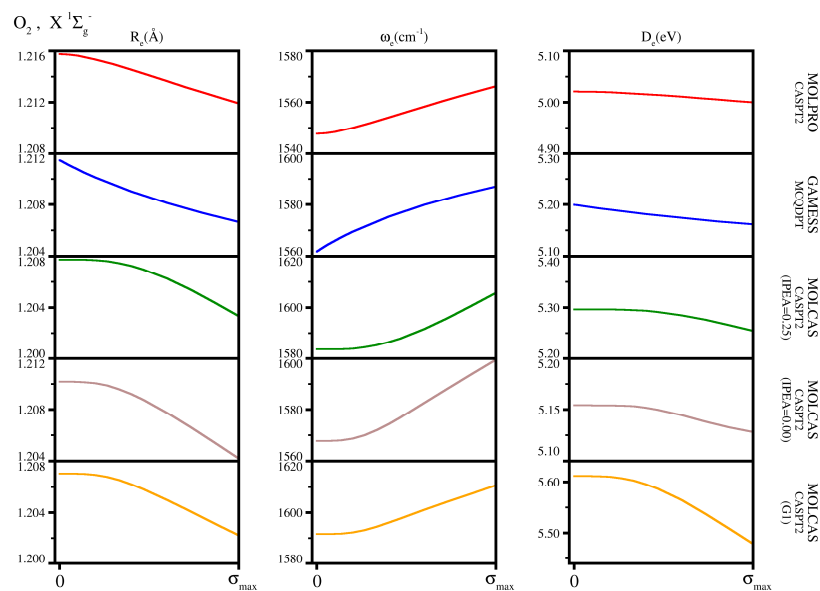


Figure 6.55 Spectroscopic constants for the $X^3\Sigma_g^-$ state of O_2 obtained using different methods with various values of the shift parameter σ .

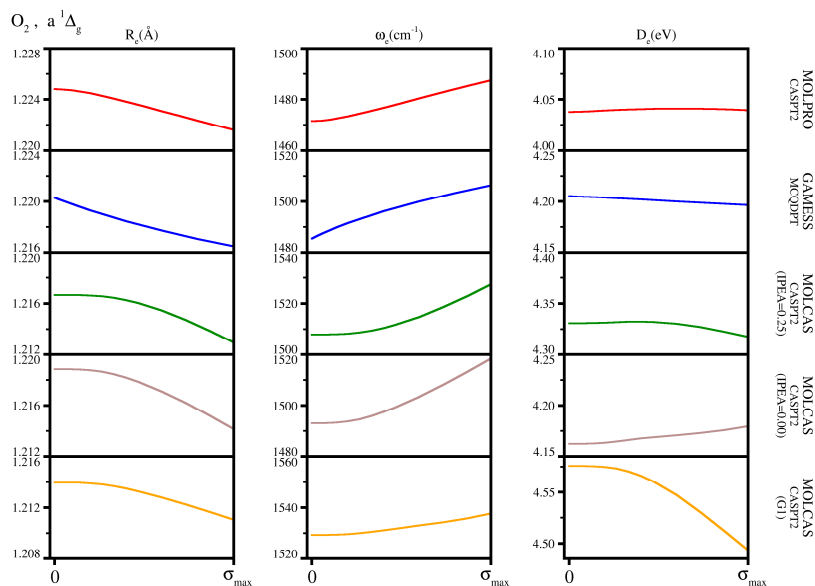


Figure 6.56 Spectroscopic constants for the $a^1\Delta_g$ obtained using different methods with various values of the shift parameter σ .

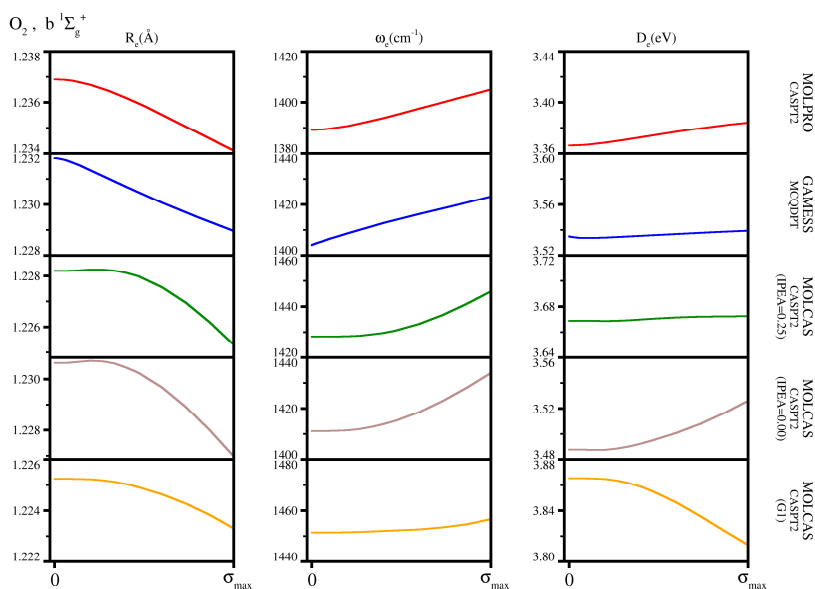


Figure 6.57 Spectroscopic constants for the $b^1\Sigma_g^+$ state of O_2 obtained using different methods with various values of the shift parameter σ .

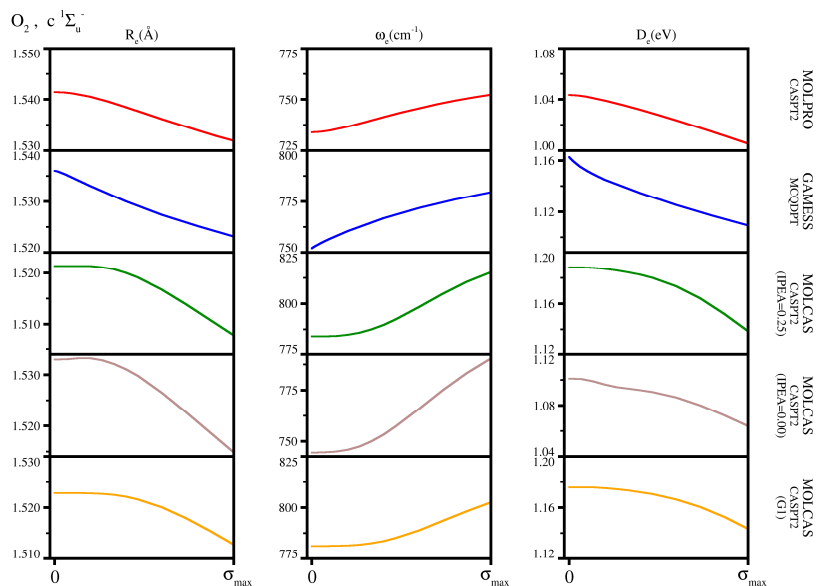


Figure 6.58 Spectroscopic constants for the $c^1\Sigma_u^-$ state of O_2 obtained using different methods with various values of the shift parameter σ .

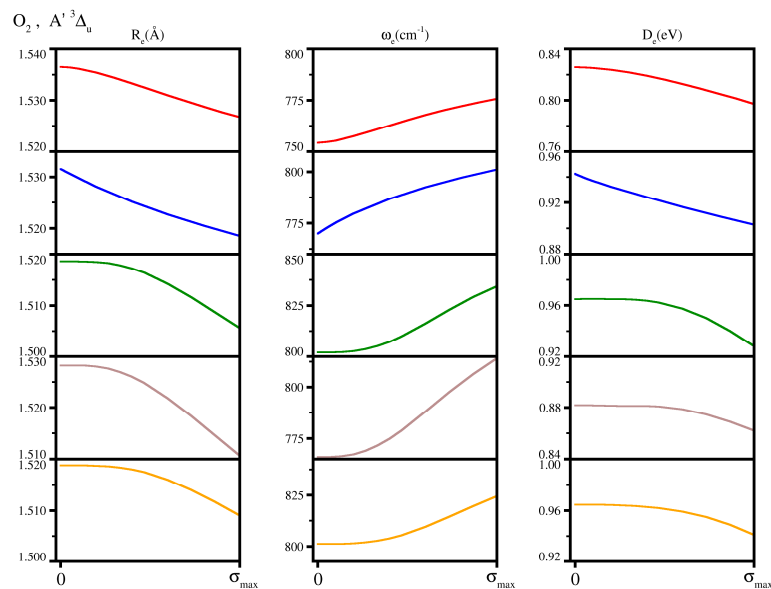


Figure 6.59 Spectroscopic constants for the $A'^3\Delta_u$ state of O_2 obtained using different methods with various values of the shift parameter σ .

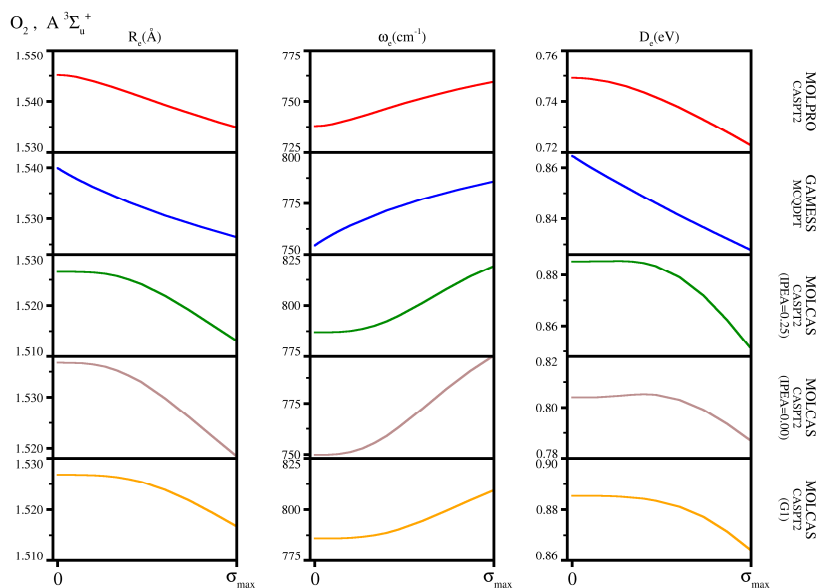


Figure 6.60 Spectroscopic constants for the $A \ ^3\Sigma_u^+$ state of O_2 obtained using different methods with various values of the shift parameter σ .

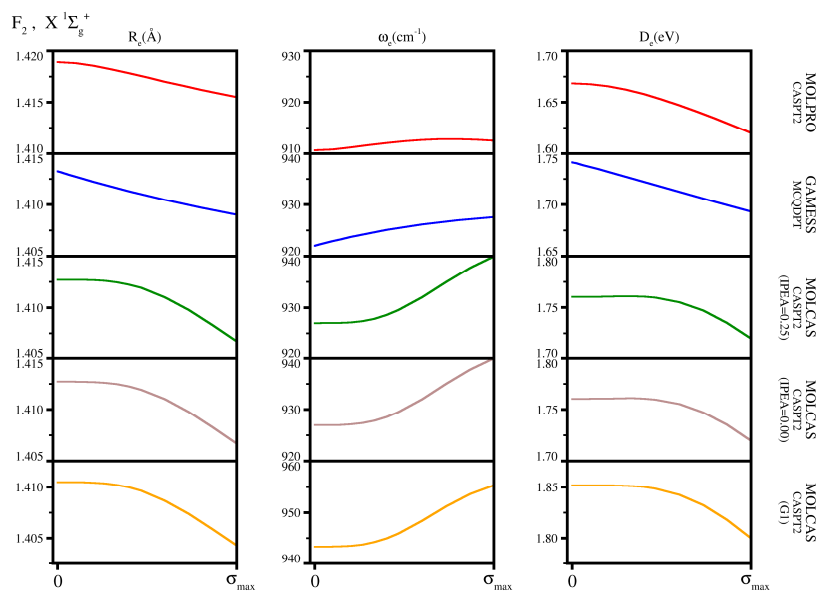


Figure 6.61 Spectroscopic constants for the $X \ ^1\Sigma_g^+$ state of F_2 obtained using different methods with various values of the shift parameter σ .

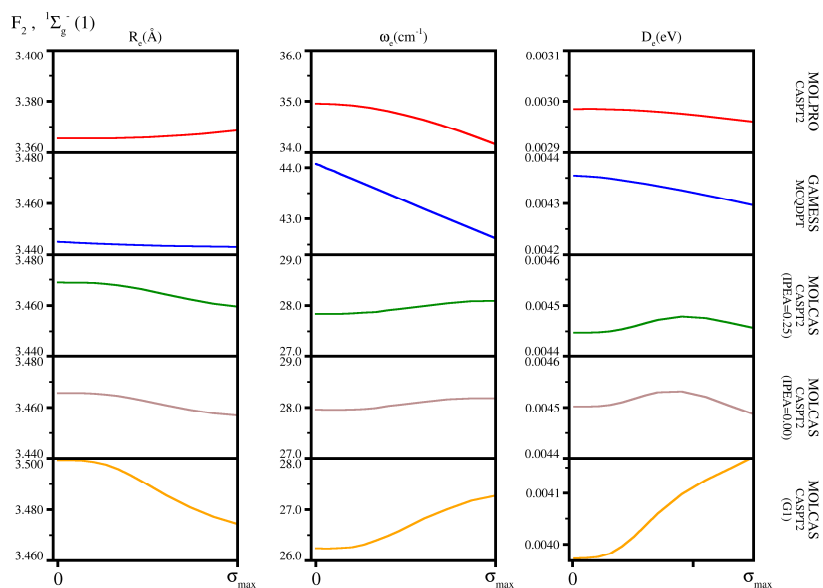


Figure 6.62 Spectroscopic constants for the $^1\Sigma_g^-(1)$ state of F_2 obtained using different methods with various values of the shift parameter σ .

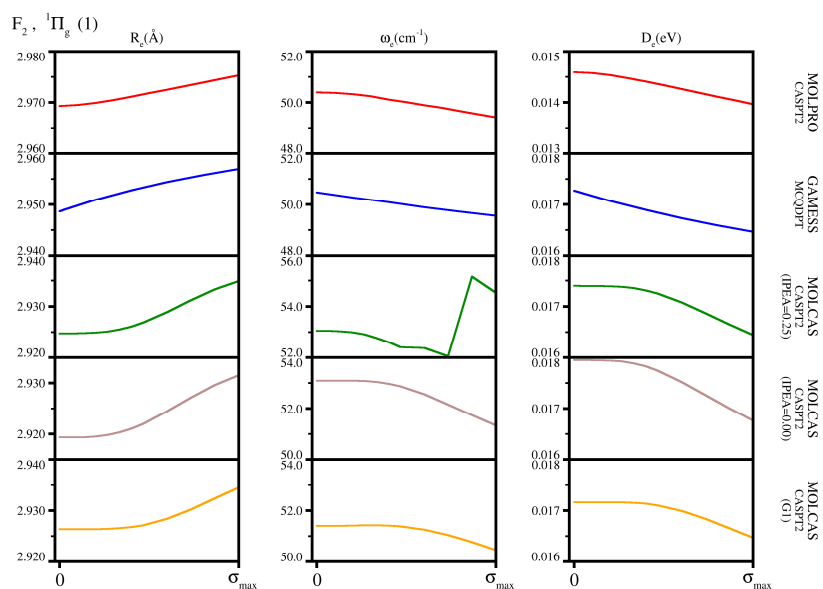


Figure 6.63 Spectroscopic constants for the $^1\Pi_g(1)$ state of F_2 obtained using different methods with various values of the shift parameter σ .

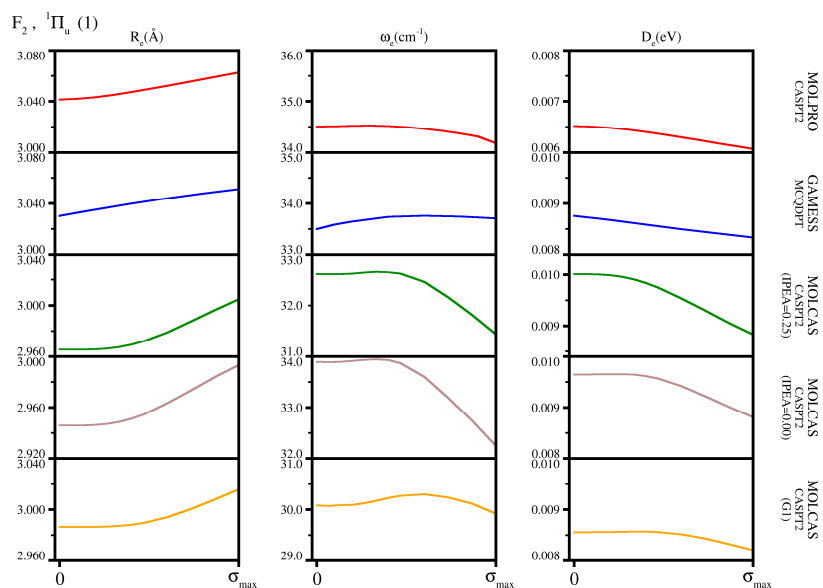


Figure 6.64 Spectroscopic constants for the $^1\Pi_u(1)$ state of F_2 obtained using different methods with various values of the shift parameter σ .

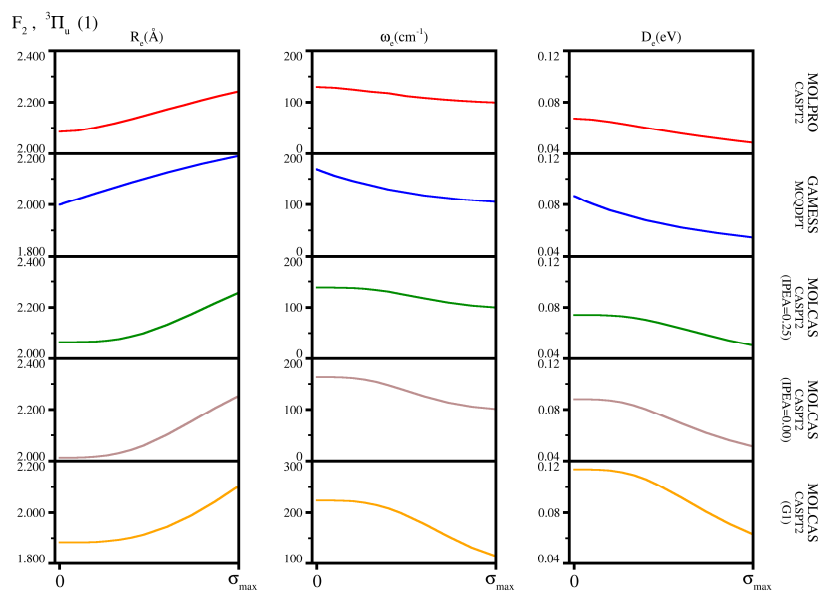


Figure 6.65 Spectroscopic constants for the $^3\Pi_u(1)$ state of F_2 obtained using different methods with various values of the shift parameter σ .

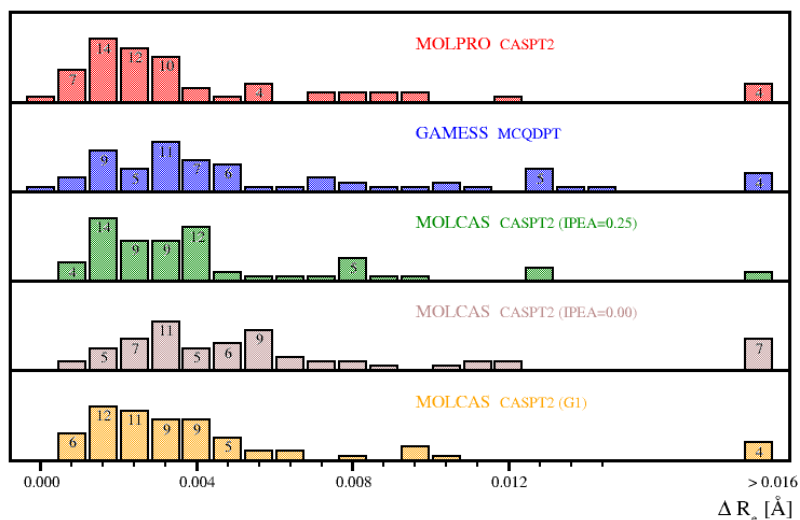


Figure 6.66 Distribution of changes in R_e induced by changing the intruder state removal parameter within whole studied shift values.

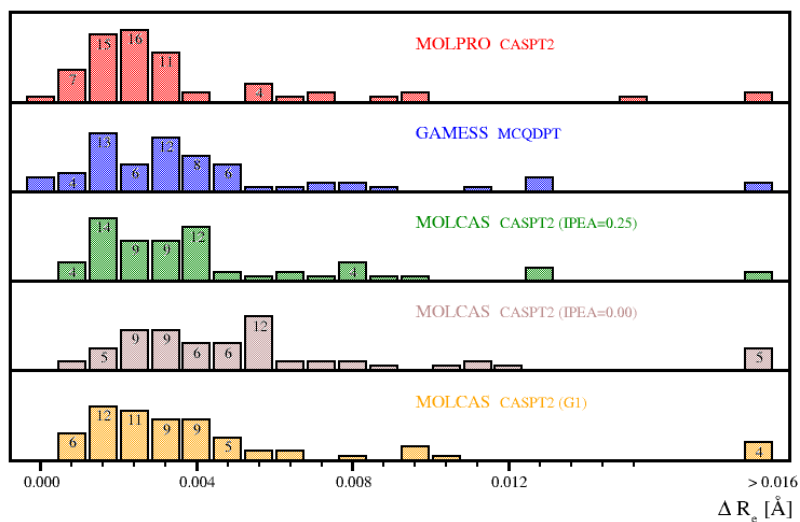


Figure 6.67 Distribution of changes in R_e induced by changing the intruder state removal parameter ignoring the region of yellow boxes in Figures 6.1-6.65.

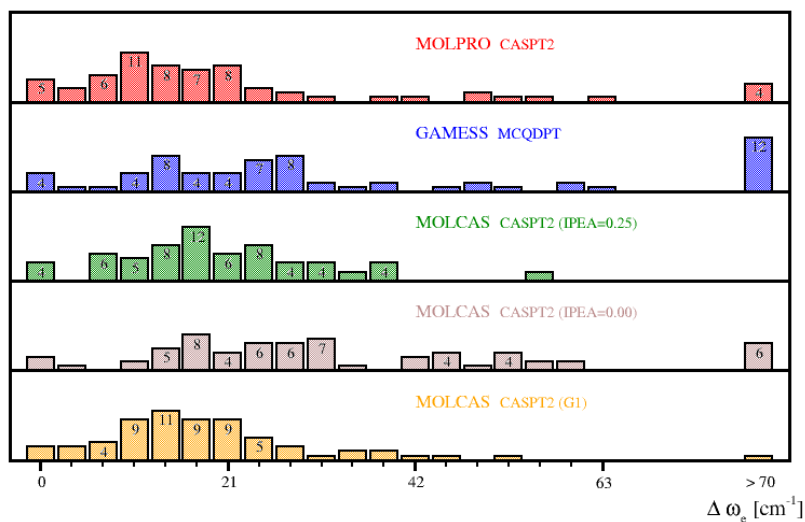


Figure 6.68 Distribution of changes in ω_e induced by changing the intruder state removal parameter within whole studied range of the shift values.

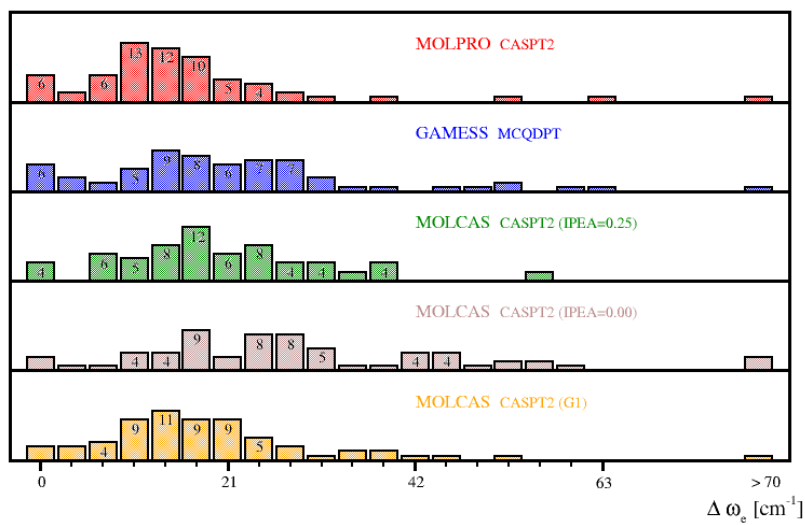


Figure 6.69 Distribution of changes in ω_e induced by changing the intruder state removal parameter ignoring the region of yellow boxes in Figures 6.1-6.65.

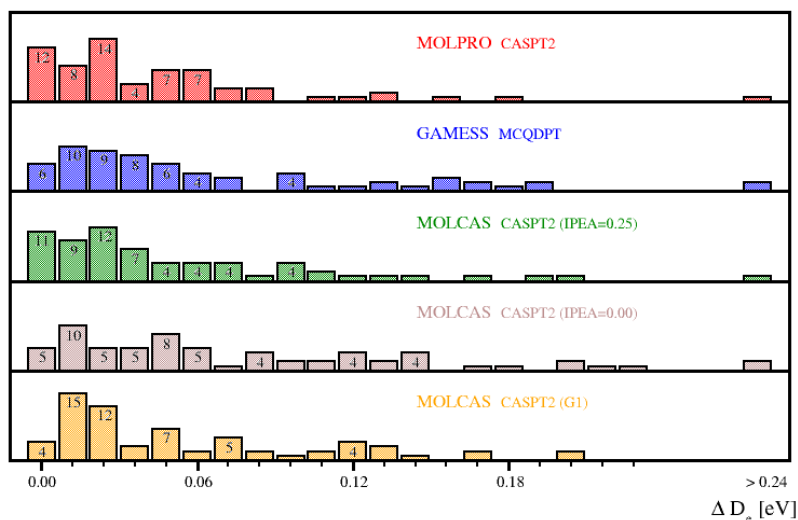


Figure 6.70 Distribution of changes in D_e induced by changing the intruder state removal parameter within whole studied range of the shift values.

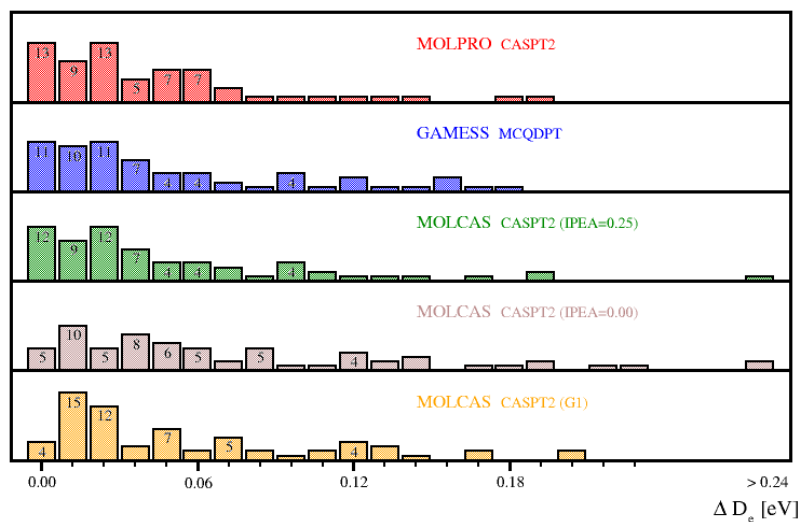


Figure 6.71 Distribution of changes in D_e induced by changing the intruder state removal parameter ignoring the region of yellow boxes in Figures 6.1-6.65.

Mean absolute deviation from experiment for equilibrium distances [in Å]

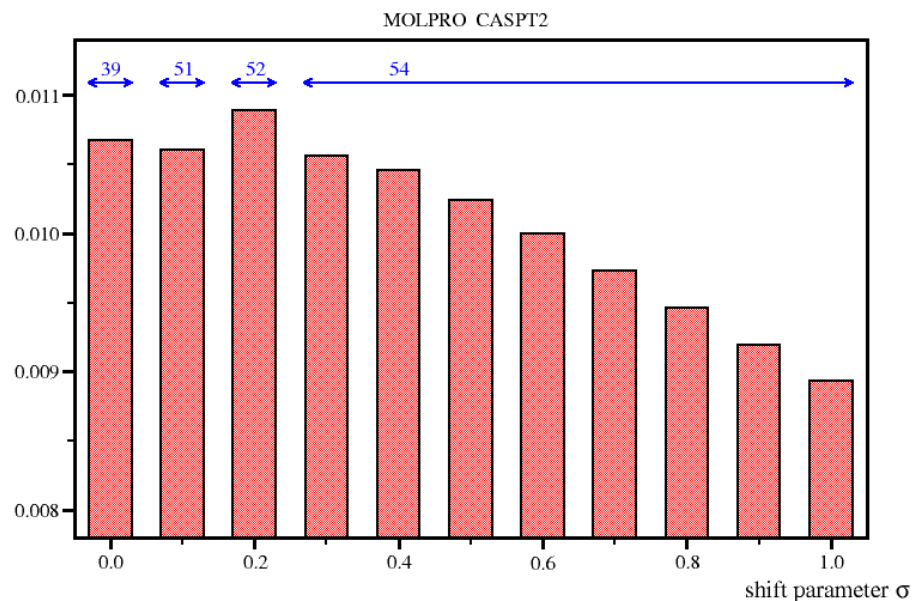


Figure 6.72 Mean absolute deviation from the experiment for R_e obtained with CASPT2/MOLPRO method.

Mean absolute deviation from experiment for equilibrium distances [in Å]

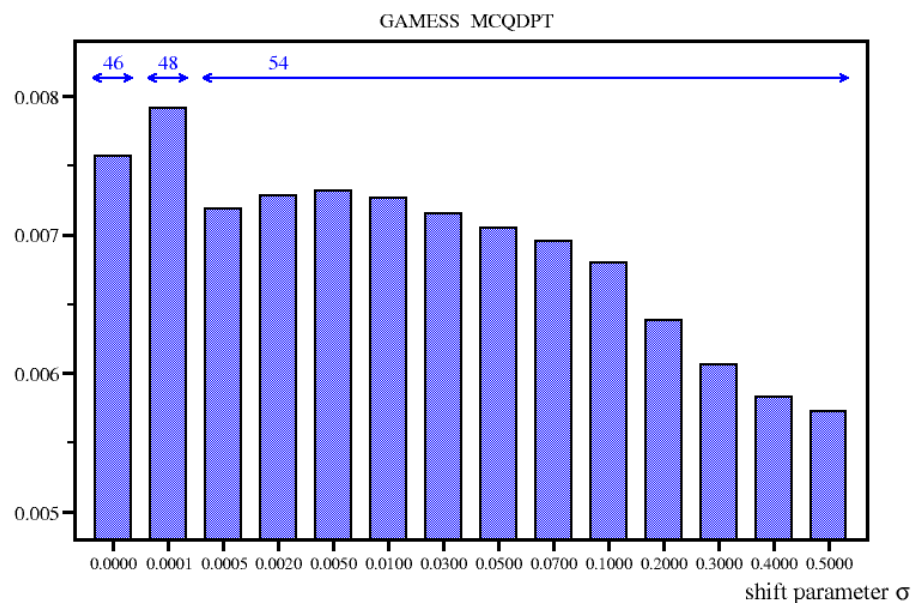


Figure 6.73 Mean absolute deviation from the experiment for R_e obtained with MCQDPT/GAMESS method.

Mean absolute deviation from experiment for equilibrium distances [in Å]

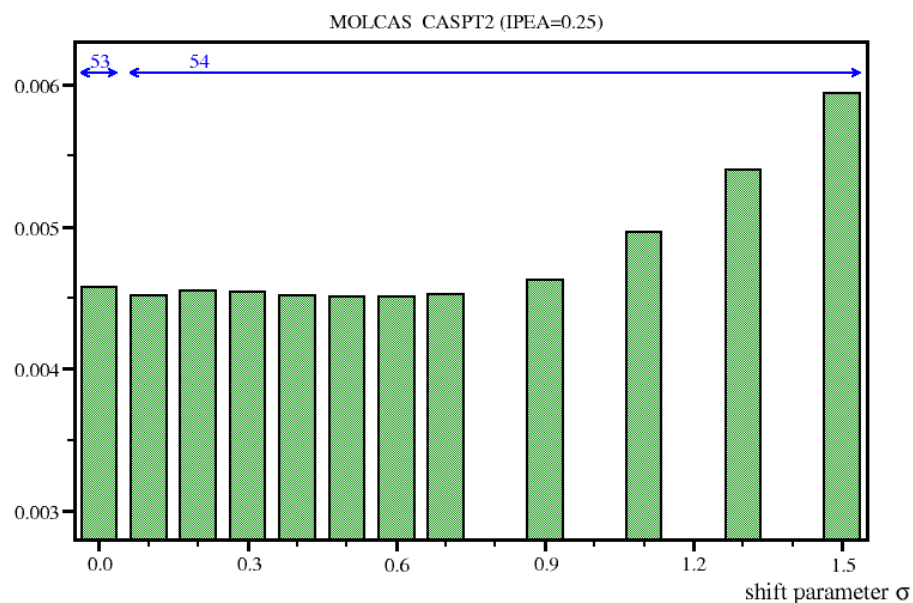


Figure 6.74 Mean absolute deviation from the experiment for R_e obtained with IPEA-CASPT2/MOLCAS method.

Mean absolute deviation from experiment for equilibrium distances [in Å]

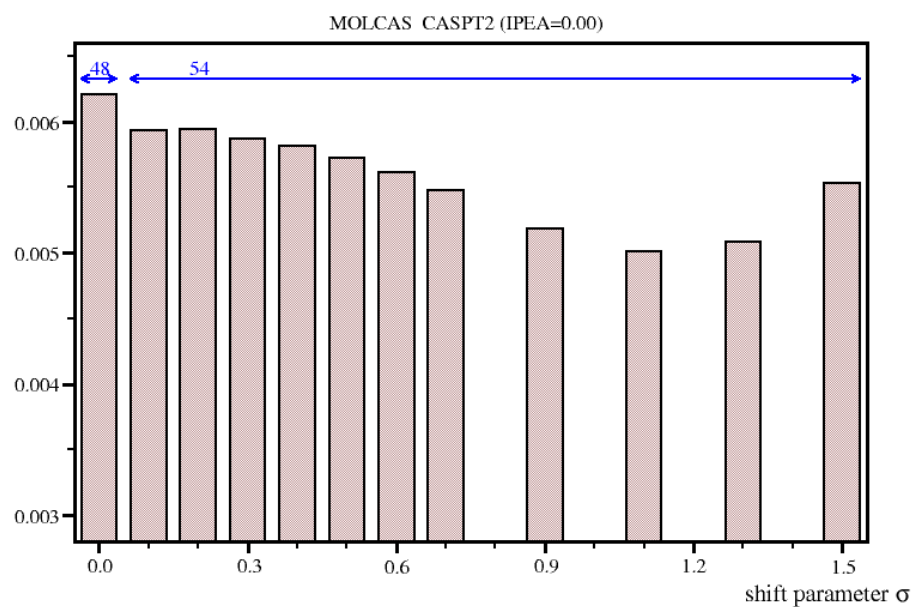


Figure 6.75 Mean absolute deviation from the experiment for R_e obtained with CASPT2/MOLCAS method.

Mean absolute deviation from experiment for equilibrium distances [in Å]

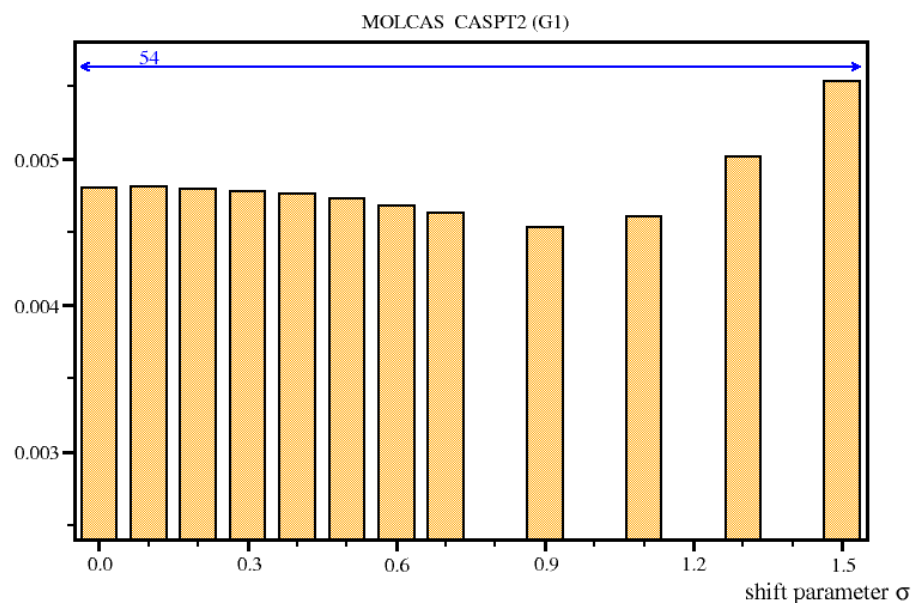


Figure 6.76 Mean absolute deviation from the experiment for R_e obtained with G1-CASPT2/MOLCAS method.

Mean absolute deviation from experiment for equilibrium frequencies [in cm^{-1}]

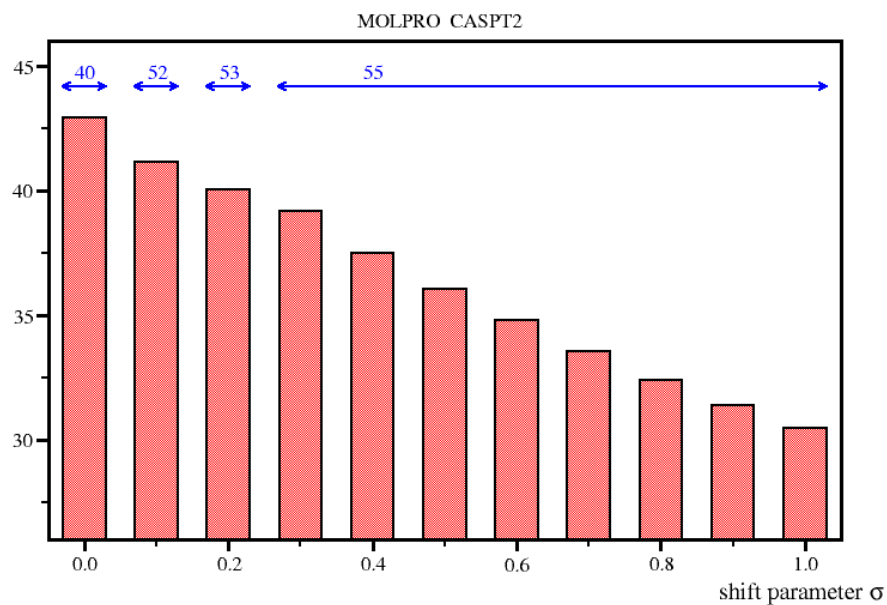


Figure 6.77 Mean absolute deviation from the experiment for ω_e obtained with CASPT2/MOLPRO method.

Mean absolute deviation from experiment for equilibrium frequencies [in cm^{-1}]

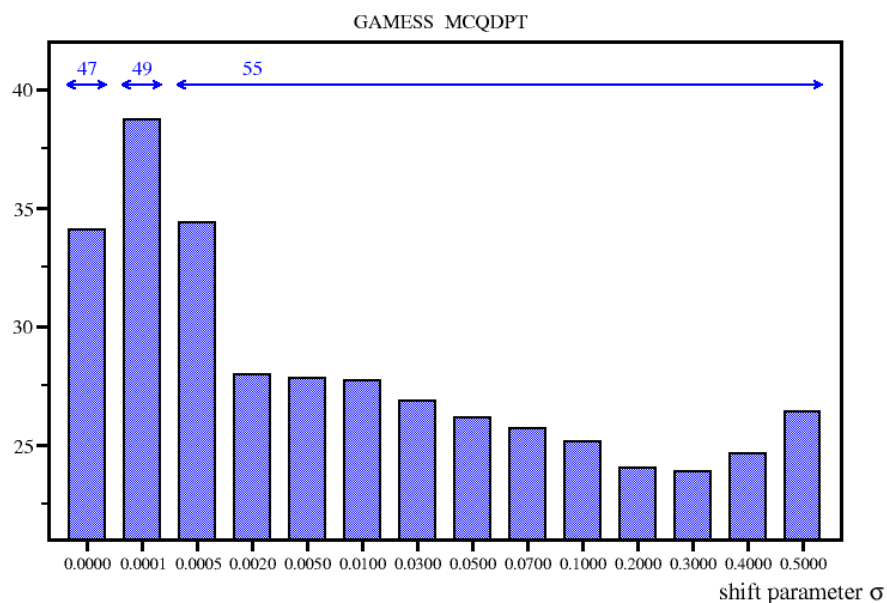


Figure 6.78 Mean absolute deviation from the experiment for ω_e obtained with MCQDPT/GAMESS method.

Mean absolute deviation from experiment for equilibrium frequencies [in cm^{-1}]

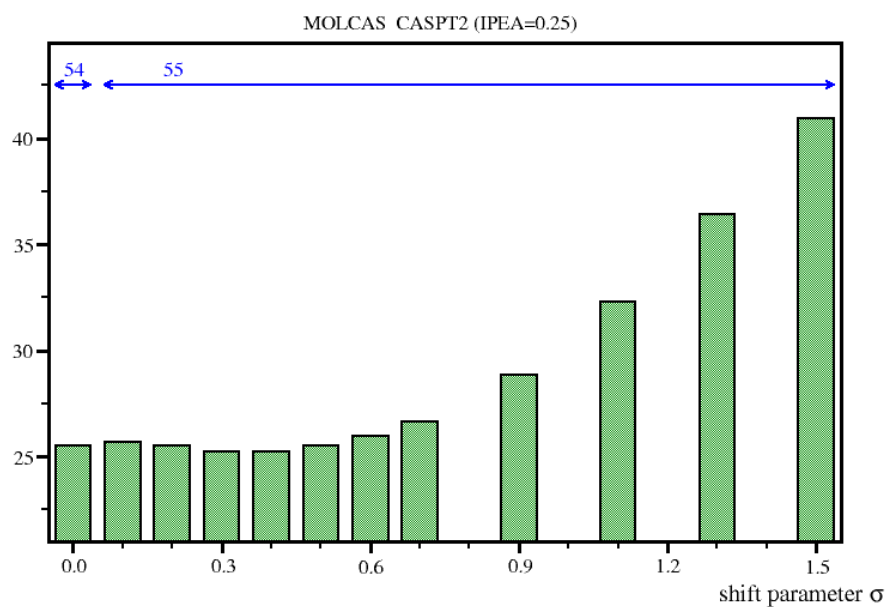


Figure 6.79 Mean absolute deviation from the experiment for ω_e obtained with IPEA-CASPT2/MOLCAS method.

Mean absolute deviation from experiment for equilibrium frequencies [in cm^{-1}]

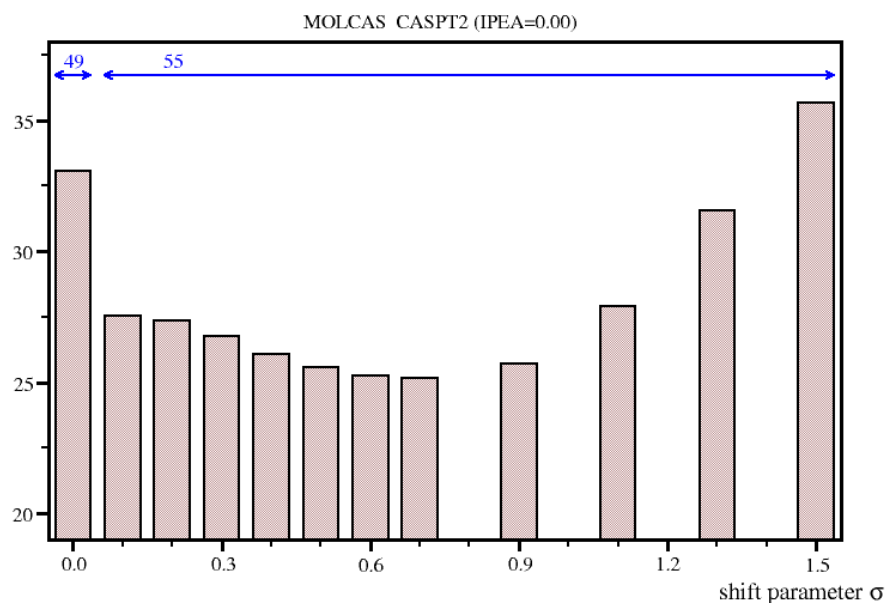


Figure 6.80 Mean absolute deviation from the experiment for ω_e obtained with CASPT2/MOLCAS method.

Mean absolute deviation from experiment for equilibrium frequencies [in cm^{-1}]

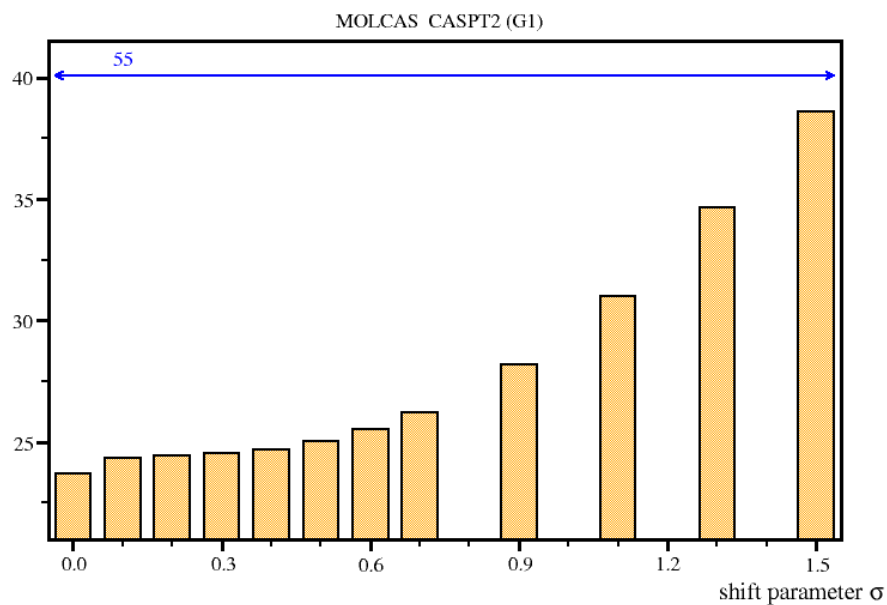


Figure 6.81 Mean absolute deviation from the experiment for ω_e obtained with G1CASPT2/MOLCAS method.

Mean absolute deviation from experiment for equilibrium dissociation energies [in eV]

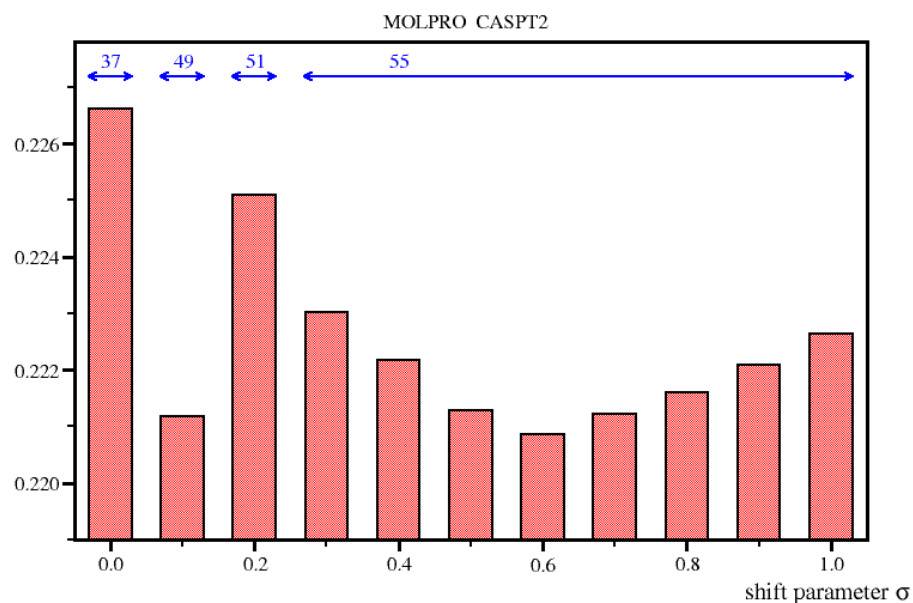


Figure 6.82 Mean absolute deviation from the experiment for D_e obtained with CASPT2/MOLPRO method.

Mean absolute deviation from experiment for equilibrium dissociation energies [in eV]

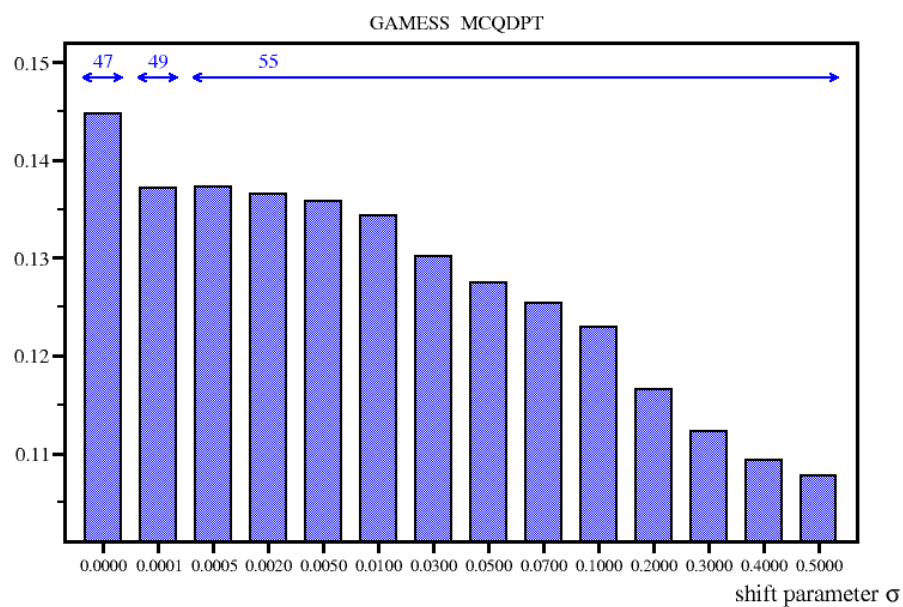


Figure 6.83 Mean absolute deviation from the experiment for D_e obtained with MCQDPT/GAMESS method.

Mean absolute deviation from experiment for equilibrium dissociation energies [in eV]

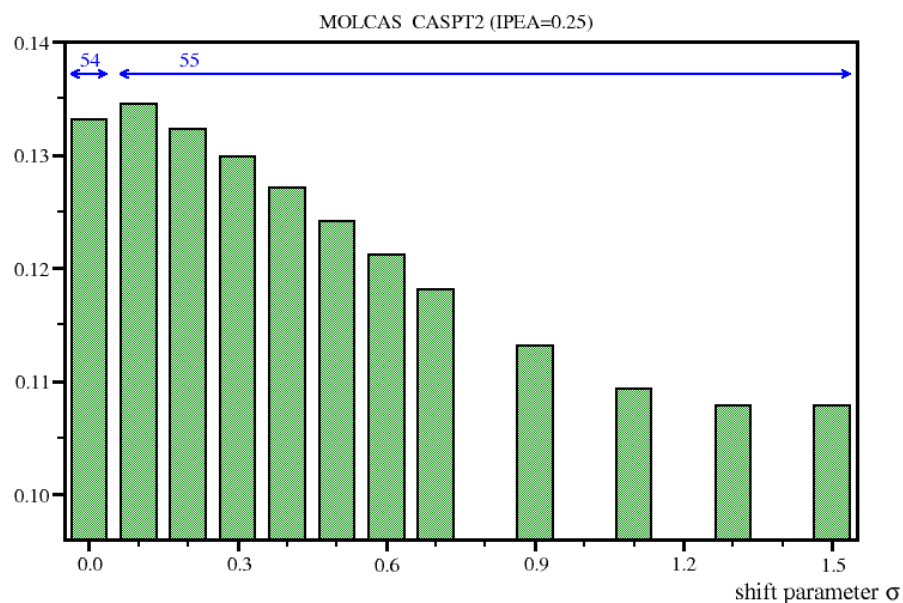


Figure 6.84 Mean absolute deviation from the experiment for D_e obtained with IPEA-CASPT2/MOLCAS method.

Mean absolute deviation from experiment for equilibrium dissociation energies [in eV]

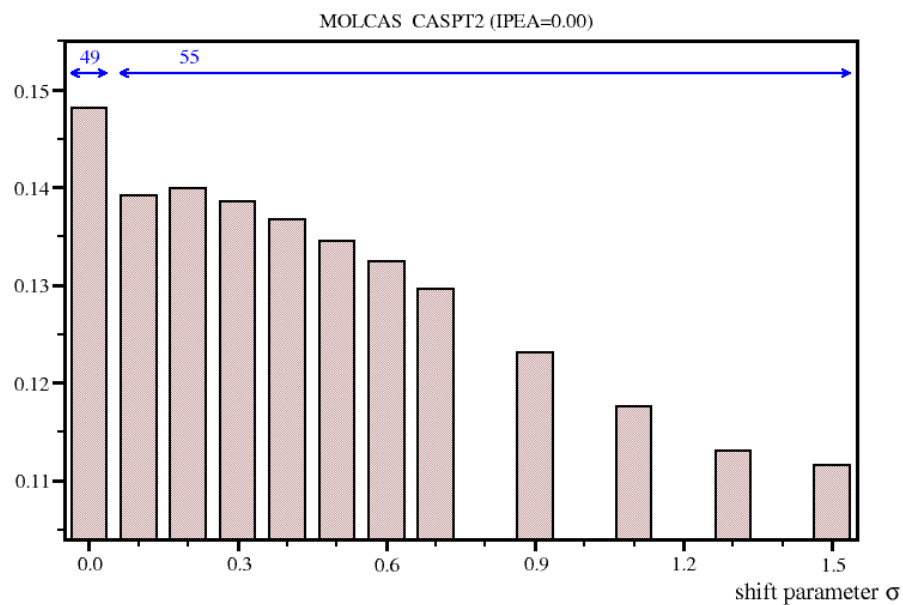


Figure 6.85 Mean absolute deviation from the experiment for D_e obtained with CASPT2/MOLCAS method.

Mean absolute deviation from experiment for equilibrium dissociation energies [in eV]

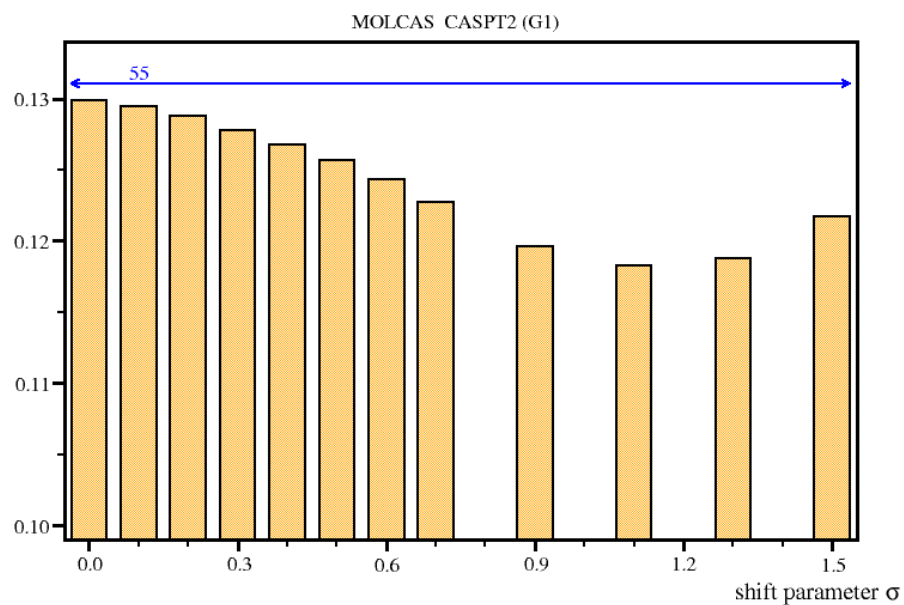


Figure 6.86 Mean absolute deviation from the experiment for D_e obtained with G1-CASPT2/MOLCAS method.

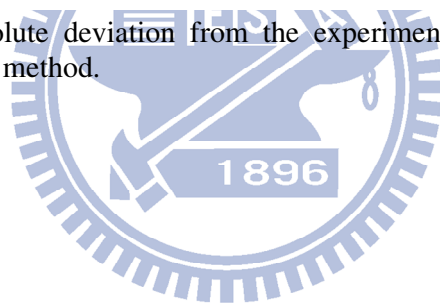


Table 1 The low-lying electronic states included in the MRPT calculations and numbers of available experimental data for diatomic molecules.

System	Number of states	States	Number of experimental data		
			ω_e	R_e	D_e
BH	4	X $^1\Sigma^+$ a $^3\Pi$ A $^1\Pi$ b $^3\Sigma^-$	2	4	2
CH	3	X $^2\Pi$ a $^4\Sigma^-$ A $^2\Delta$	3	3	3
NH	4	X $^3\Sigma^-$ a $^1\Delta$ b $^1\Sigma^+$ A $^3\Pi$	4	4	4
OH	2	X $^2\Pi$ A $^2\Sigma^+$	2	2	2
HF	1	X $^1\Sigma^+$	1	1	1
BF	3	X $^1\Sigma^+$ A $^1\Pi$ a $^3\Pi$	3	3	3
CN	1	A $^2\Pi$	1	1	1
CO	9	X $^1\Sigma^+$ A $^1\Pi$ I $^1\Sigma^-$ D $^1\Delta$ a' $^3\Sigma^+$ d $^3\Delta$ a $^3\Pi$ e' $^3\Sigma^-$ s $^3\Pi$ (1)	8	8	8
NO	6	X $^2\Pi$ B $^2\Pi$ $^2\Phi$ (1) a' $^4\Pi$ b' $^4\Sigma^-$ B' $^2\Delta$	5	3	5
FO	1	X $^2\Pi$	1	1	1
B ₂	1	X $^3\Sigma_g^-$	1	1	1
C ₂	10	X $^1\Sigma_g^+$ $^1\Delta_g$ (1) $^1\Sigma_g^+$ (2) a $^3\Pi_u$ b $^3\Sigma_g^-$ A $^1\Pi_u$ c $^3\Sigma_u^+$ d $^3\Pi_g$ e $^3\Pi_g$ C $^1\Pi_g$	8	8	8
N ₂	9	X $^1\Sigma_g^+$ A $^3\Sigma_u^+$ B $^3\Pi_g$ W $^3\Delta_u$ B' $^3\Sigma_u^-$ B'' $^3\Sigma_u^-$ a' $^1\Sigma_u^-$ a $^1\Pi_g$ w $^1\Delta_u$ C $^3\Pi_u$	9	8	9
O ₂	6	X $^3\Sigma_g^-$ a $^1\Delta_g$ b $^1\Sigma_g^+$ c $^1\Sigma_u^-$ A' $^3\Delta_u$ A $^3\Sigma_u^+$	6	6	6
F ₂	5	X $^1\Sigma_g^+$ $^1\Sigma_g^-$ (1) $^1\Pi_g$ (1) $^1\Pi_u$ (1) $^3\Pi_u$ (1)	1	1	1
Total	65		55	54	55

Table 2 Experimental data of the low-lying states for diatomic molecules.

System	State	Experimental data		
		ω_e [cm ⁻¹] ^a	R_e [Å] ^a	D_e [eV] ^b
BH	X ¹ Σ ⁺	2367	1.232	3.524
	a ³ Π	... ^c	1.201	... ^c
	A ¹ Π	2251	1.219	0.655
	b ³ Σ ⁻	... ^c	1.227	... ^c
CH	X ² Π	2859	1.120	3.647
	a ⁴ Σ ⁻	3145	1.085	2.923
	A ² Δ	2931	1.102	2.032
NH	X ³ Σ ⁻	3282	1.036	3.671
	a ¹ Δ	3188	1.034	4.497
	b ¹ Σ ⁺	3352	1.036	4.618
	A ³ Π	3231	1.037	2.359
OH	X ² Π	3738	0.970	4.621
	A ² Σ ⁺	3179	1.012	2.527
HF	X ¹ Σ ⁺	4138	0.917	6.110
BF	X ¹ Σ ⁺	1402	1.263	7.957
	A ¹ Π	1324	1.308	4.344
	a ³ Π	1265	1.304	1.614
CN	A ² Π	1813	1.233	6.549
CO	X ¹ Σ ⁺	2170	1.128	11.244
	A ¹ Π	1518	1.235	3.176
	I ¹ Σ ⁻	1092	1.391	3.175
	D ¹ Δ	1094	1.399	3.070
	a' ³ Σ ⁺	1229	1.352	4.322
	d ³ Δ	1172	1.370	3.666
	a ³ Π	1743	1.206	5.208
	e ³ Σ ⁻	1118	1.384	3.280
	⁵ Π (1)	... ^c	... ^c	... ^c

Table 2 (continued)

System	State	Experimental data			
		ω_e [cm ⁻¹] ^a	R_e [Å] ^a	D_e [eV] ^b	
NO	X ² Π	1904	1.151	6.605	
	B ² Π	1037	1.417	3.296	
	² Φ (1)	... ^c	... ^c	... ^c	
	a ⁴ Π	1017	... ^c	1.839	
	b ⁴ Σ ⁻	1206	... ^c	2.536	
	B' ² Δ	1217	1.302	1.504	
	FO	X ² Π	1029	1.326	1.670
B ₂	X ³ Σ _g ⁻	1051	1.59	3.102	
C ₂	X ¹ Σ _g ⁺	1855	1.243	6.354	
	¹ Δ _g (1)	... ^c	... ^c	... ^c	
	¹ Σ _g ⁺ (2)	... ^c	... ^c	... ^c	
	a ³ Π _u	1641	1.312	6.265	
	b ³ Σ _g ⁻	1470	1.369	5.556	
	A ¹ Π _u	1608	1.318	5.313	
	c ³ Σ _u ⁺	1962	1.230	4.703	
	d ³ Π _g	1788	1.266	3.871	
	e ³ Π _g	1107	1.535	2.556	
	C ¹ Π _g	1809	1.255	2.106	
	N ₂	X ¹ Σ _g ⁺	2359	1.098	9.906
		A ³ Σ _u ⁺	1461	1.287	3.681
		B ³ Π _g	1733	1.213	4.898
W ³ Δ _u		1501	... ^c	4.874	
B' ³ Σ _u ⁻		1517	1.278	5.265	
a' ¹ Σ _u ⁻		1530	1.276	6.223	
a ¹ Π _g		1694	1.220	6.083	
w ¹ Δ _u		1559	1.268	5.734	
C ³ Π _u		2047	1.149	1.238	

Table 2 (continued)

System	State	Experimental data		
		ω_e [cm ⁻¹] ^a	R_e [Å] ^a	D_e [eV] ^b
O ₂	X ³ Σ _g ⁻	1580	1.208	5.213
	a ¹ Δ _g	1484	1.216	4.232
	b ¹ Σ _g ⁺	1433	1.227	3.577
	c ¹ Σ _u ⁻	794	1.517	1.115
	A' ³ Δ _u	850	1.48	0.912
	A ³ Σ _u ⁺	799	1.522	0.825
F ₂	X ¹ Σ _g ⁺	917	1.412	1.661
	¹ Σ _g ⁻ (1)	... ^c	... ^c	... ^c
	¹ Π _g (1)	... ^c	... ^c	... ^c
	¹ Π _u (1)	... ^c	... ^c	... ^c
	³ Π _u (1)	... ^c	... ^c	... ^c

^a Experimental value, Ref. 27.

^b Experimental value, Ref. 28.

^c No experimental data available.

Table 3 Conversion of coefficients from spherical harmonic type to Cartesian type.

Orbital type	Cartesian type ^a	Spherical harmonic type ^b
S	S	S
P	P_x	P_x
	P_y	P_y
	P_z	P_z
D	D_{x^2}	$-\frac{1}{2}D_0 + \frac{\sqrt{3}}{2}D_{+2}$
	D_{y^2}	$-\frac{1}{2}D_0 - \frac{\sqrt{3}}{2}D_{+2}$
	D_{z^2}	D_0
	D_{xy}	D_{-2}
	D_{xz}	D_{+1}
	D_{yz}	D_{-1}

Table 3 (continued)

Orbital type	Cartesian type ^a	Spherical harmonic type ^b
F	F_{x^3}	$-\frac{\sqrt{3}}{2\sqrt{2}}F_{+1} - \frac{\sqrt{5}}{2\sqrt{2}}F_{+3}$
	F_{y^3}	$-\frac{\sqrt{3}}{2\sqrt{2}}F_{-1} - \frac{\sqrt{5}}{2\sqrt{2}}F_{-3}$
	F_{z^3}	F_0
	F_{x^2y}	$-\frac{\sqrt{3}}{2\sqrt{10}}F_{-1} + \frac{3}{2\sqrt{2}}F_{-3}$
	F_{x^2z}	$-\frac{3}{2\sqrt{5}}F_0 + \frac{\sqrt{3}}{2}F_{+2}$
	F_{xy^2}	$-\frac{\sqrt{3}}{2\sqrt{10}}F_{+1} + \frac{3}{2\sqrt{2}}F_{+3}$
	F_{y^2z}	$-\frac{3}{2\sqrt{5}}F_0 - \frac{\sqrt{3}}{2}F_{+2}$
	F_{x^2z}	$\sqrt{\frac{6}{5}}F_{+1}$
	F_{yz^2}	$\sqrt{\frac{6}{5}}F_{-1}$
	F_{xyz}	F_{-2}

^a Cartesian Gaussian type functions $g_{ijk} = Nx^{n_x}y^{n_y}z^{n_z}e^{-\alpha r^2}$ with $n = n_x + n_y + n_z$

can be combined to $\frac{(n+1)(n+2)}{2}$ atomic orbitals. The correspondence of each orbital is as follows: $n = 0$ for S-type, $n = 1$ for P-type, $n = 2$ for D-type, etc.

^b Spherical Gaussian type functions $g_{nlm} = Nr^{n-1}e^{-\alpha r^2}(Y_l^{m*} \pm Y_l^m)$ present $2l + 1$ real atomic orbitals formed from the linear combinations of spherical harmonic functions. The correspondence of each orbital as follow: $l = 0$ for S-type, $l = 1$ for P-type, $l = 2$ for D-type, etc.

Appendix A

Theoretical Study of *p*-Nitroaniline for the Infrared Spectra of Ground State and the Lowest Triplet State

A.1 Introduction

In Appendix A, the main objective is to provide a theoretical interpretation of the experimentally observed infrared spectra (IR) of *p*-nitroaniline (PNA), dissolved in CD₃CN. We are mainly interested in two electronic states of PNA, its singlet ground state, S₀ and the lowest excited triplet state, T₁. A Simulation of IR spectrum in a liquid solution requires a time-dependent investigation of dynamics of an ensemble of PNA/CD₃CN molecules at some finite temperature. Namely, obtaining the IR spectrum consists of running a molecular dynamics trajectory for such an ensemble followed by a Fourier transformation of the resulting dipole moment autocorrelation function. Unfortunately, the development of computational methods does not provide us with a technique, which is feasible and applicable for our systems, in particular for excited states. For this reason, we employed traditional, time-independent methods to

interpret the IR spectra of the PNA. Here, we used DFT calculation with the B3LYP exchange correlation functional^{29,30,31} to optimize structures of the PNA and to simulate the IR spectra in a harmonic approximation.

We attempted to provide the IR spectra from gas-phase calculations for PNA and from analogous polarizable continuum model (PCM) calculations³² but the results were unsatisfactory. Fortunately, we found a different line of approach, which is using explicitly solvated models³³ to acquire a good agreement with the experimental results for S_0 and T_1 of PNA.

A.2 Computational Details

Usually, IR spectra of molecules in liquid phase is interpreted by use of the calculation of a bare, gas-phase molecule, assuming that there is no sharp difference between the gas-phase and solvated system spectra. Here, we investigated the singlet ground state of PNA and compared the result with accurate experimental data. After finding a molecular model that was able to reproduce the observed ground-state spectrum of PNA in a satisfactory manner, we have proceeded to interpretation of the triplet-state IR spectrum of PNA.

All the calculations, including geometry optimization, frequency calculations with IR intensity determination, and the PCM calculation with dielectric constant (here $\epsilon = 37.5$ for CD_3CN) were performed using the DFT/B3LYP/cc-pVTZ computational strategy as implemented in the Gaussian 09 program. It was found that

slight elongation of the optimized C–NH₂ bond in the explicitly solvated model leads to substantial improvement in the simulated spectra. The remaining geometrical parameters were reoptimized with keeping the C–NH₂ bond distance constant. The following calculations of vibrational frequencies and IR intensities were found almost insensitive to this procedure. The simulated IR spectra were plotted by MOLDEN program with a half-width of 8 cm⁻¹. Due to the lack of harmonicity, we uniformly scaled the vibrational frequencies by a constant factor of 0.972.

A.3 Results and Discussion

A.3.1 Failure of Simulated Gas-phase and PCM IR Spectra for Singlet Ground State of PNA

The S₀ experimental IR spectrum of PNA dissolved in CD₃CN (see Figure A.1a) shows four major bands, located around 1320, 1500, 1600, and 1630 cm⁻¹. According to theoretical calculations, these bands are dominated by the symmetric NO₂ stretch, antisymmetric NO₂ stretch, and two combinations of the NH₂ scissoring motion with the phenyl ring stretch, respectively. The most characteristic of these peaks is the symmetric NO₂ stretch with a doublet of peaks centered around 1320 cm⁻¹.

The simulated gas-phase B3LYP IR spectrum of S₀ PNA (see Figure A.1b) is in apparent contrast with the experimental results. First of all, the spectral window between 1250 and 1350 cm⁻¹ displays two, well-separated strong bands with reversed

intensity pattern. Other major bands between 1450 and 1650 cm^{-1} are distinct from the experiment.

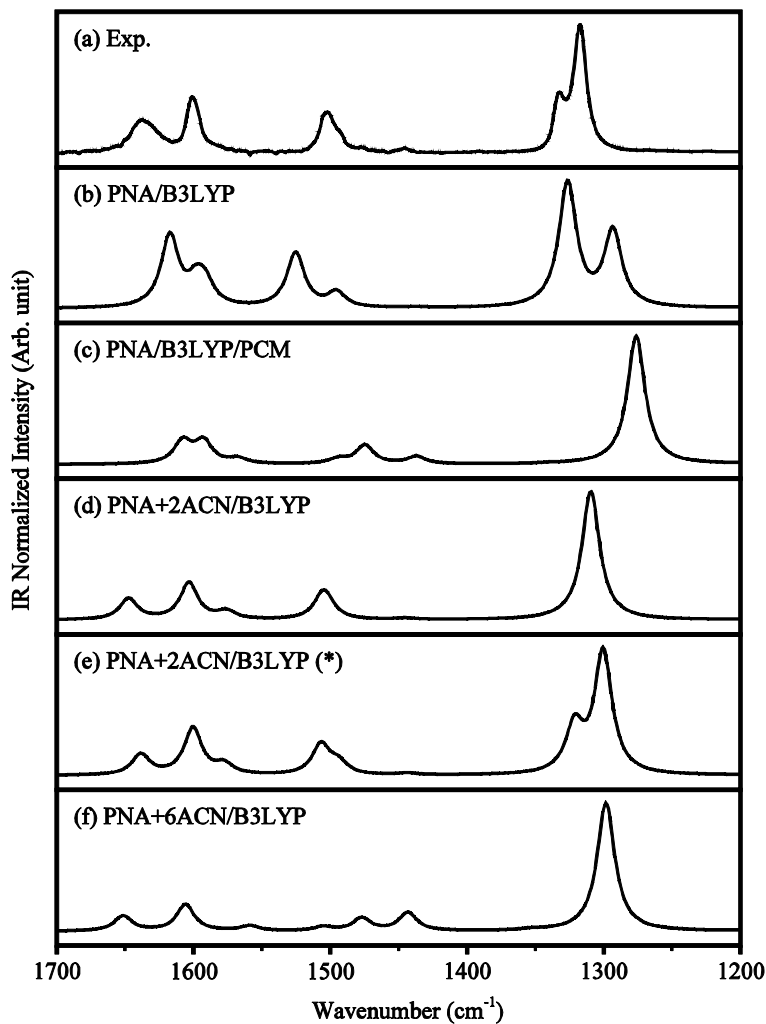


Figure A.1 Experimental and computational IR spectra for singlet ground state of PNA. The asterisk symbol indicates the spectra obtained from the PNA+2ACN with the elongation of C–NH₂ model.

These unsatisfactory results are probably attributed to ignoring the solvation of PNA by CD₃CN. We have taken into account the solvent effects by combining polarizable continuum model (PCM) with DFT calculation. The simulated B3LYP/PCM IR

spectrum (see Figure A.1c) does not give any improvement over the gas-phase calculations because of the two following reasons. One is that the resulting spectrum still displays only a single peak corresponding to the doublet at 1320 cm^{-1} . The other is that the intensities of observable bands between 1400 and 1650 cm^{-1} are relatively weak and mismatch the experiment.

A.3.2 Simulated IR Spectra of S_0 PNA Using Explicitly Solvated Models

Fortunately, there is a way to consider the solvent effect by employing an explicitly solvated model of PNA, in which two CD_3CN molecules (see Figure A.2b) are hydrogen-bonded to the NH_2 group. The resulting spectrum (see Figure A.1d) displays very good agreement with the experimental data except for the missing hump in the 1320 cm^{-1} band. We have considered a multitude of various explicitly solvated models containing one to six CD_3CN molecules (see Figure A.2c) attached either to the NH_2 group, the NO_2 group, or aligned along the ring. It has been found that all the resulting spectra are quite similar with a strong single band between 1300 and 1400 cm^{-1} and reasonable agreement with experiment in the 1600 – 1700 cm^{-1} region. For explicitly solvated models with four or more solvent molecules, two split bands around 1500 cm^{-1} does not model the experimentally observed pattern.

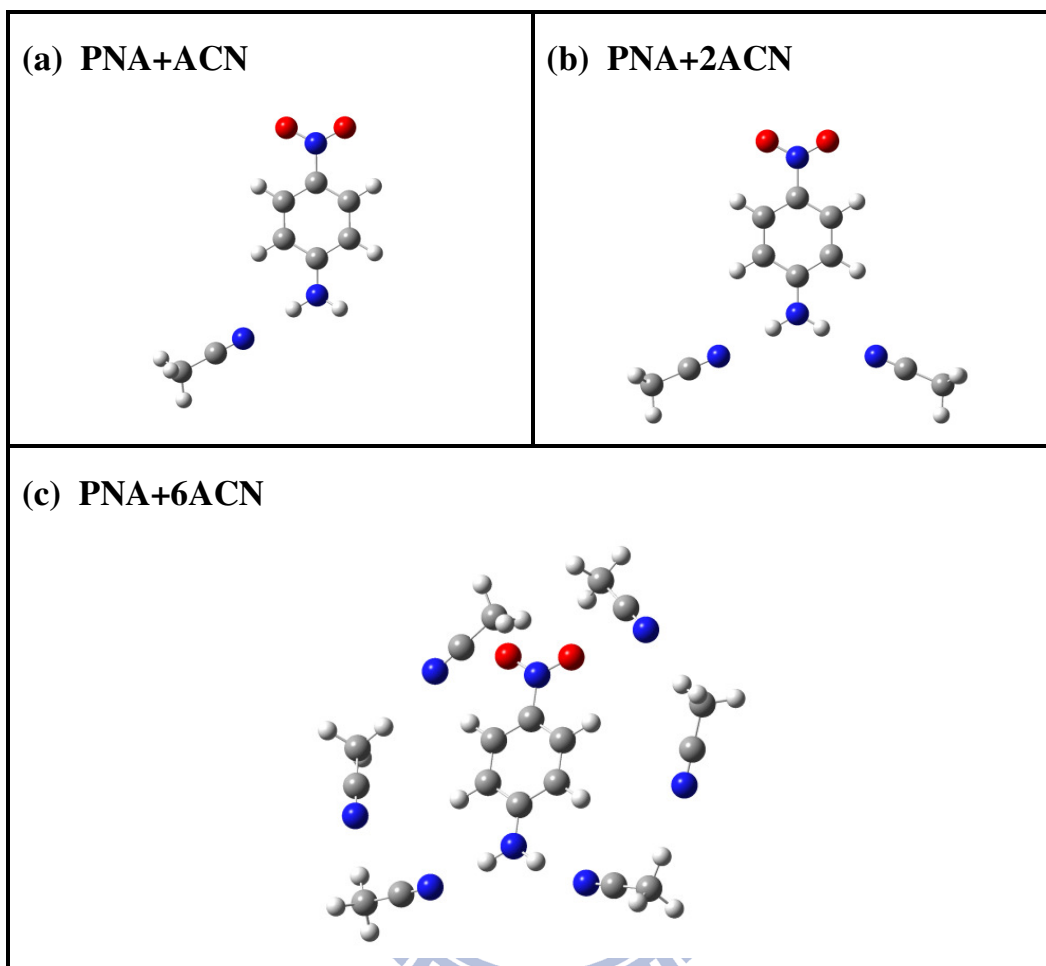


Figure A.2 Schematic geometries of the explicitly solvated models.

A.3.3 Slight Elongation of the Explicitly Solvated Models for Improving Simulated IR Spectrum of S_0 PNA

In this study, we observe that some of the explicitly solvated models with only one CD_3CN attached to the NH_2 group (see Figure A.2a), show a doublet of bands at around 1320 cm^{-1} . However, the equilibrium geometries of this model are not quite

different from the other explicitly solvated models. We observed that one missing peak of doublet of bands is mainly concerned about the vibrational motion of the NH_2 group. We have anticipated the small variations of the equilibrium geometry with the NH_2 group can have quite substantial influence on the simulated spectra. Investigating various out-of-plane NH_2 group motions and elongation/contraction of the C-NH_2 , we have found a dramatic change in the spectrum with the variation of the C-NH_2 distance. Slight elongation (0.012 \AA) of the C-NH_2 bond from its equilibrium length (1.352 \AA) produces a hump on the single band at 1300 cm^{-1} and gives a perfect agreement between this simulated spectrum (see Figure A.1e) and the experimental result. The largest change in the elongated PNA vibrational frequencies in this simulated IR spectrum is only 15 cm^{-1} .

We also investigated simulated and experimental IR spectra of isotope-substituted PNA ($\text{PNA-}^{15}\text{NH}_2$ and $\text{PNA-}^{15}\text{NO}_2$), which provided additional verification. In the experimental spectra of the $\text{PNA-}^{15}\text{NH}_2$ (see Figure A.3c), the isotope effect caused a reparation of the doublet of bands at around 1320 cm^{-1} into two peaks with a distinct spacing and similar intensities. Our simulated spectrum of the $\text{PNA-}^{15}\text{NH}_2+2\text{ACN}$ model (see dotted line, Figure A.3d) shows only a single peak at this region but the other strong peak is recovered after elongating the bond length in the same way as described above (see solid line, Figure A.3d). On the other side, the experimental spectrum of the $\text{PNA-}^{15}\text{NO}_2$ (see dotted line, Figure A.3e) shows a red-shifted, single band at 1300 cm^{-1} and three weak bands between 1420 and 1520 cm^{-1} . Both the simulated spectra of the $\text{PNA-}^{15}\text{NO}_2+2\text{ACN}$ model (see solid line,

Figure A.3e) with and without elongation of C–NH₂ can predict the isotope substitution correctly.

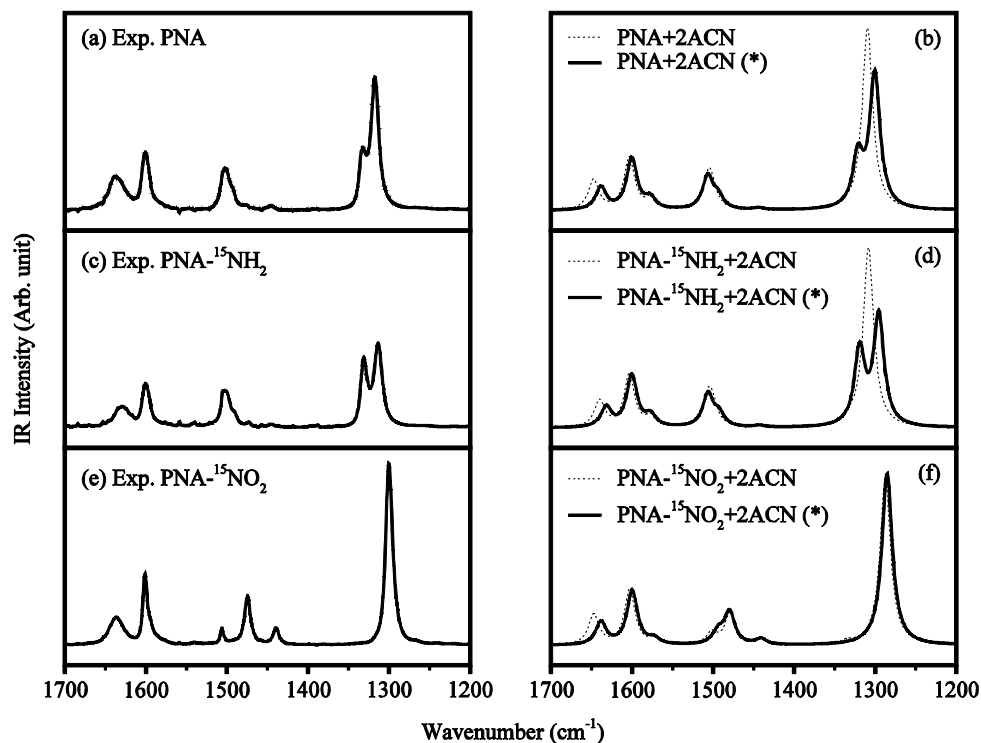


Figure A.3 Experimental and computational IR spectra for singlet ground state of PNA and isotope-substituted PNA. The IR spectra obtained from PNA+2ACN (dotted line) and PNA+2ACN with the elongation of C–NH₂ (solid line) models.

As mentioned above, the IR spectra of the explicitly solvated PNA model give good agreement with the experiment of PNA and its isotopomers. The applied elongation is small when compared with a typical error (0.01 Å) of DFT calculation. In addition, the bond lengths of the C–NH₂ in the explicitly solvated models are able to vary from 1.343 to 1.375 Å depending on the number and location of the solvent molecules. It is reasonable that the elongated length of the C–NH₂ bond (1.364 Å) falls in this range. Taking into account anharmonicity, we can expect that the averaged

distance in a real system is usually slightly larger than the equilibrium distance in theoretical calculation. Employing the slight bond elongation proves to be useful for describing IR spectrum of the real systems.

A.3.4 Simulated Spectrum for the Lowest Triplet Excited State of PNA

The use of the explicitly solvated models with elongation of C–NH₂ model has been successful for simulating the IR spectrum of the S₀ PNA. We are able to employ the resulting model also for interpretation in the lowest triplet of PNA. It is important to note that the experimental spectrum of T₁-PNA (see Figure A.4a) was produced by compensating the depletion regions in the difference spectra by using the S₀ signal. Three obvious bands in the T₁ spectrum are located at around 1250, 1480, and 1610 cm⁻¹. Our simulated spectrum of the explicitly solvated model (see Figure A.4e) can reproduce three similar bands at 1232, 1453, and 1625 cm⁻¹, respectively. According to the theoretical calculations, the characteristics of these three bands is as follow. The band at 1232 cm⁻¹ corresponds predominantly to the antisymmetric NO₂ stretch. The band at 1453 cm⁻¹ has quite complicated character and is a mixture of the in-plane C–H wagging and the C–NH₂ and C–NO₂ stretches. The band at 1625 cm⁻¹ originates from a mixture of the NH₂ scissoring motion and phenyl ring stretch; the analogous band appears in the IR spectrum of the S₀ PNA at 1650 cm⁻¹. In addition, the simulated spectrum displays good agreement with experiment in the region

around 1300 cm^{-1} . These bands resemble analogous bands in the S_0 spectrum. We also reported the T_1 spectra of the isotope-substituted PNA shown in Figure A.5 for explaining the isotope effect of these bands. However, the unequivocal confirmation of the presence of these signals depends on the validity of the compensation procedure as this region is strongly influenced by the signals from the singlet of PNA.

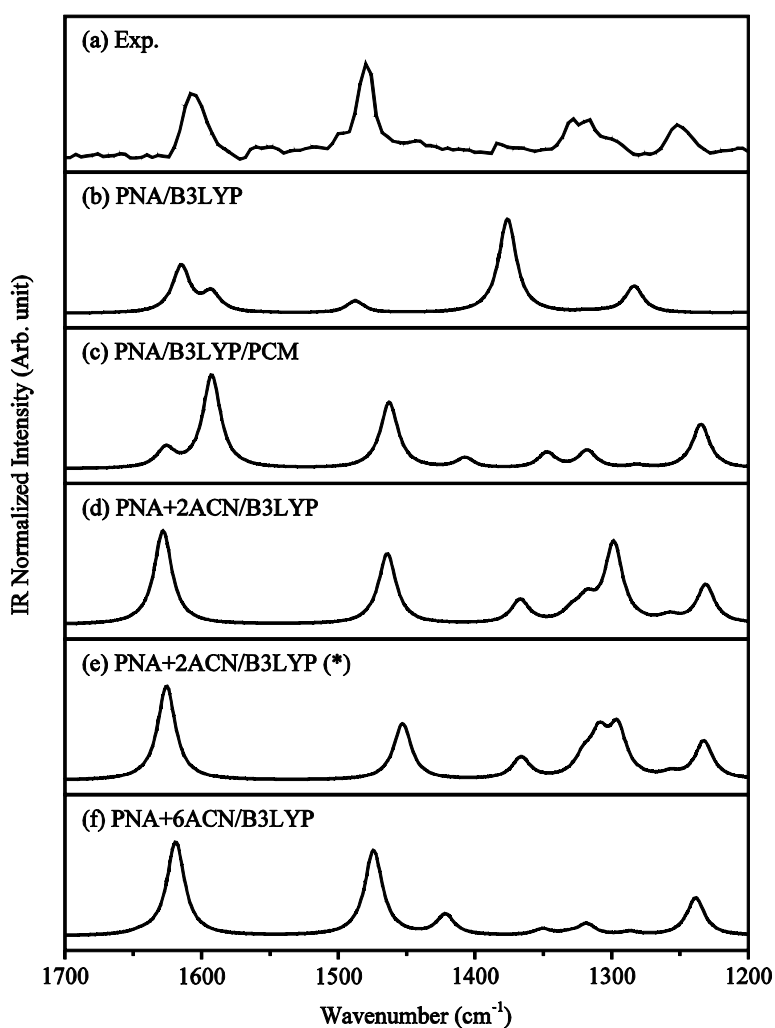


Figure A.4 Experimental and computational IR spectra for the lowest excited triplet state of PNA. The asterisk symbol indicates the spectra obtained from the PNA+2ACN with the elongation of C–NH₂ model.

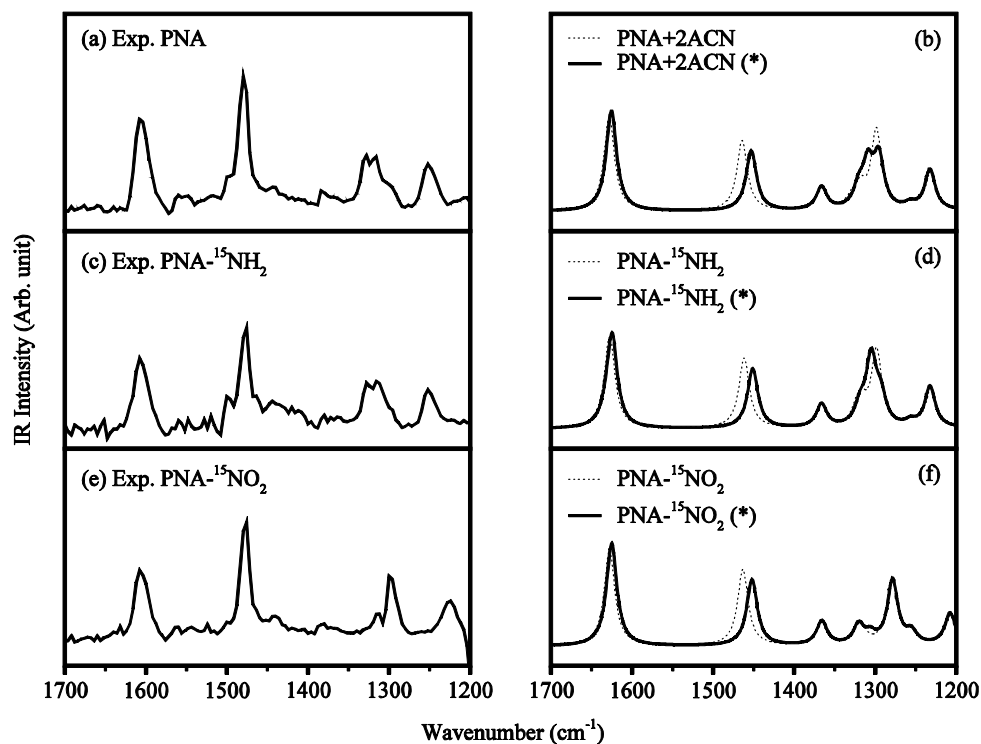


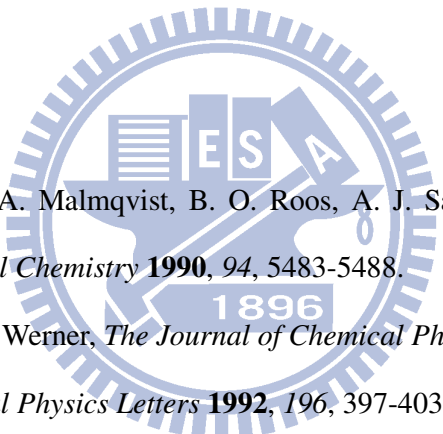
Figure A.5 Experimental and computational IR spectra for the lowest triplet state of PNA and isotope-substituted PNA. The IR spectra obtained from PNA+2ACN (dotted line) and PNA+2ACN with the elongation of C–NH₂ (solid line) models.

A.4 Conclusion

Since the gas-phase and PCM model calculations were not adequate to describe simulated IR spectra of PNA, we employed explicitly solvated models representing the system in liquid phase. The explicitly solvated models displayed remarkable success in reproducing the spectra of both singlet and triplet PNA. It was shown that the non-equilibrium geometry plays a significant role in the simulated accurate spectra. On the other side, employing too many explicit solvent molecules makes the system huge and distorts the geometry of the molecule to a degree, which probably

cannot represent the studied system. The result shows that attaching a few solvents to a molecule is enough to obtain a satisfactory result. Consequently, the use of the explicitly solvated models provides a more intuitive approach for taking into account the solvent effect, and predicts the IR spectra of the PNA correctly.

References

- 
- [1] K. Andersson, P. A. Malmqvist, B. O. Roos, A. J. Sadlej and K. Wolinski, *Journal of Physical Chemistry* **1990**, *94*, 5483-5488.
- [2] P. Celani and H. J. Werner, *The Journal of Chemical Physics* **2000**, *112*, 5546.
- [3] K. Hirao, *Chemical Physics Letters* **1992**, *196*, 397-403.
- [4] H. Nakano, *The Journal of Chemical Physics* **1993**, *99*, 7983.
- [5] C. Angeli, R. Cimiraglia, S. Evangelisti, T. Leininger and J. P. Malrieu, *The Journal of Chemical Physics* **2001**, *114*, 10252.
- [6] B. O. Roos and K. Andersson, *Chemical Physics Letters* **1995**, *245*, 215-223.
- [7] N. Forsberg and P. A. Malmqvist, *Chemical Physics Letters* **1997**, *274*, 196-204.
- [8] H. A. Witek, Y. K. Choe, J. P. Finley and K. Hirao, *Journal of Computational Chemistry* **2002**, *23*, 957-965.

- [9] C. Camacho, H. A. Witek and S. Yamamoto, *Journal of Computational Chemistry* **2009**, *30*, 468-478.
- [10] J. M. Matxain, E. Rezabal, X. Lopez, J. M. Ugalde and L. Gagliardi, *The Journal of Chemical Physics* **2008**, *128*, 194315.
- [11] C. Camacho, R. Cimiraglia and H. A. Witek, *Physical Chemistry Chemical Physics* **2010**, *12*, 5058-5060.
- [12] A. Szabo and N. S. Ostlund, *Modern Quantum Chemistry: Introduction to Advanced Electronic Structure Theory* **1996**.
- [13] I. N. Levine, *Quantum Chemistry*, **2008**.
- [14] F. Jensen, *Introduction to Computational Chemistry*, **2006**.
- [15] P. Atkins and R. Friedman, *Molecular Quantum Mechanics*, **2005**.
- [16] R. Pauncz, *The Symmetric Group in Quantum Chemistry*, **1995**.
- [17] B. O. Roos, P. R. Taylor and P. E. M. Siegbahn, *Chemical Physics* **1980**, *48*, 157-173.
- [18] K. Andersson, *Theoretical Chemistry Accounts: Theory, Computation, and Modeling (Theoretica Chimica Acta)* **1995**, *91*, 31-46.
- [19] G. Ghigo, B. O. Roos and P. A. Malmqvist, *Chemical Physics Letters* **2004**, *396*, 142-149.
- [20] H. J. Werner and P. J. Knowles, *The Journal of Chemical Physics* **1985**, *82*, 5053.
- [21] P. J. Knowles and H. J. Werner, *Chemical Physics Letters* **1985**, *115*, 259-267.
- [22] B. O. Roos, K. Andersson, M. P. Fulscher, L. Serrano-Andres, K. Pierloot, M. Merchán and V. Molina, *Journal of Molecular Structure: THEOCHEM* **1996**,

388, 257-276.

- [23] M. Schreiber and L. Gonzalez, *Chemical Physics Letters* **2007**, *435*, 136-141.
- [24] S. Shirai, S. Iwata, T. Tani and S. Inagaki, *The Journal of Physical Chemistry A* **2011**, *115*, 7687-7699.
- [25] S. Perun, A. L. Sobolewski and W. Domcke, *Journal of the American Chemical Society* **2005**, *127*, 6257-6265.
- [26] W. Zou and W. Liu, *The Journal of Chemical Physics* **2006**, *124*, 154312.
- [27] I. K.P. Huber and G. Herzberg (data prepared by J.W. Gallagher and R.D. Johnson in "*Constants of Diatomic Molecules*" in *NIST Chemistry WebBook, NIST Standard Reference Database Number 69*, Eds. P.J. Linstrom and W.G. Mallard, National Institute of Standards and Technology, Gaithersburg MD, 20899, <http://webbook.nist.gov>, (retrieved August 24, 2011)).
- [28] B. d. Darwent, *Bond Dissociation Energy in Simple Molecules*, **1970**.
- [29] A. D. Becke, *Chem. Phys* **1993**, *98*, 5648-5652.
- [30] C. Lee, W. Yang and R. G. Parr, *Physical Review B* **1988**, *37*, 785.
- [31] B. Miehlich, A. Savin, H. Stoll and H. Preuss, *Chemical Physics Letters* **1989**, *157*, 200-206.
- [32] J. Tomasi, B. Mennucci and R. Cammi, *Chemical reviews* **2005**, *105*, 2999-3094.
- [33] S. Shigeto, H. Hiramatsu and H. Hamaguchi, *The Journal of Physical Chemistry A* **2006**, *110*, 3738-3743.